8-2019

The Disk Structure of Late Type Galaxies: Determining the Black Hole Mass Function of Low Surface Brightness Galaxies Through Logarithmic Spiral Arm Pitch Angle Measurement

Michael S. Fusco
University of Arkansas, Fayetteville

The Disk Structure of Late Type Galaxies: Determining the Black Hole Mass Function of Low Surface Brightness Galaxies Through Logarithmic Spiral Arm Pitch Angle Measurement

A dissertation submitted in partial fulfillment
of the requirements for the degree of
Doctor of Philosophy in Space and Planetary Sciences

by

Michael S. Fusco
Colgate University
Bachelor of Arts in Astrogeophysics, 2013

August, 2019
University of Arkansas

This dissertation is approved for recommendation to the Graduate Council.

_____
Julia Kennefick Ph.D.
Dissertation Director

_____
Larry Roe Ph.D.
Committee Member

_____
Jiali Li Ph.D.
Committee Member

_____
Daniel Kennefick Ph.D.
Committee Member

ABSTRACT

This dissertation pertains to the geometric structure of late type (spiral) galaxies, specifically on the relation between the logarithmic spiral pitch angle of the galactic spiral arms with other properties of the galaxy, such as central Supermassive Black Hole (SMBH) mass. Our work continues a study of the Black Hole Mass Function (BHMF) in local galaxies by recording the pitch angles of spiral galaxies with lower surface brightness than were previously included. We also conduct a case study on the structure of an interestingly shaped galaxy, UGC 4599. Previous studies on the topic of spiral arm pitch angles have measured the pitch angle of galaxies using a variety of image analysis techniques. Here the effectiveness of two of these techniques are assessed under different galaxy conditions and their errors and failure modes are probed as the measurement characteristics of simulated galaxies are manipulated and degraded. This is done for the purpose of recognizing and accounting for the limits of techniques for measuring the pitch angles of galaxies as they increase in redshift or decrease in surface brightness or angular resolution (pixel size). As a result, imaging based relations in galaxy structure may be applied to extend measurements from the local universe to greater distances as long as image degradation with distance is accounted for. In exploring populations of galaxies, errors in distribution studies might result from gaps in selection; galaxies with too little apparent structure or too faint a surface brightness to be recognized as spirals and included in the study. Errors might also result from inaccuracy or failure on the measurement side, where low resolution, low surface brightness galaxies produce pitch angle measurements characterized by higher failure rates and higher associated errors for successful measurements. We work to employ new techniques to minimize these errors as well as understand and account for their effects on the distributions being measured.

DEDICATION

This dissertation is dedicated to my grandfather Saverio Catalano, whose attitude toward life and family was a constant inspiration.

ACKNOWLEDGEMENTS

Thank you to my mother, Helene C. Fusco, for all of your support, especially in keeping me organized and on task over the years. Thank you to my father, Angelo M. Fusco, for running logistics and support, and for keeping me interested in Scouting, which has been such an important part of my life. Thank you to Mr. Norman Burtness, for sparking my interest in physics and preparing me for my undergraduate adventure at Colgate. Thank you to Dr. Jonathon Levine for keeping my passion in Planetary Science alive and well, and to Dr. Beth Parks for pushing my comfort zone and challenging me to extend my limitations. Thank you to Drs. Julia and Daniel Kennefick for bringing me on to graduate study at the University of Arkansas. The opportunity to work with you on these projects has been enjoyable and memorable. Thank you to Dr. Mike Rich for inviting me to collaborate on the Halos and Environments of Nearby Galaxies (HERON) Survey. The trips to UCLA to observe and share knowledge were valuable and your family's hospitality is much appreciated. Thank you to my colleagues at the Center for Space and Planetary Sciences for your collaboration and lifelong friendship. Finally, thank you to all those who have mentored, helped, or rooted for me along the way and helped me to find my path in life.

"When you know all the names in every language of that bird, you know nothing, but absolutely nothing about the bird…So I had learned already that names don't constitute knowledge…that's caused me a certain trouble since, because I refuse to learn the name of anything…knowing the names of things is useful if you want to talk to someone else."

-Richard Feynman

TABLE OF CONTENTS

LIST OF FIGURES

LIST OF TABLES

LIST OF PUBLICATIONS

Chapter 2 – Pitch Angle Distribution Function of Local Spiral Galaxies and Its Role in Galactic Structure, Michael S. Fusco, Benjamin L. Davis, Daniel Kennefick, Marc S. Seigar, and Julia Kennefick, ApJ, Submitted

Chapter 3 – UGC 4599: Revealing the Extended Structure of a Giant Low Surface Brightness Hoag's Object Analog with HERON, Michael S. Fusco, David Thilker, Noah Brosch, Michael West, Michael Gregg, Francis Longstaff, Aleksander Mosenkov, Andreas Koch, Jayce Dowell, Liese Van Zee, MNRAS, Submitted

1 Introduction

This scientific dissertation is comprised of three main research studies which are continuations of the work of two separate research collaborations. The focus of this research is toward the development of methods for producing images and for measuring properties of galaxies at low surface brightness or low signal to noise ratios. This is undertaken in order to achieve various ends, including improvements in mapping of the outer regions of galaxies. Of particular interest are surface brightness measurement and galactic spiral arm pitch angle measurement at low signal to noise ratios and low spiral arm to interarm contrasts. Pitch angle measurement at higher redshifts has become crucial to better understand spiral galaxy evolution.

The Arkansas Galaxy Evolution Survey (AGES) group is involved in the study of the evolution of spiral galaxy structure, predominantly the relationships between Supermassive Black Holes (SMBH) at the center of most galaxies with other galactic properties and how these SMBH evolve over time (Seigar et al., 2008; Berrier et al., 2013). To this end, the group has undertaken studies of the black holes of local quiescent spiral galaxies, as well as less local Active Galactic Nuclei (AGN). Research on behalf of the AGES group in this dissertation concentrates on extending our measurements of SMBH masses using spiral arm pitch angle to a fainter set of galaxies than in previous work. In addition, a detailed assessment of the limitations and biases of various techniques in use for measuring these black hole masses is undertaken in order to better constrain limitations of pitch angle measurement techniques for future datasets at higher redshifts.

The Halos and Environments of Nearby Galaxies (HERON) Survey (Rich et al., 2017) is a project primarily utilizing observations on 0.7 meter telescopes in California and Israel to image local galaxies and dwarf companions at low surface brightness, at times exceeding 30

mag./arcsec^2. This dissertation's contribution to the HERON project involves the study of a specific galaxy, UGC 4599, which is a possible analog to Hoag's Object, a galaxy with an elliptical-like core region and bright star forming ring structure. UGC 4599 is also found to be a Giant Low Surface Brightness Galaxy (GLSB) with a very faint (26th central r magnitude) disk.

1.1 Logarithmic Pitch Angles in the Arms of Spiral Galaxies

Logarithmic spirals are self-similar curves found often in nature, where the distances between turnings of the spiral increase in a geometric sequence (rather than other spiral types such as Archimedean spirals with a linear growth sequence). Spiral galaxies may contain arm shaped regions of star formation visible in both the gas and the stars of the galaxy, across a wide range of wavebands. These spiral structures may be well organized and with a high arm-interarm contrast, often referred to as a grand design spiral. Grand design spirals possess two arms which are usually well described by a logarithmic spiral curve (Seigar & James, 1998). Other spiral galaxies are called flocculent, with no well-defined arms extending from the galactic center to the outer edge. These instead are composed of several arm fragments or spurs which occupy relatively small regions of the galaxy (Elmegreen, 1981; Seiden & Gerola, 1982). Finally, there exist multi-armed galaxies which have a tendency toward less symmetrically spaced arms than their two armed grand design cousins. These may represent an intermediary between the well defined structure of the grand designs and the low contrast spurs of the flocculent galaxies.

1.1.1 Pitch Angle

Logarithmic spirals are described mathematically by the equation given below, where r is the radius of the spiral, theta is the phase angle of the spiral with relation to the x axis, and a and b are constants.

Equation 1.1: $r = ae^{b*\Theta}$

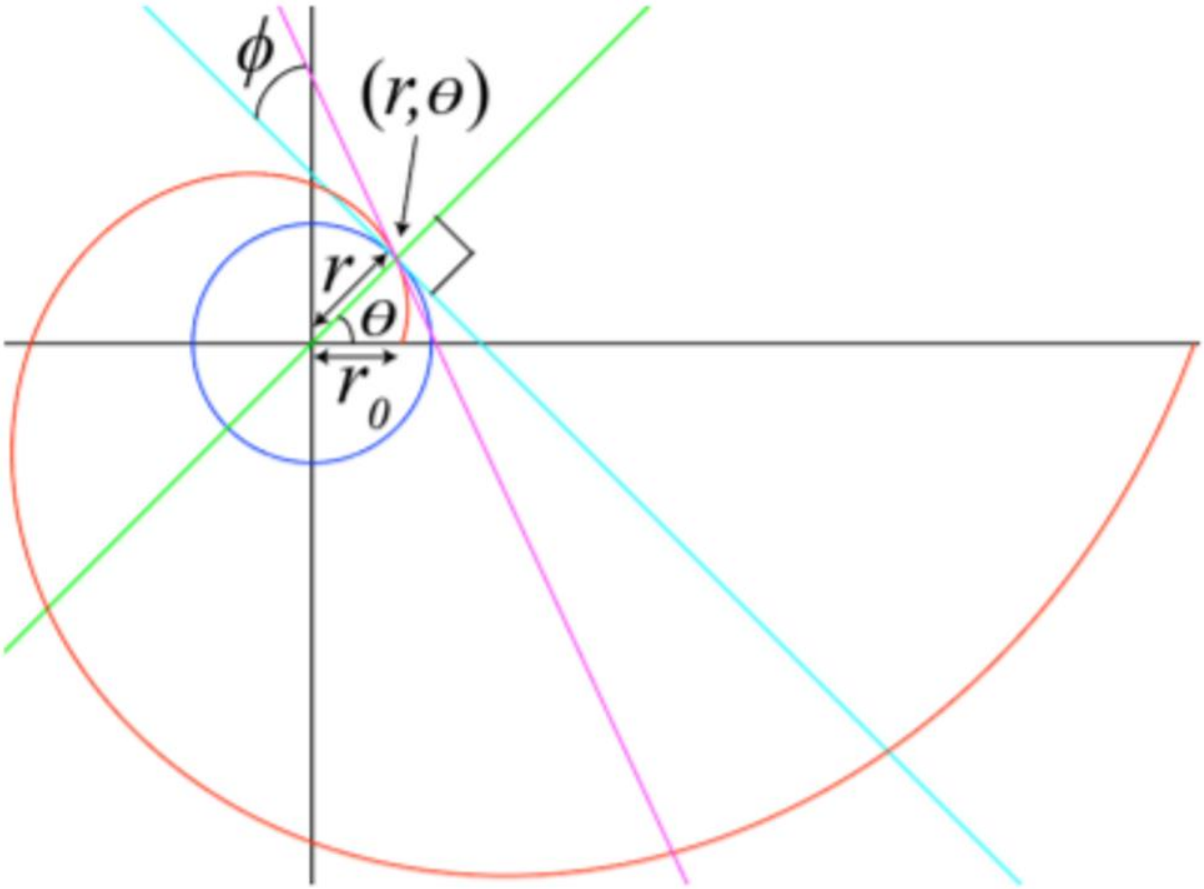

Figure 1.1 Figure reproduced from Davis et al. (2017). A logarithmic spiral (Red), circle (blue), line tangent to the logarithmic spiral (magenta) at point (r,Θ), line tangent to circle (cyan) at point (r,Θ). The pitch angle (the angle between the tangent to the circle and the tangent to the spiral) is $|\phi|=20^{o}$.

Perhaps a more intuitive parameter for understanding the shape of a logarithmic spiral is its pitch angle. The pitch angle of a spiral is the angle between the spiral and the tangent line of a circle drawn at the same radius as the spiral. A pitch angle of 0^{o} implies the shape of a circle,

while a pitch angle of 90º is a radial line. For values between zero and ninety, the lower the pitch angle of the spiral, the tighter its winding. For logarithmic spirals, the value of the pitch angle is constant at all radii. The pitch angle is related to one of the constants (b) in the equation for the logarithmic spiral:

$$\text{Equation 1.2: } \phi = \arctan\left\{\frac{1}{b}\right\}, P = 90^{\circ} - \phi$$

The pitch angle of the spirals in spiral galaxies take on a large range of values but interestingly their distribution in the local universe peaks somewhat close to the Golden Spiral (P=17.03 degrees), which grows by one Golden Ratio every quarter of a turn of the spiral (Davis et al., 2015).

1.1.2 Density Wave Theory and its Application to Studies of Galactic Supermassive Black Hole Masses

In gravitationally bound systems with flattened disk structures, spiral shaped disturbances in the disk density are common. These spiral structures are present in numerous different physical systems including planetary rings, protoplanetary disks around young stars, and galactic spiral arms. Notable propositions for physical explanations for the initiation and propagation of these spiral arms include: Density Wave Theory (Lin & Shu, 1964), Swing Amplification Theory (Kormendy 1981; Gerola & Seiden 1978; Seiden & Gerola 1979), and Manifold Theory (Gerola & Seiden ,1978, 1979; Kormendy, 1981; Kaufmann & Contopoulos, 1996).

1.1.2.1 Manifold Theory

One possible explanation for the spiral structure observed in galaxies is the Manifold Theory (Gerola & Seiden ,1978, 1979; Kormendy, 1981; Kaufmann & Contopoulos, 1996). Manifold Theory forms spirals from stars born near the ends of galactic bars carried along paths (manifolds) in eccentric orbits. Motion along these narrow paths creates the appearance of spiral arms on the galactic scale. The orbital shapes are controlled by the central mass concentration of the galaxy (Athanassoula et al. ,2012). Athanassoula et al. (2011) offer explanations for inner rings at the radius of galactic bars, outer rings near twice the bar radius, and spiral structure due to manifold orbits forced by Lagrangian points near the bar. The L1 and L2 points in a barred galaxy account for the m=2 spiral arm shape, although higher order forcing modes may result in other morphologies such as m=4. The strength of the non-axisymmetric forcing at the corotation radius is determinative of which morphology is produced, with stronger forcing producing spirals and weaker forcing producing rings (Athanassoula et al., 2009).

1.1.2.2 Swing Amplification

Spiral patterns in disks with leading arms shear into trailing patterns over time. Under certain conditions this trailing spiral may grow in amplitude as it shifts from leading to trailing. This phenomenon is referred to as swing amplification, described in Goldreich & Lynden-Bell (1965), Julian & Toomre, 1966). Michikoshi & Kokubo (2014) find pitch angles of spirals to increase with epicycle frequency and decrease with shear rate. They invoke swing amplification as an explanation of this phenomenon.

Swing amplified spirals should be transient processes rather than the more persistent structures invoked in other models of spiral structure. Swing amplification is shown to be a stronger factor in gas than in stars, and gas features to have lower pitch angles than stellar features (Jog, 1992). In most cases, swing amplification is considered in a two fluid system which separates gas and stars as the main components. These fluids interact gravitationally (Toomre, 1981). In galaxies where gas is a contributor in two fluid models, the range of pitch angles is increased as a result of coupling between the two fluids (Jog, 1992). In wooly or flocculent galaxies which lack the well defined m=2 spiral structure of grand design galaxies, the creation and propagation of transient spurs and arm fragments as a result of swing amplification may be the dominant process, rather than the bar-caused manifolds or modal density waves.

1.1.2.3 Density Wave Theory

Density Wave Theory (Lin & Shu, 1964) is a system which describes the origin of spiral structure in gravitationally bound disk systems as a result of waves emanating from Lindblad resonances. Lindblad resonances are locations in the disk where the epicyclic frequency is in resonance with a forcing frequency. Particles near Lindblad resonances typically have their eccentricities forced to higher values, which eventually drives the creation of spiral density waves (Shu, 1984). When a star orbits faster than the speed of the spiral arm, this is an inner Lindblad resonance, whereas when the arm moves faster than the star, an outer Lindblad resonance occurs. Density waves generated at the Lindblad resonances propagate outwards from ILRs and inwards from OLRs (Shu, 1984). Density waves are divided into linear and nonlinear regimes. In the linear case, the perturbing force is relatively small and the resulting density wave

is mostly sinusoidal. Linearized, self-gravitating response of a heavy mass point embedded in a collisionless stellar disk was first studied by Julian & Toomre (1966).

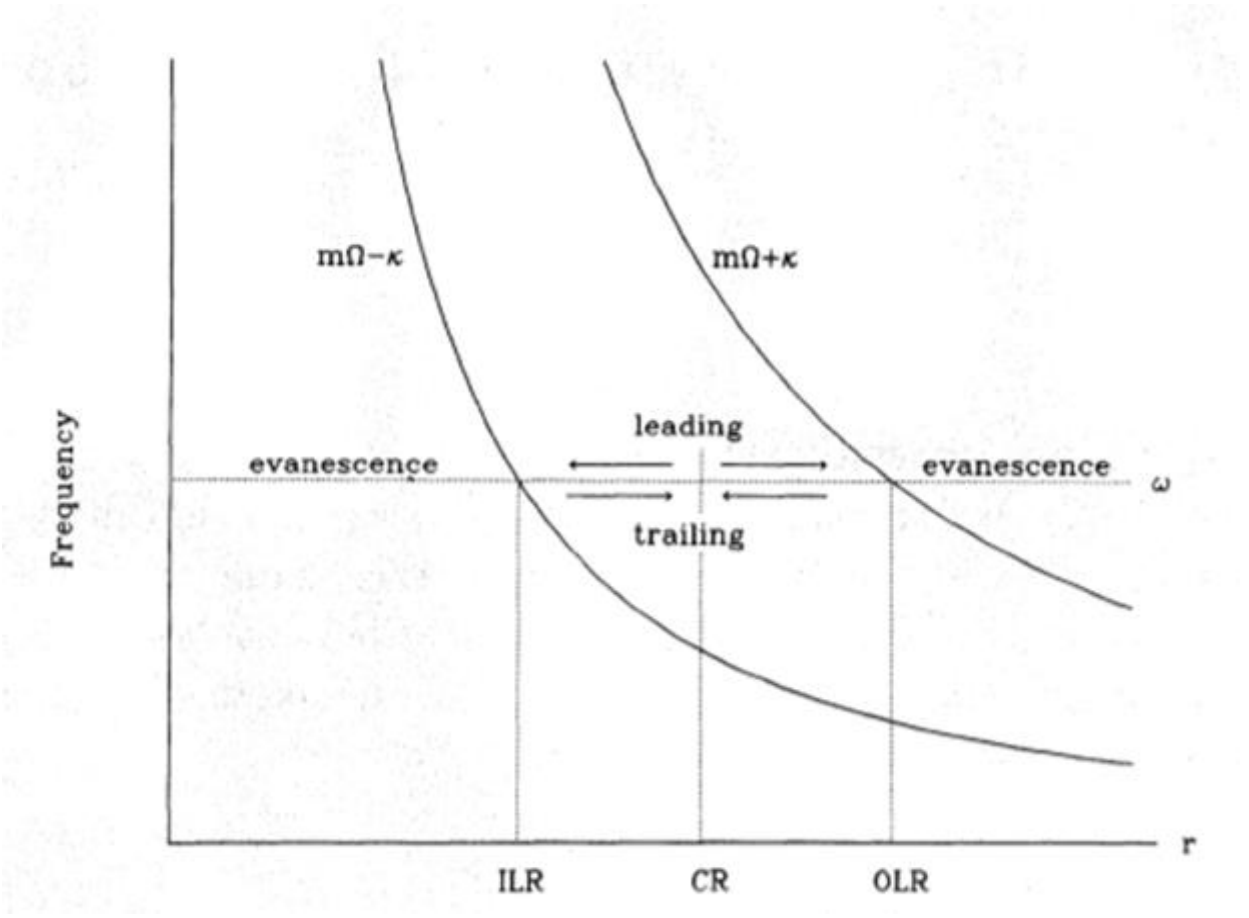

Figure 1.2 Figure reproduced from Shu (1984). Schematic showing long trailing spiral density waves which propagate away from inner and outer Lindblad resonances while long leading spiral density waves propagate toward them. Long waves reflect and transmit as short waves at the corotation radius. The regions beyond the Lindblad resonances are evanescent.

The theory behind density wave patterns in Saturn's rings is well developed (Goldreich & Tremaine, 1982; Shu, 1984). In the example of Saturn, multi armed patterns with extremely low pitch angles are generated at mean-motion resonances with orbiting moons. An additional set of waves, primarily in Saturn's C ring, are the consequence of anomalies in Saturn's gravitational

field (Rosen et al., 1991). A majority of the spiral structure in Saturn's rings is the result of resonances with Saturn's moon or the planet itself. For spiral galaxies, instead, the gravity wakes of spiral shaped potentials allow for-self propagation of density waves. While self-gravity wakes exist in the rings of Saturn, these may be the result of swing amplification processes rather than density waves (Salo, 1995).

Density wave theory in its application to protoplanetary disks has also been extensively investigated. In planetary disks both linear (Goldreich & Tremaine, 1980) and nonlinear (Goodman & Rafikov, 2001) regimes have been examined. Spiral structures have been observed in several disks, including those around Herbig Ae/Be stars SAO 206462, MWC 758, and HD 100546 (Muto et al. 2012; Garufi et al. 2013; Grady et al. 2013; Benisty et al. 2015; Currie et al. 2014). The spirals of SAO 20642 and MWC 758 are m=2 and resemble the grand design structures seen in spiral galaxies.

Spiral Density Waves in protoplanetary disks are important in type I migration processes for low mass planets (Nelson, 2005; Nelson & Papaloizou, 2004). This is accomplished through angular momentum transfer between the density waves in the disk and the planet. The final locations of planets in star systems are at least partially the result of transport of the orbits of these planets through disk migration. In planetary disks, the pitch angle of the spiral arms depends on the planetary mass. This fits with the non-linear formulation of density wave theory. More massive planets produce spirals with larger pitch angles and larger angular separation between the primary and secondary arms (Zhaohuan et al., 2015).

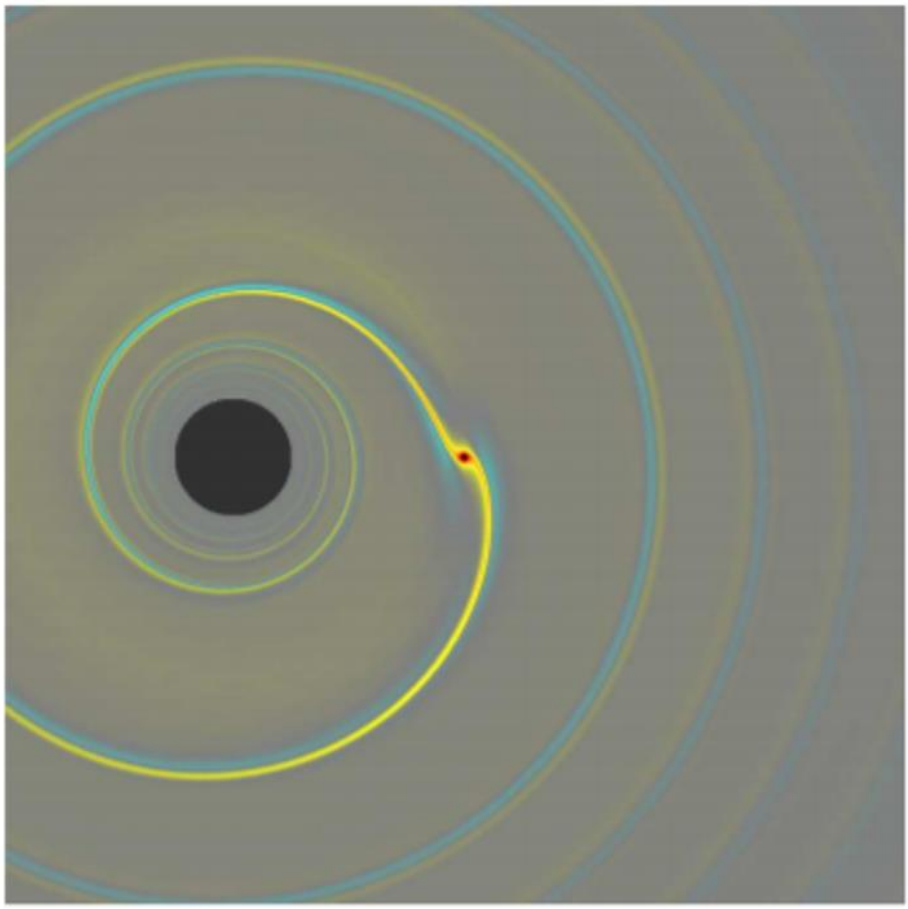

Figure 1.3 Figure reproduced from Duffell and MacFayden (2012). The perturbation to the surface density caused by a low mass planet $M_p = 0.0209M_{Th}$. The planetary wake traces out a spiral shape.

1.2 The M-P Relation and Fundamental Plane

A relation between the morphology of galactic spiral arms and the supermassive black hole mass at the centers of spiral galaxies is identified in Seigar et al. (2008). Modal density wave theory predicts a correlation between the central mass concentration and the pitch angle of the spiral arms (Grand et al., 2012). In an analog to Saturn's rings, where the central mass is the planet and the rings make up a thin debris disk, spiral galaxies frequently contain classical or pseudobulges at their centers, a portion of the mass of which includes supermassive black holes. The gas and stars of the galaxy are the equivalent of the rings for Saturn. The mass ratio between

Saturn and its rings is much greater than the ratio of the central mass in spiral galaxies and the mass of the disk. Spiral galaxies, while being much more complex structures than the simple planet-ring case, are still subject to spiral patterns driven by density waves.

The central bulge mass and supermassive black hole mass of galaxies are likely correlated (Silk & Rees, 1998). If the spiral structure of galaxies is governed by density waves, the parameters of which are constrained by the ratio of the central mass to the disk mass, it should be the case that the supermassive black hole mass of the galaxy would correlate with the pitch angle of the galactic spiral arms. This relationship may be understood as a standing wave pattern which depends upon the density of the disk and the central mass of the galaxy. The proportionality relationship follows the following equation (Seiger et al., 2008):

Equation 1.3: $\tan|P| \propto (\sigma_o + F\sigma_*) / M_o$

where P is the pitch angle of the galaxy, the numerators contain the densities of the gas and stars as well as a constant, and the denominator is the bulge mass of the galaxy. This relation has been developed into an equation for the SMBH mass as a function of the pitch angle of the spiral arms (Berrier et al., 2013).

Equation 1.4: $\log(M/M_\odot) = (b \pm \delta b) - (k \pm \delta k)|P|$

with $b = 8.21$, $\delta b = 0.16$, $k = 0.062$, and $\delta k = 0.009$

Davis et al. (2015) update this relation to a "Fundamental Plane" among the pitch angle, neutral hydrogen gas density in the disk, and bulge mass of the galaxy:

Equation 1.5: $$\frac{\Sigma_{H_I}^{max}}{M_\odot pc^{-2}} = (5.70 \pm 1.40)\tan|P| - (0.677 \pm 0.199)\log\left(M_*^{bulge}/M_\odot\right) + (9.29 \pm 1.96).$$

For late type galaxies, these relations have been shown to have less scatter than other methods for measuring SMBH masses (Davis et al. 2017). A clear advantage of the M-P relation is the capability to measure the SMBH mass of late type galaxies by proxy with imaging of the spiral arms rather than spectroscopy. This technique should ease measurement of SMBH masses at higher redshifts where spectroscopic censuses may not be available.

1.3 Black Hole Scaling Relations and the The Black Hole Mass Function

The Black Hole Mass Function (BHMF) is a distribution which describes the relative abundances of black holes as a function of mass in the universe. There are many different techniques used to measure the masses of black holes and many scaling relations among different galactic properties and their central SMBH masses. Many of these relations involve the bulge of the galaxy and include stellar luminosity, sersic index, and the stellar velocity dispersion (σ) of the bulge (for review, see Graham 2016). Other frameworks have the dark matter halo properties as the major determinant of SMBH mass (Loeb & Rasio 1994, Silk & Rees 1998, Cattaneo et al. 1999, Haehnelt & Kauffmann 2000, Monaco et al. 2000, Adams et al. 2001). The rotational velocity profile of a galaxy may be considered a proxy for the dark matter halo mass. Davis et al. (2018) find a relation between the total stellar mass of a spiral galaxy and its SMBH. The total stellar luminosity of a galaxy correlates with its rotational velocity in the Tully-Fisher relation (Tully & Fisher 1977). Kennicutt (1981) and Kennicutt & Hodge (1982) find an anticorrelation between vmax (the maximum rotational velocity of the disk) and the spiral arm pitch angle, where galaxies with higher vmax have lower pitch angles (tighter spirals).

These sets of scaling relations among galaxy properties may be used to build up several different measures of the SMBH masses of galaxies such that populational surveys may be taken. Finding a Black Hole Mass Function (BHMF) for galactic SMBH has impact on cosmology questions. The time dependency of the BHMF is of interest toward better understanding galaxy evolution. The Black Hole Mass Function for early type galaxies has been measured (Marconi et al. 2004, Graham et al. 2007, Vika et al. 2009) as has the BHMF of late type galaxies in the local universe (Davis et al. 2014). Later in this research we provide corrections to the late type BHMF by including fainter galaxies than were used in the Davis et al. (2014) study. The properties of SMBH and intermediate mass black hole (IMBH) masses in extremely late type spirals and dwarf galaxies are also of interest in constructing a complete BHMF.

1.4 Pitch Angle Measurement Techniques

There are several techniques commonly employed in the measurement of the logarithmic spiral arm pitch angle of galaxies. These include: manual selection of points on spiral arms and fitting to the equation for a logarithmic spiral, manual logarithmic spiral overlays, Fourier Decomposition techniques to find pitch angle (Davis et al., 2012), machine vision techniques (Dieleman et al., 2015), and template fitting techniques (Shields et al., 2015). For this research, we primarily use the codes 2DFFT (Davis et al., 2012) and Spirality (Shields et al., 2015b), with spiral overlays as visual checks on the calculated values.

Here we will examine the set of best practices for performing pitch angle measurement using 2DFFT and Spirality. In order to properly set up galaxy images for pitch angle measurement there are several important preparatory processing steps which need be

systematically followed for best results. The first of these issues is that of foreground star removal. Galaxies with foreground stars in their images may cause disruptions to the measured pitch angle in both 2DFFT and Spirality; counts from bright foreground stars tend to outshine the spiral arms and force the fit of the spiral through these stars. This problematic effect is counteracted in a few possible ways.

First, star subtraction should be performed. Our preferred method of star subtraction is through the use of the IRAF routine DAOPHOT (Stetson, 1987), wherein a Point Spread Function (PSF) for the stars in the image is fit, a list of point sources to remove are generated and have photometry performed, and this list of stars is subtracted using the user generated PSF. DAOPHOT is preferred over other star subtraction methods in being able to cope with stars which have nearby neighbors whose light profiles overlap. The main drawbacks of DAOPHOT are imperfect PSF creation and removal of stars, particularly for stars which have the disk of the galaxy in their background.

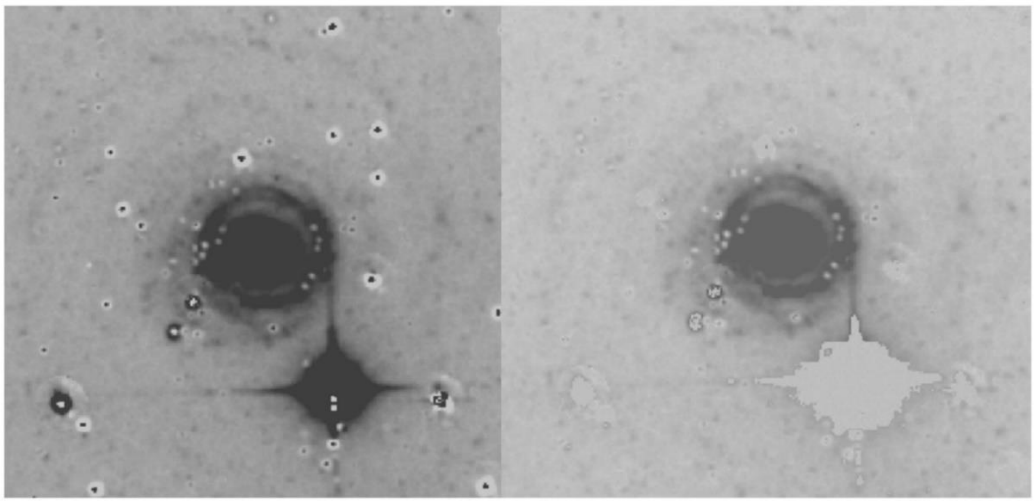

Figure 1.4 Left: DAOPHOT star subtracted image of the galaxy UGC 4599. Right: Same image iteratively sigma clipped to reduce signal from star subtraction residuals and oversaturated foreground stars. The iteratively clipped image is much better behaved when run through spiral arm pitch angle fitting codes or scripts to measure the radial brightness profile.

For some galaxies, it may prove beneficial to further remove counts from the residuals of the star subtraction. To this end, we have written a script in MATLAB which allows both high and low sigma clipping of sets of pixels within the image. We replace removed pixels with the mean sky value, though it may be beneficial for certain stars to use the local 'sky' value which includes the background galaxy disk as part of the sky. These replacements serve the advantage of allowing maximum removal of excess pixels from the star subtraction residuals without removing counts from galaxy pixels. Boxes for clipping may be placed around individual stars, or iterative radial clipping from the center of the galaxy with different high sigma may be performed. In this way, the goal is to minimize excess counts from star subtraction residuals.

After star subtraction is satisfactorily achieved, the next step toward measurement of pitch angle is deprojection of galaxies which are not face-on to a face-on orientation. This is usually accomplished by using the IRAF routine Ellipse to find the ellipticity of the galaxy disk, and deprojecting the galaxy to be circular. An alternative method is to define the inclination as that which produces the cleanest logarithmic spiral. This technique takes several different deprojections of the galaxy and measures the pitch angle of all of them, searching for the lowest associated error. Incorrect deprojection of the galaxy does not have a strong effect on the recorded value of pitch angle, though it does increase the size of the associated error with the pitch angle measurement (Davis et al., 2012).

The galaxy should now be face-on in orientation, with stars subtracted. From this position, it is still possible to improve the stability of the resulting pitch angle measurements from the image. This is accomplished by taking symmetrical components of the image. A symmetrical component image of order m takes sets pixels with the associated symmetry and replaces their counts with the value of the lowest pixel of the set. For an m=2 symmetrical component image,

pixels of the same radius but 180º (radially opposed) from one another are grouped; for m=3, pixels 120º apart and so on. This accomplishes the removal of non-axisymmetric components from the image, including the removal of foreground stars as long as there are no other foreground stars in the same pixel group. Also, irregular structures within the galaxy such as spiral arm spurs which do not have symmetric siblings on the other side of the galaxy are removed. However, as the lowest pixel value in the set is the one adopted, the brightness of the galaxy is diminished. There is a trade-off, then, between the signal to noise ratio of the galaxy over the sky and the disruption caused by non-axisymmetric components of the galaxy on the pitch angle measurement. If arms are not perfectly symmetric, arm-interarm contrast is reduced. Often, performing analysis on the symmetrical component image of a galaxy dramatically expands the stability of the pitch angle measurement compared to the star subtracted image, and is worthwhile despite the diminished signal/noise.

Another technique with the tendency to improve pitch angle measurement is the use of the software GALFIT (Peng et al., 2002) to fit and remove bulge or bulge and disk components from the galaxy. GALFIT is a software for modelling galaxy structure, the newest version of which includes non-axisymmetric components such as spiral arms, tidal tails, and others (Peng et al., 2007). The types of mathematical spirals produced in GALFIT models do not lend themselves well to producing a pitch angle measurement. Even so, modeling a simple Sersic component for the bulge of the galaxy, and possibly another Sersic or exponential function for the disk of the galaxy, may be advantageous. Removing the bulge and disk from the galaxy leaves the spiral structure in the residual image. Light in galaxies tends to be centrally concentrated, and our commonly used pitch angle measurement techniques have increased sensitivity to the brightest pixels along the spiral arms. This means both 2DFFT and Spirality are overly reactive to the

pixels at lower galactic radii when determining the pitch angle. By attempting to remove the core and disk of the galaxy, we flatten the radial brightness profile of the galaxy, and correct this center-biasing to some degree. The final images to be measured for pitch angle, then, are star subtracted, iteratively sigma clipped, symmetrical component images which have had their bulge and disk features removed.

1.5 Surface Brightness Mapping

Accurate mapping of the surface brightness of galaxies necessitates similar preprocessing techniques to those employed for pitch angle measurement: star subtraction with DAOPHOT, Iterative Sigma Clipping and pixel replacement. If deprojection is performed, attention must be paid to the corrected pixel scale of the deprojected image. Symmetrical component images are not useful for surface brightness mapping as they inherently result in the galaxy image being altered to fainter than real values by changing pixel values to the lower of the pair/set. Individual pixels are transformed from counts to surface brightness values. Once a surface brightness map is produced, it may be useful to fit smoothing contours to this map for a better fit measurement of the surface brightness map.

1.5.1 Calibration of Luminance Filter to Sloan r magnitude

For faint galaxies, dwarf companions, or galaxies with faint outer regions of interest, it is best to image in the luminance filter, which spans a wide swath of optical wavelengths. The intention of observing with luminance filter is to allow as much galaxy light as possible into the aperture in order to shorten the exposure times required to reach the same effective limiting

magnitude. This allows very deep imaging of galaxies at reasonable exposure times. For comparison, though, it is useful to translate surface brightness data in luminance band to other, more commonly used filters such as the Sloan u, g, r, i, z system. For our studies of UGC 4599, we convert from luminance filter instrumental magnitudes per pixel to Sloan r surface brightness in magnitudes per square arcsecond.

We select 18 foreground stars in the field of UGC 4599 with known u, g, r, i, z magnitudes to produce a transformation equation for our instrument. For this work, we find a transformation from the instrumental luminance filter magnitude to the Sloan r filter equivalent magnitude (see figure 1.5). The g and r colors of the stars are known from the Sloan Digital Sky Survey catalogue.

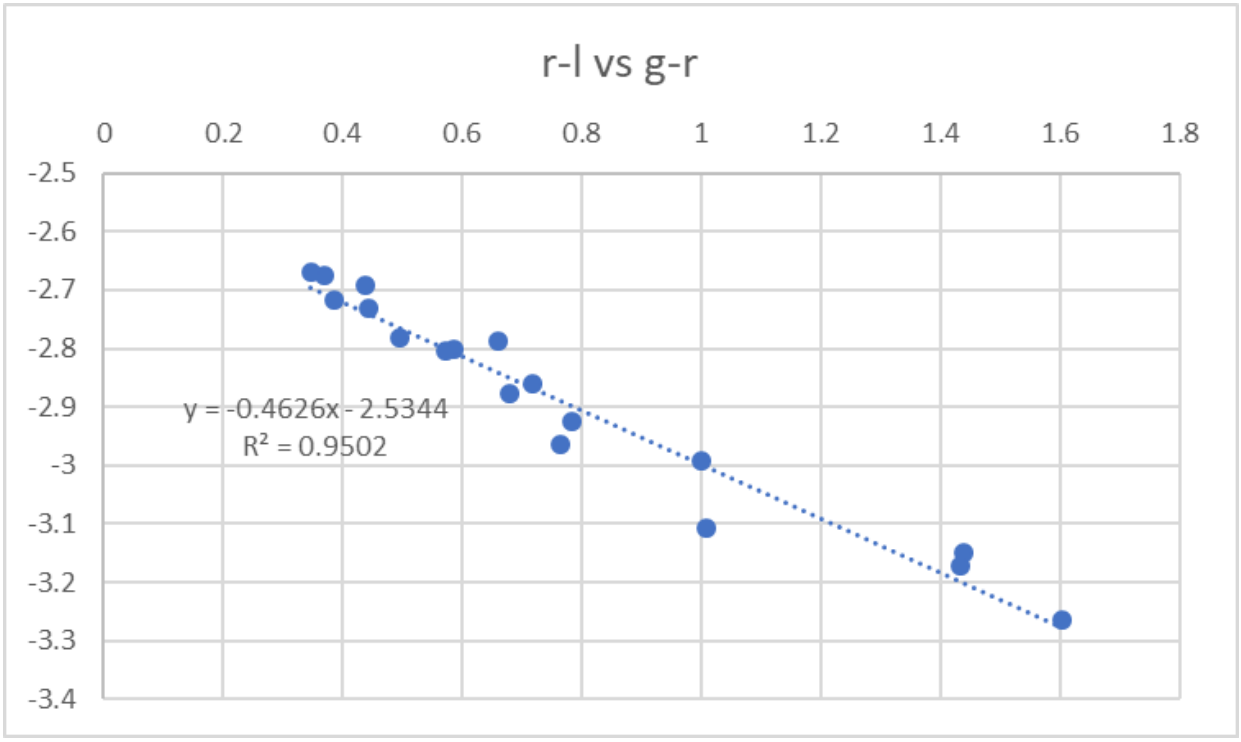

Figure 1.5 $r\text{-}l_{ins}$ vs. g-r plot for comparison stars of known u, g, r, i, z magnitudes in the field of UGC 4599. These stars produce a best fit equation of $(r\text{-}l_{ins}) = 0.4626*(g\text{-}r)\text{-}2.5344$. With this equation, if the g-r color of an object is known, a conversion from instrumental luminance filter magnitude to r magnitude may be performed.

In converting from luminance to r, it is helpful to know color information from the target object. We use a globally selected g-r color for the galaxy to define our conversion. Using literature values for the g-r color of the star forming ring of UGC 4599 (Finkelman & Brosch, 2011), we adopt this color for the entire galaxy image. This may not be as accurate in the core region of the galaxy, but we are most interested in the outlying faint spiral structure which is likely to have the similar g-r color to the star forming ring. As it may be demonstrated from the fit, using the wrong g-r color will result in an offset of the measured r magnitude by up to a few tenths of a magnitude. When assuming a g-r color for an extended object, in practical terms, the location of a given surface brightness contour may shift inwards or outwards due to the incorrect calibration. Realistically, galaxies do not have a constant color throughout their structure, so finer detail mapping might be useful in some situations. For our study of UGC 4599, we reasonably assume the spiral structure in the disk to have a similar g-r color to that of the star forming ring as measured in Finkelman & Brosch (2015). For faint outer structures in galaxies, our errors are likely to primarily come from either incorrect characterization of the g-r color of the region or from imprecise measurement of the mean sky flux at that region.

1.5.2 Radial Surface Brightness Profiles

In addition to generating surface brightness images and contour maps of galaxies in order to showcase spiral structure, the production of 1D or 2D radial surface brightness profiles of the galaxy is instructional. These radial profiles may be decomposed into models of their constituent parts, which might include features such as a bulge in the core of the galaxy, an exponential disk, star forming rings, and excess light due to spiral arms.

Decomposition of the galaxy, at least at the level of separating a bulge from a disk, is helpful in characterizing some critical galaxy properties. A common software used to produce radial surface brightness profiles is the routine Ellipse in IRAF. Most radial surface brightness modeling codes take as input the tables produced by the ellipse routine or some variant on it. For this research, we use modified versions of the Ellipse and BModel routines called ISOFIT and CModel (Ciambur, 2015). These improve on the fitting of Ellipse by replacing the polar coordinates with eccentric anomaly, removing cross-like patterns from fit residuals. Our preferred modeling software for bulge-disk decomposition is Profiler 2.0 (Ciambur, 2016). This package allows fitting of the output tables of Ellipse, Isofit, or I(r) tables with various components. Bulges are modeled as Sersic functions, rings as gaussians, and disks as either simple or truncated/antitruncated exponentials.

When attempting to fit a radial surface brightness profile to a galaxy, perhaps the most important parameter to get correct is the value of the sky in the image. Ideally, the sky should be flat across the image. If there is a slope to the sky values from one side of the image to the other the IRAF routine ImSurFit is capable of fitting and correcting linear or polynomial variability of the sky. For images with galaxies which have extended faint disks, special care must be taken to select sky values from a region outside of the galaxy edges, which may be difficult to identify. Near the limiting magnitude of the detector, a single count of sky may make a large (excess of 1 magnitude at the detection limit) difference in terms of the surface brightness profile recorded.

One good check on the sky value is to examine the radial surface brightness profile and identify the outer edge of the disk of the galaxy. If the chosen sky value for the image is too high, the lowest brightness galaxy pixels and most of the sky pixels will be recorded as zero or negative flux. If the sky value is too low, all of the sky pixels (even those below the skymean)

will have an associated surface brightness. If the sky fit is good, the outer boundary of the galaxy will be visible as an antitruncation in the surface brightness profile as the disk fades into the sky noise, and the sky outside this radius should have flux values very close to zero with large associated errors in surface brightness (on the order of one magnitude). Incorrectly chosen sky values mainly cause a vertical shift in the surface brightness profile, which might affect other measurements of parameters such as star formation rates.

In addition to modeling and subtracting the sky, a good radial surface brightness profile should either include spiral arms as a contributing model component, or seek to mask spiral arms from the image by replacement with the designation Not a Number (NaNs). Foreground stars in the image should also be masked. Masks are here preferred to the previously mentioned star subtraction and sigma clipping techniques. Those techniques, while very useful for producing images which retain as much galaxy structure as possible, are often imperfect in subtracting stars from the image, and may result in a region which does not match the brightness of the galaxy disk at that radius. For this reason, bad pixel mask creation and replacement of bad pixels with NaN is the common practice.

1.6 Giant Low Surface Brightness Galaxies

The study of low surface brightness galaxies (LSBs) has been popular recently as the capabilities of ground based telescopes have improved. Many galaxies which were formerly classified as elliptical are being reconsidered as LSBs as deep observations at low surface brightness have become available (Hagen et al., 2016). LSB galaxies are characterized by low star formation rates, abundant hydrogen gas, and low metallicities, with the canonical example being that of Malin 1 (Bothun et al., 1987). The disks of low surface brightness galaxies are

defined as having a central surface brightness fainter than the Freeman (1970) value for disk galaxies of μ_{oB}=21.65 mag/arcsec^2. The limiting threshold for what constitutes a low surface brightness disk varies across authors, but is generally between 22 and 25 mag/arcsec^2. These galaxies contribute a significant fraction of the total light from galaxies (Impey & Bothum, 1997). Low surface brightness galaxies are divided into a few different categories: Dwarf LSBs, LSBs, and Giant low surface brightness galaxies (GLSBs). This latter category, GLSBs, have some of the largest disks observed in galaxies, up to 250 kpc in diameter (Boissier et al., 2016).

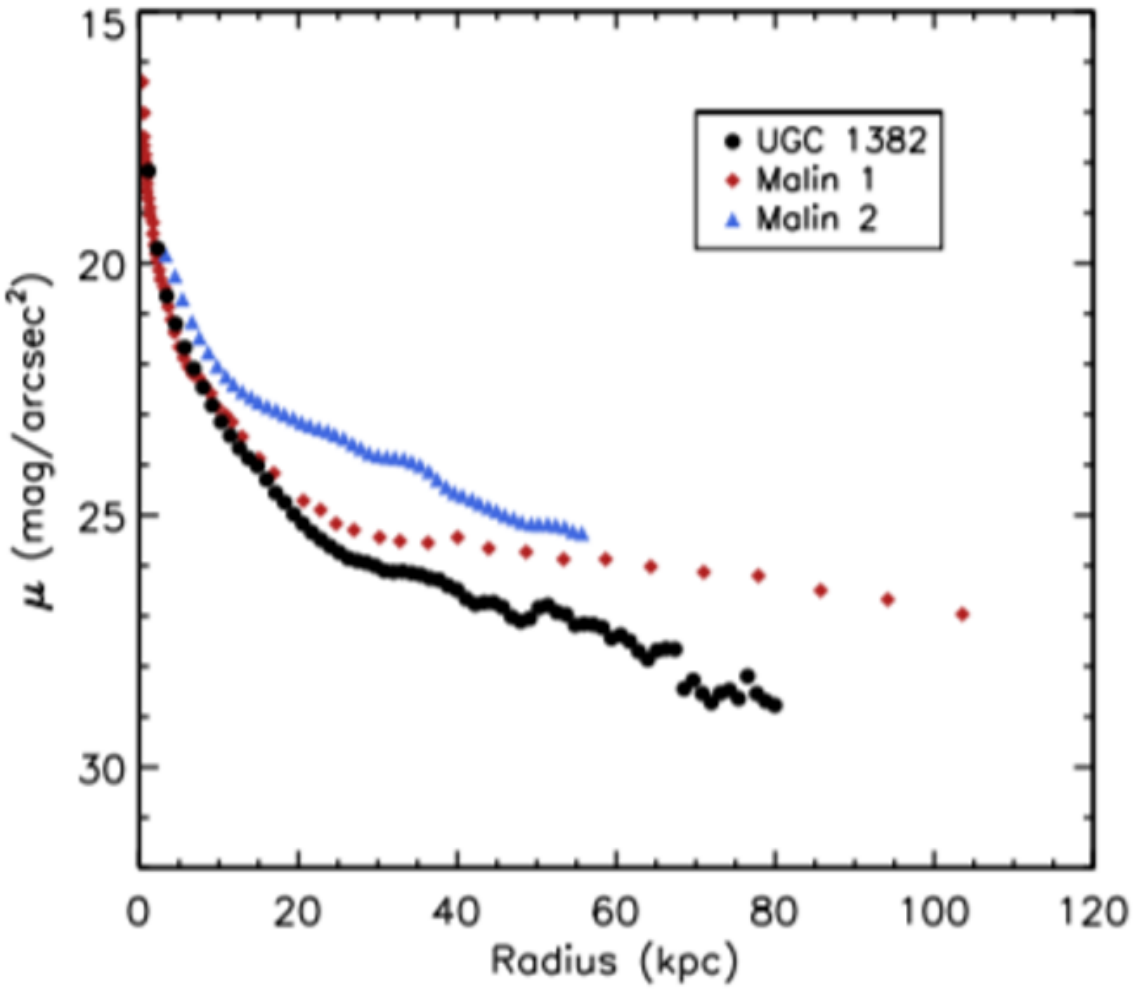

Figure 1.6 Figure reproduced from Hagen et al. (2016). r-band radial profiles of Malin 1, Malin 2, and UGC 1382.

The formation histories of GLSB galaxies is not yet well understood, although there are a few competing models for their evolution. The main scenarios proposed for their formation are divided into catastrophic collision, secular bar evolution, or dark matter properties based models. Zhu et al. (2018) propose a catastrophic collision model which reproduces a gas rich giant disk galaxy. Meanwhile, Noguchi (2001) propose a transformation of High Surface Brightness galaxy spirals to GLSBs by dynamical bar evolution processes which flatten the disk density over time. Any or some combination of these possible formation histories may apply to different GLSB case studies.

Noguchi (2001) discussed the transformation of normal HSB spirals to GLSBs through dynamical evolution due to the bar, which induces non-circular motions and radial mixing of disc matter that flattens the disc density profile over time. In this scenario barred galaxies would expand in radius as the bar evolves. However, LSB disks generally lack bars and strong spiral arms (Bothun et al., 1997). Boissier et al. (2016) determine that the surface brightness and color of GLSBs can be reproduced with a low surface density disk slowly forming stars with no significant collisional event. Meanwhile, Kasparova et al. (2014) and Saburova (2018) find unusual properties of the dark matter halo (large radial size and low central density) could result in the production of GLSBs. These galaxies typically have very massive dark matter halos (Das, 2013) which may contribute to their stability. When there is spiral structure observed, GLSBs are usually classified as very late type (Sc or Sd) galaxies (Impey & Bothun, 1997), except in those cases where there exists a prominent bulge component. These bulgier GLSBs have a tendency toward tightly wound spiral arms (Das, 2013).

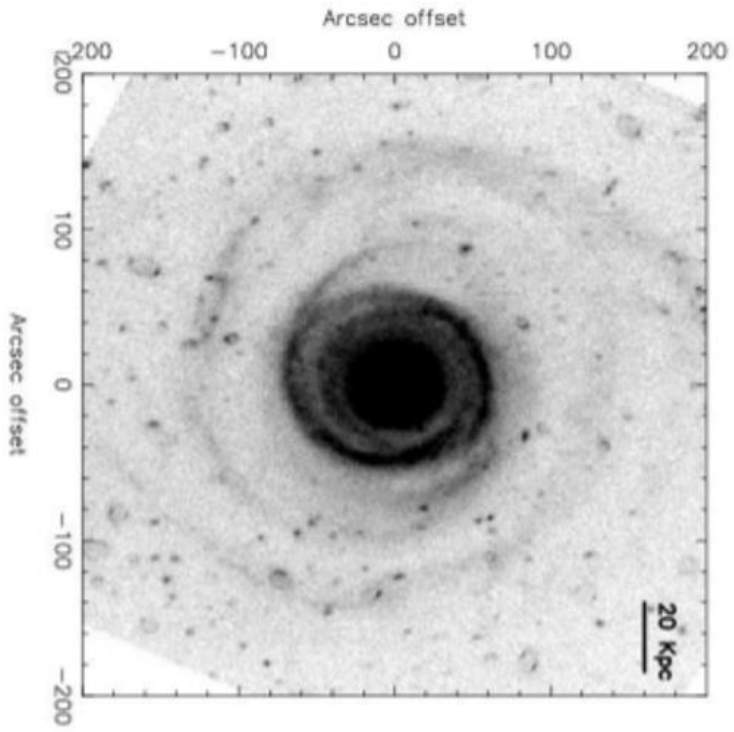

Figure 1.7 Figure reproduced from Das (2013). Disk, ring-like structure, and spiral arms of the Giant Low Surface Brightness Galaxy UGC6614.

1.7 Hoag's Object and Hoag Type Galaxies

Hoag's Object (Hoag,1950) is a galaxy characterized by a spheroidal central bulge with a bright blue star forming ring surrounding the bulge. Observations of the galaxy have measured the mass of the ring to be ~1/3 the mass of the central bulge, so the mass of the ring is comparable to that of the core (Schweizer et al 1987, Finkelman et al. 2011, Brosch et al, 2013). Bannikova (2018) explore the stability of orbits in such a system and find a Lagrangian circle (LC) of unstable equilibrium and an Outermost Stable Circular Orbit (OSCO) for systems of this type. The gap between the core and the ring is maintained by the instability of orbits between the OSCO and LC. While the ring gap is self reinforcing, any presence of spiral structure is shown to be dissipative of rings (Berrier & Sellwood, 2015).

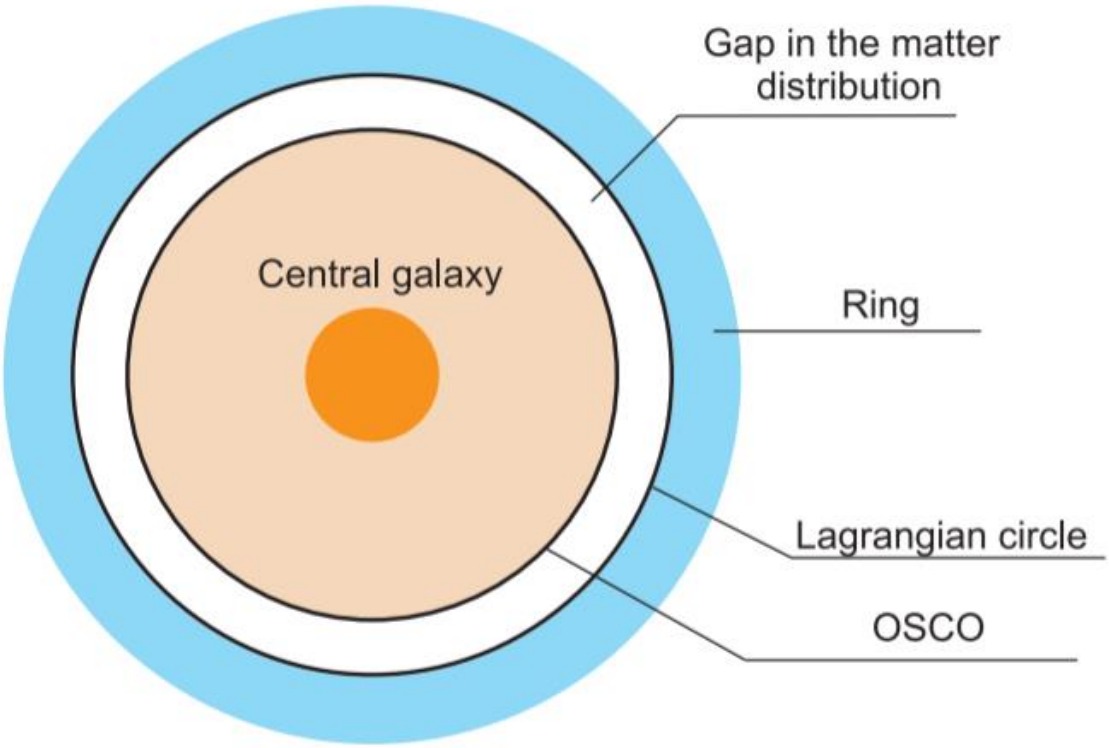

Figure 1.8: Figure reproduced from Bannikova (2018). Structure of a Hoag type galaxy showing the gap in the matter distribution located between the OSCO and LC.

There exist a few analogs to Hoag's Object in the literature (Moiseev et al. 2015, Finkelman & Brosch 2011, Mutlu Pakdil et al. 2017), which we will call Hoag type galaxies. These contain varying degrees of spiral structure in addition to the canonical core-ring setup of Hoag's Object. UGC 4599 is one such nearby Hoag type galaxy with a similar non-barred inner core plus star forming ring structure (Finkelman & Brosch, 2011). In addition, we find UGC 4599 to also contain an extended very faint disk and spiral structure, making it a GLSB analog for Hoag's Object. The presence of the spiral structure may dissipate the ring in UGC 4599 over time (Berrier et al. 2015) and suggests a relatively recent age for the ring.

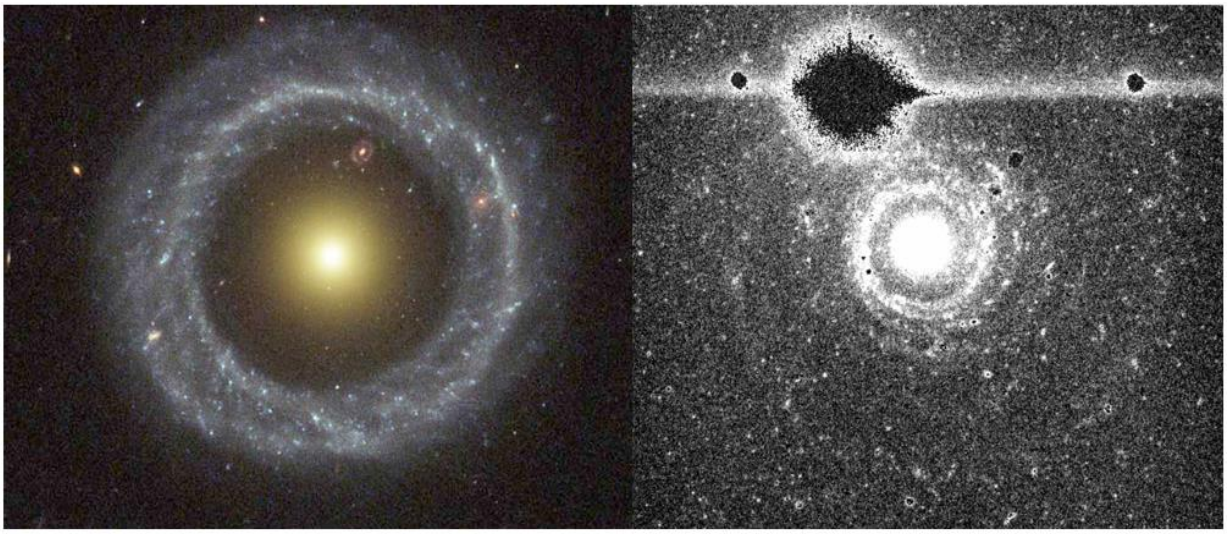

Figure 1.9 Left: Color image of Hoag's Object. Image by Lucas, R., Hubble Heritage Team, NASA. Yellow core and blue ring structure of Hoag's Object are clearly visible.

Right: UGC 4599 u band image showing similar core-ring structure as Hoag's Object, but with an extended faint disk and spiral structure.

1.8 Outline

This doctoral dissertation is comprised of three lead author publications, two of which have been submitted for publication in peer-reviewed scientific journals. Chapter 2, "Pitch Angle Distribution Function of Local Spiral Galaxies and Its Role in Galactic Structure" examines the pitch angle distribution and black hole mass functions of a set of Carnegie-Irvine Galaxy Survey (CGS) galaxies and identifies possible populational differences between earlier and later Hubble type spirals in terms of black hole mass. Chapter 3, "UGC 4599: Revealing the Extended Structure of a Giant Low Surface Brightness Hoag's object analog with HERON", observes an extremely low surface brightness disk and spiral structure surrounding the star forming ring of UGC 4599. Chapter 4, "An Assessment of Capabilities and Limitations of Logarithmic Spiral Arm Pitch Angle Measurement Techniques", studies selection effects and biases in the pitch

angle measurement of spiral galaxies at low signal to noise ratios, to the end of extending the SMBH mass – pitch angle relation to higher redshifts. Finally, in Chapter 5, we summarize the overall results and implications of this dissertation.

1.9 Bibliography

Adams, F. C., Graff, D. S., & Richstone, D. O. 2001, ApJL, 551, L31, doi: 10.1086/319828

Athanassoula, E. 2012, MNRAS, L505

Athanassoula E., Romero-G´omez M., Masdemont J.J., 2011, Memorie della Societa Astronomica Italiana Supplementi, 18,97

Berrier, J. C., Sellwood, J. A., 2015, ApJ, 799, 213

Berrier, J. C., Davis, B. L., Kennefick, D., Kennefick, J. D., Seigar, M. S., Barrows, R. S., Hartley, M.,
Shields, D., Bentz, M. C., & Lacy, C. H. S. 2013, The Astrophysical Journal, 769, 132

Bannikova E., 2018, MNRAS, 476, 3, 3269-3277

Brosch N., Finkelman I., Oosterloo T., Jozsa G., Moiseev A., 2013, MNRAS, 435, 475

Cattaneo, A., Haehnelt, M. G., & Rees, M. J. 1999, MNRAS, 308, 77, doi: 10.1046/j.1365-8711.1999.02693.x

Ciambur B. C., 2015, ApJ, 810, 120

Ciambur B. C., 2016, PASA, 33, e062

Currie, T., Muto, T., Kudo, T., et al. 2014, ApJ, 796, L30 de Val-Borro, M., Edgar, R. G., Artymowicz, P., et al. 2006, MNRAS, 370, 529

Davis, B. L., Graham, A. W., & Seigar, M. S. 2017, MNRAS, 471, 2187

Davis, B. L., Kennefick, D., Kennefick, J., et al. 2015, ApJL, 802, L13

Davis, B. L., Berrier, J. C., Shields, D. W., Kennefick, J., Kennefick, D., Seigar, M. S., Lacy, C. H. S., & Puerari, I. 2012, ApJS, 199, 33

Dieleman, S., Willett, K.W., & Dambre, J. 2015, Mon. Not. R. Astron. Soc., Volume 450, Issue 2, 21 June 2015, Pages 1441- 1459

Elmegreen, D.M., Astrophys. J. Suppl. **47**, 229 (1981)

Finkelman I., Moiseev A., Brosch N., Katkov I., 2011, MNRAS, 418, 1834

Gerola, H. & Seiden, P. E. 1978, ApJ, 223, 129

Goldreich, P. & Lynden-Bell, D. 1965, MNRAS, 130, 125

Goldreich, P., & Tremaine, S. 1980, ApJ, 241, 425

Goldreich P., Tremaine S., 1982, ARA&A, 20, 249

Goodman, J., & Rafikov, R. R. 2001, ApJ, 552, 793

Grady, C. A., Muto, T., Hashimoto, J., et al. 2013, ApJ, 762, 48

Graham, A. W. 2016, Galactic Bulges, 418, 263, doi: 10.1007/978-3-319-19378-6 11
Graham, A. W., Driver, S. P., Allen, P. D., & Liske, J. 2007, MNRAS, 378, 198

Grand, R. J. J., Kawata, D., & Cropper, M. 2012, ArXiv e-prints

Haehnelt, M. G., & Kauffmann, G. 2000, MNRAS, 318, L35, doi: 10.1046/j.1365-8711.2000.03989.x

Harsoula, M. & Kalapotharakos, C. 2009, MNRAS, 394, 1605

Jog C. J., 1992, ApJ, 390, 378

Kaufmann, D. E. & Contopoulos, G. 1996, A&A, 309, 381

Kennicutt, R., J., & Hodge, P. 1982, ApJ, 253, 101, doi: 10.1086/159614

Kennicutt, R. C., J. 1981, AJ, 86, 1847, doi: 10.1086/113064

Kormendy, J. 1981, in Cambridge Univ. Press, Vol. 153, , 111

Loeb, A., & Rasio, F. A. 1994, ApJ, 432, 52, doi: 10.1086/174548

Lin, C. C. & Shu, F. H. 1964, ApJ, 140, 646

Masters, K., Lintott, C., Hart, R., Kruk, S., Smethurst, R., Casteel, K., Keel, W., Simmons, B., Stanescu, D., Tate, K., Tomi, S., 2019, MNRAS, 487, 2, 1808-1820

Marconi, A., Risaliti, G., Gilli, R., Hunt, L. K., Maiolino, R., & Salvati, M. 2004, MNRAS, 351, 169
Michikoshi, S., & Kokubo, E. 2014, ApJ, 787, 17

Monaco, P., Salucci, P., & Danese, L. 2000, MNRAS, 311, 279, doi: 10.1046/j.1365-8711.2000.03043.x

Muto, T., Grady, C. A., Hashimoto, J., et al. 2012, ApJ, 748, L22

Nelson R. P., 2005, A&A, 443, 1067

Nelson R. P., Papaloizou J. C. B., 2004, MNRAS, 350, 849

Peng C. Y., Ho L. C., Impey C. D., Rix H.-W., 2002, AJ, 124, 266

Peng, C. Y., Ho, L. C., Impey, C. D., & Rix, H. W. 2007, in Bulletin of the American Astronomical Society, Vol. 39, American Astronomical Society Meeting Abstracts, 804

Rich, R. M., Brosch, N., Bullock, J., et al. 2017, in Formation and Evolution of Galaxy Outskirts, ed. A. Gil de Paz, J. H. Knapen, & J. C. Lee, Vol. 321, 186–189

Rosen, P.A., Tyler, G.L., Marouf, E.A., Lissauer, J.J., Icarus, 93 (1991), pp. 25-44

Salo, H., Nature, 359:619–621, 1992.

Schweizer F., Ford Jr. W. K., Jedrzejewski R., Giovanelli R., 1987, ApJ, 320, 454
Seiden, P. E. & Gerola, H. 1979, ApJ, 233, 56 —. 1982, Fund. Cosmic Phys., 7, 241

Seigar, M. S., Kennefick, D., Kennefick, J., & Lacy, C. H. S. 2008, ApJ, 678, L93

Seigar, M. S., & James, P. A. 1998a, MNRAS, 299, 672 —. 1998b, MNRAS, 299, 685

Shields, D. W., Boe, B., Pfountz, C., et al. 2015a, ArXiv e-prints.
https://arxiv.org/abs/1511.06365 —. 2015b, Spirality: Spiral Arm Pitch Angle Measurement, Astrophysics Source Code Library. http://ascl.net/1512.015

Shu F. H., 1984, in Greenberg R., Brahic A., eds, Planetary Rings. U. of Arizona Press, pp 513–561

Silk, J. & Rees, M. J. 1998, A&A, 331, L1

Stetson, P. B. 1987, PASP, 99, 191

Toomre, A. 1964, ApJ, 139, 1217

Toomre, A. 1981, Structure and Evolution of Normal Galaxies, 111

Tully, R. B., & Fisher, J. R. 1977, A&A, 500, 105

Vika, M., Driver, S. P., Graham, A. W., & Liske, J. 2009, MNRAS, 400, 1451

Zhu Z., Dong R., Stone J. M., Rafikov R. R., 2015, ApJ, 813, 88

2 Pitch Angle Distribution Function of Local Spiral Galaxies and Its Role in Galactic Structure

2.1 Abstract

We present an analysis of the Pitch Angle Distribution Function (PADF) and Black Hole Mass Function (BHMF) of a sample of nearby galaxies selected from the Carnegie-Irvine Galaxy Survey (CGS). Our subset consists of spiral galaxies with $M_B > -19.12$ and limiting luminosity distance $L_D < 25.4$ Mpc (z=0.00572). These constraints result in a set of 74 spiral galaxies, 51 with measurable pitch angles. This is an extension of work by Davis et. al on a more luminous (M_B ><-19.12) subset containing all of the late-type CGS galaxies out to $L_D < 25.4$ Mpc. Combining these two subsamples of local galaxies yields a group restricted only in luminosity-distance rather than both luminosity-disance and M_B. We produce a BHMF for this combined sample, representative of spiral galaxies in the local univers

The fainter subset presented here is morphologically distinct from its brighter counterpart, with a higher percentage of Sc and Sd classified galaxies. However, we find the pitch angle distributions of the two samples are not strongly dissimilar. We explore some indications of populational differences as expressed through the distributions of galactic spiral arm pitch angles (and resulting BHMFs) of the two samples. These differences are especially expressed on the high pitch angle, or low Supermassive Black Hole (SMBH) mass tail of the distribution. Our data show a divide in the pitch angles of the a-c Hubble types and the cd, d, m types, with a-c types having tighter spiral arms on average. The cd, d, and m type galaxies therefore represent the lower mass end of spiral galaxies and form a mass distribution distinct

from their a-c counterparts. Incorporation of the low mass end of late type galaxies into the BHMF is results in a more complete local BHMF.

2.2 Introduction

Supermassive Black Holes (SMBHs) reside at the center of most galaxies (Richstone et al. 1998; Schodel et al. 2002). There is strong evidence supporting proposed relationships among the mass of the central SMBH and various properties and features of their host galaxies (for thorough review, see Graham et al. 2015, and references therein) and (Shu 2016). Given that black hole masses correspond to morphological features of their host galaxies, a comprehensive census can be undertaken to characterize the distribution of SMBH masses, A Black Hole Mass Function (BHMF) in the local universe. Extension of the BHMF to higher redshift galaxies would advance studies of galactic evolution through the time dependency of SMBH masses. The local census offers a snapshot of the current distribution of black hole masses in the present universe while a higher redshift study would allow a mapping of the history of the BHMF through cosmic time. Incorporation of galaxies at greater redshifts will inform changes in the BHMF through processes such as mergers, accretion, and secular evolution.

At present, the high mass end of the BHMF has been probed through observations of the most active galaxies (Dalla Bonta et al. 2009). In the local universe, a majority of large black holes reside in elliptical or lenticular galaxies. The masses of these objects are estimated through a correlation between their central velocity dispersion, σ, and the mass of the SMBH (Ferrarese & Merritt 2000; Gebhardt et al. 2000). In general, the BHMF relies on applying scaling relations to luminosity/velocity functions, and has been utilized by many authors for populations of late-

type and early-type galaxies (Salucci et al. 1999; Richstone 2002; Shankar et al. 2004; Shankar 2009; Tundo et al. 2007).

For the low mass-end of the BHMF, there is still no clear consensus as to the behavior of the distribution (Marconi et al. 2004; Shankar et al. 2004; Vika et al. 2009). A secure estimate of the low mass-end of the BHMF provides constraints on the degree of time evolution in the Eddington ratio distributions (e.g. Shankar 2009), as well as on the population of seed SMBHs (e.g. Natarajan 2011). To probe evolution of the BHMF over the lifetime of the universe, a more complete measurement of the distribution locally must be attained and modified to include galaxies of lower SMBH masses. Therefore, our exploration continues a census of black holes in late type galaxies, concentrating here on galaxies with lower absolute B-Band luminosities. As we will see, these galaxies represent the low mass tail of galactic black hole masses.

The most commonly used method of measurement for SMBH masses of early type galaxies is the M-σ relation between the mass of the black hole and the central stellar velocity dispersion of the galaxy. This relation has been extensively adopted to estimate the masses of early type galaxies in order to establish a BHMF for those morphologies (Franceschini et al. 1998; Graham et al. 2007). Another widely used mass measurement method for early type galaxies is the Sersic Index (Savorgnan et al. 2013). Spiral galaxies are structurally complex and require extensive bulge/disk decomposition before attempting to calculate either the central σ or an accurate Sersic Index value. Neither of these methods have been convincingly shown to be effective in measuring SMBH masses for late type galaxies.

Here we use a correlation between the SMBH mass and the spiral galaxy pitch angle as proposed in Seigar et al. (2008) and Berrier et al. (2013), and developed further in Davis et al. (2015). According to the M_{BH}-P_{spiral} relation, galaxies with larger SMBH masses will have more

tightly wound spiral arms with lower pitch angles, whereas galaxies with lower SMBH masses will have looser spirals with higher pitch angles. This M_{BH}-P_{spiral} relation has a few advantages over past techniques for measurement of SMBH masses in late type galaxies. M_{BH}-P_{spiral} relation has less a tighter correlation than other methods when applied to disk galaxies. More importantly, measuring the pitch angle of galaxy spiral arms only requires sufficiently resolved images of the galaxy rather than observationally intensive spectra. It may be, then, the best method for extending SMBH measurement in late type galaxies to higher redshifts is through the M-P relation rather than other current methods. As a result, the M-P relation is a useful method both for measuring the SMBH mass of spiral galaxies locally and at higher redshift, with the caveat that spiral structure be sufficiently resolved in imaging.

The M-P relation indirectly measures the mass of the central bulge region of spiral galaxies. Modal Density Wave Theory (Lin & Shu 1964) describes spiral structure in galaxies as a standing wave pattern of density waves. These density waves are generated by inner and outer Linblad resonance orbits in the galaxy. They propagate through the disk, amplified or damped by interactions with galactic features. The pitch angle of the spiral arms is analogous to the wavelength of a standing wave on a vibrating string. The value of pitch angle is dependent on the ratio of the mass density in the disk to the mass in the central region. The SMBH behaves like tension on the string, while the disk itself acts as the medium of the string.

This formulation of modal density wave theory has been applied effectively to the behavior of spirals in the rings of Saturn (Cuzzi et al. 1981). Spiral galaxies, though more structurally complex than the high central mass, low disk mass ideal model, nevertheless have a configuration of a centrally concentrated mass (SMBH and bulge) with a thin disk of orbiting material. Since the mass of the galactic bulge correlates well with the SMBH mass, it follows

that application of modal density wave theory to indirectly measure SMBH masses is a viable method. Unlike the end-member case of Saturn, where the disk mass is much less than the central mass, spiral galaxies have a comparatively flat mass distribution.

Spiral structures induced by density waves are also present in protoplanetary and circumplanetary disks (Perez et al. 2016; Xu & Goodman 2018; Bae et al. 2016). As the mass ratio of central mass to disk mass decreases, the logarithmic spiral arm pitch angle increases. While Saturn's ring spirals have a pitch angle much less than 1º, most spiral galaxies are closer to 20º. It has been shown in Davis et al. (2015) there is a planar relationship among the quantities of SMBH mass, pitch angle, and the mass of neutral hydrogen (proxy for disk density) in the galaxy in accordance with Density Wave Theory.

A first census of the BHMF in spiral galaxies has been conducted by Davis et al. (2014), in which a sample of spiral galaxies was selected from the CGS (Ho et al. 2011) sample of nearby galaxies with two bounds, luminosity-distance and absolute B-Band magnitude. The reasoning for these bounds was for sample completeness, as fainter galaxies might not be identified beyond a specified distance. Here we consider these fainter galaxies in the larger sample, accounting for missing galaxies by weighted correction.

2.3 Methodology and Data

2.3.1 Sample Selection

We make use of Southern Hemisphere galaxies based on the Carnegie-Irvine Galaxy Survey (CGS, Ho et al. 2011). The CGS is a project to observe 605 bright southern galaxies in

photometry and spectroscopy using Las Campanas Observatory. For this research, we utilize optical (B-band) imaging of a subsample of these galaxies.

Pursuit of a BHMF for the local universe is undertaken through the measurement of pitch angles to estimate black hole masses. The formerly defined 2014 sample provided an initial construction of the BHMF of late type galaxies, wherein the pitch angles of a volume-limited set of local spiral galaxies were measured to calculate the BHMF. Their dataset excluded galaxies below a specified luminosity (limiting magnitude M_B=19.12); beyond the distance limit chosen, some fraction of these galaxies were beyond the detection limit of the survey. Consequently, their dataset is complete (no undetected galaxies) within its distance and luminosity bounds. Yet, these set limitations necessarily exclude the lowest luminosity galaxies, which may comprise the extreme low mass end of the BHMF. We measure pitch angles for all galaxies detected within the set luminosity-distance limit, accounting for those too faint to be identified. From here, we will refer to their sample as the bright sample and our sample as the faint sample.

Our sample eliminates the limiting luminosity constraint to probe lower luminosity galaxies (see Figure 2.1). From this, we selected spiral galaxies within a set defined by a limiting luminosity (redshift-independent) distance, D_L= 25.4 Mpc, where the distances are found by primary techniques. This produces a volume-limited (but no longer magnitude limited) sample consisting of the 140 spiral galaxies of Davis et al. (2014) plus 74 faint galaxies in this study.

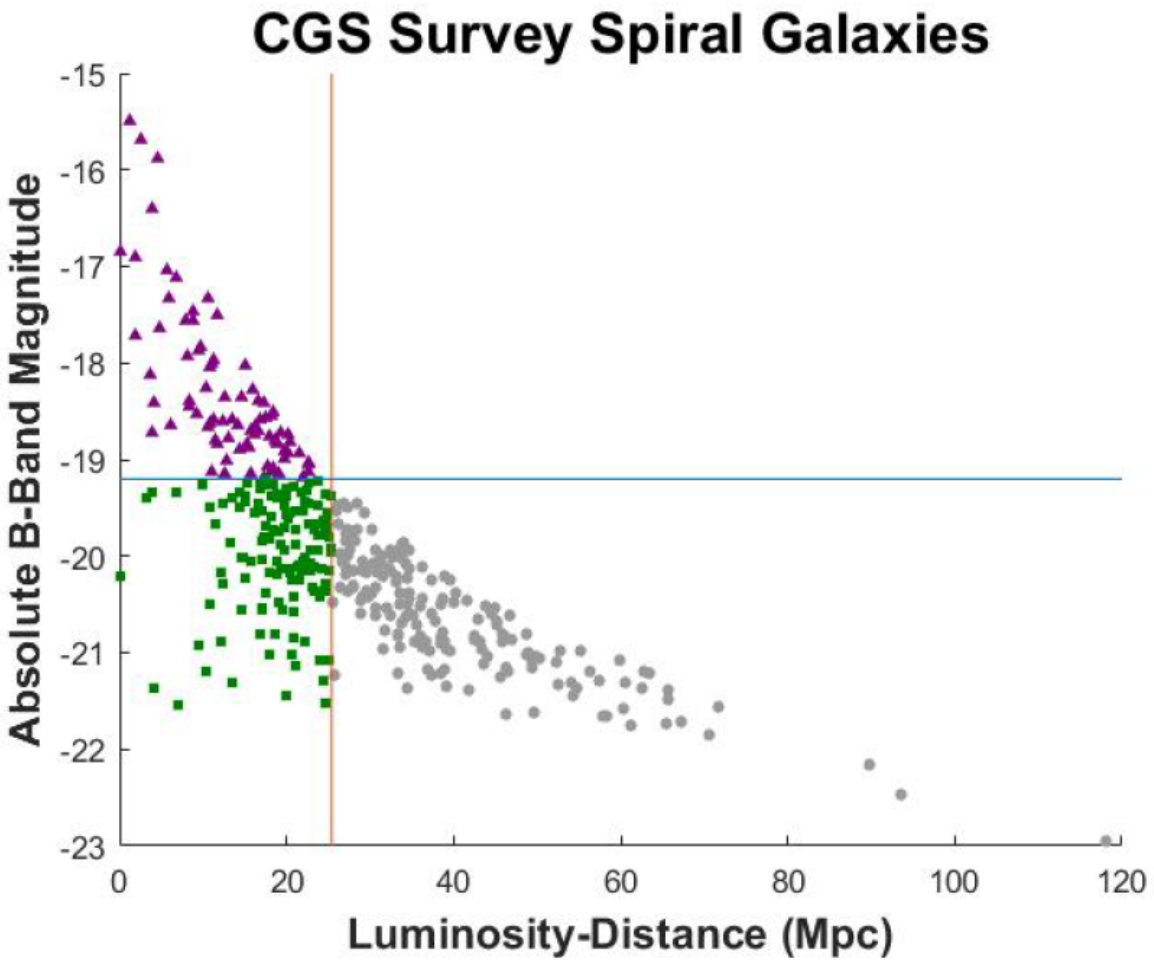

Figure 2.1: Luminosity Distance vs. Absolute M_B magnitude for CGS Survey galaxies. Davis et al. (2014) sample (green squares); Faint galaxy sample (purple triangles).

2.3.1.1 Sample Comparison

Here we consider the physical properties of the Davis sample compared to our fainter set. Two such properties are the Hubble type classification and modality (number of arms) of the galaxies (see Figure 2.2). Differences in these characteristics are indicators of distinct morphological populations of spiral galaxies comprising the two samples. In comparing the two sets of galaxies, the faint sample contains many more c and d type spirals, implying less bulge

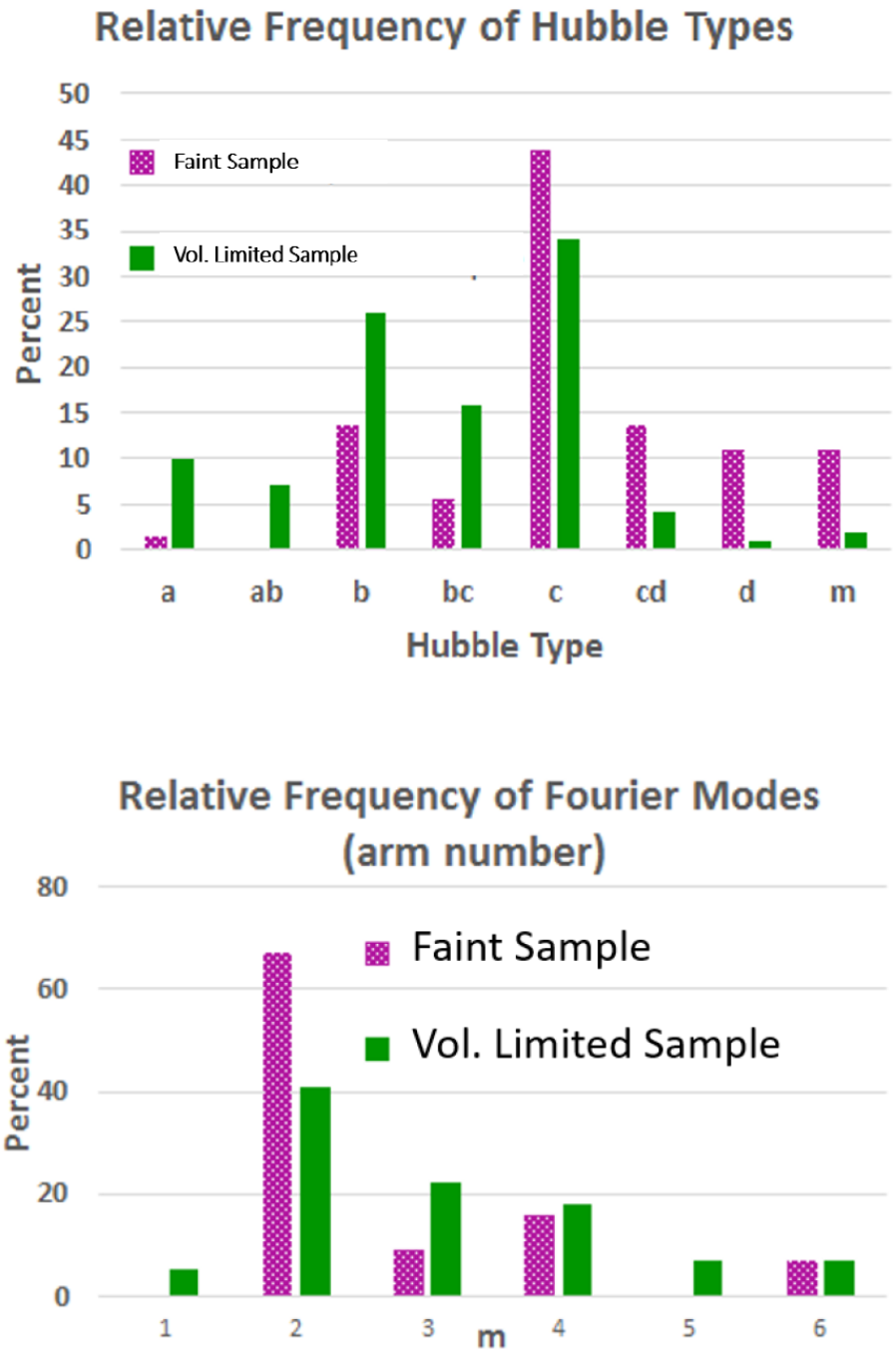

Figure 2.2: Top: Hubble types of all galaxies from each sample. The bright sample is comprised of spirals of medium arm winding (b, bc, c), while the faint sample favors less bulge dominated spirals with a high pitch angle sub-population (c, cd, d, m). Hence, a morphological difference is expressed between the two selections of galaxies.

Bottom: Number of arms for the two samples is similar, with two armed galaxies being most abundant in both. Notably, the faint sample is partially comprised of flocculent galaxies which often evade pitch angle measurement or arm number attribution, as opposed to the more accurately measured grand design spirals which are common to the earlier Davis sample.

dominated and looser spiral armed galaxies on average. According to the Tully-Fisher relation (Tully & Fisher 1977) the luminosity of a spiral galaxy relates to its rotational velocity, which is determined in part by its central SMBH and bulge mass. The lower surface brightness galaxies of our sample are therefore likely to be less massive overall and less bulge dominated. The difference in Hubble classifications between the two samples confirms this expectation.

While the galaxies of the faint sample are different in Hubble type, their distribution of arm number mirrors that of Davis et al. (2014), where arms are distinguishable. Dominant symmetry in both sets of galaxies is m=2 by far, with the faint sample showing an even higher percentage of two armed spirals. There is also an excess of flocculent galaxies in the faint sample. These generally fainter galaxies have a tendency toward less organized structure, with symmetry either unclear, having a low arm-interarm contrast, or being more difficult to identify with more spurs than grand design arms. Assigning a proper arm count to these messy galaxies is difficult. For fainter galaxies, it may simply be easier to resolve a two armed spiral than to count the number of arms in a less organized structure. This high number of flocculent galaxies explains the relative excess of m=2 and missing m>2 modes in the faint sample. As flocculent galaxies do not often have a dominant symmetry mode assigned to them, these missing assignments at least partially accounts for the dearth of galaxies with higher symmetry modes than m=2 and corresponding excess of m=2 galaxies in the faint sample.

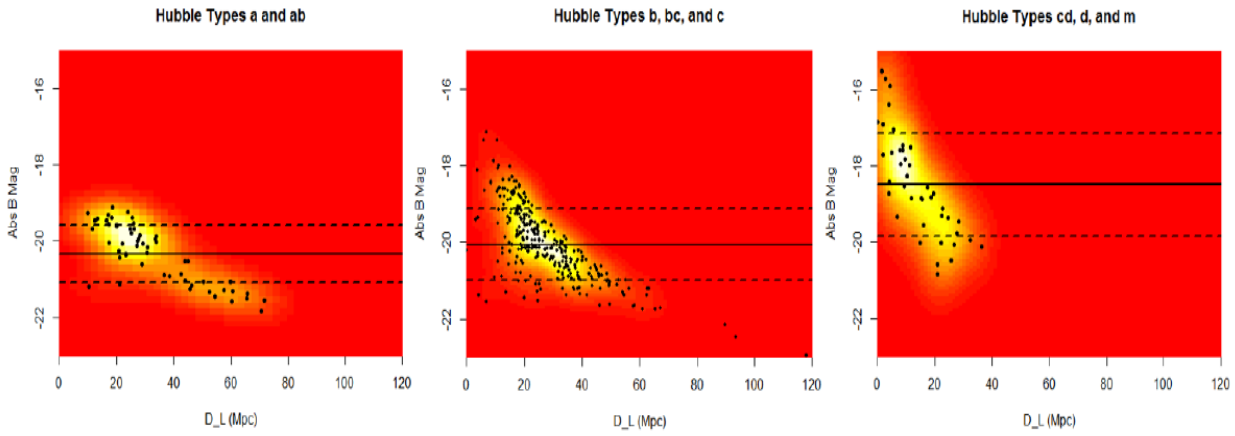

Figure 2.3: Mean absolute M_B and standard deviation of the full CGS sample, sorted by Hubble type. Hubble type a and ab spirals as reported in the CGS are confined to roughly M_B=-19 and brighter, with a mean near M_B=-20.5. Galaxies identified as b, bc, and c span nearly the whole sample in magnitude. Galaxies identified as c, cd, and m have a mean near M_B=-18.5. It is expected that galaxies with later Hubble types would have lower surface brightness, especially m dwarfs. Galaxy types through c in the CGS all have similar mean M_B, while the latest types begin to deviate toward lower brightness.

2.3.2 Galactic Spiral Arm Pitch Angle Measurement

2.3.2.1 2DFFT

Measurement of galactic logarithmic spiral arm pitch angle is achieved through utilization of a modified two dimensional fast Fourier transform code called 2DFFT (Davis et al. 2012, 2016; Puerari et al. 2000). This package decomposes digital images of spiral galaxies into superpositions of spirals of various pitch angles (P) and number of arms, or modality (m). Measurement using 2DFFT is most effective when applied to face-on galaxies. Galaxies at higher inclination to line of sight must be deprojected to a face-on orientation in pre-processing. Deprojection position and inclination angle are measured with the IRAF routine ELLIPSE. The intrinsic ellipticity of spiral galaxies is generally nonzero, though small, with an average of 0.215±0.013 (Rodriguez & Padilla 2013). We here assume circular galaxies for our

deprojections. Small errors in deprojection (<10º of inclination) do not greatly alter the measurement of pitch angle (Davis et al. 2012). Deviations from circularity of disks in these galaxies may increase the error value for pitch angle measurements.

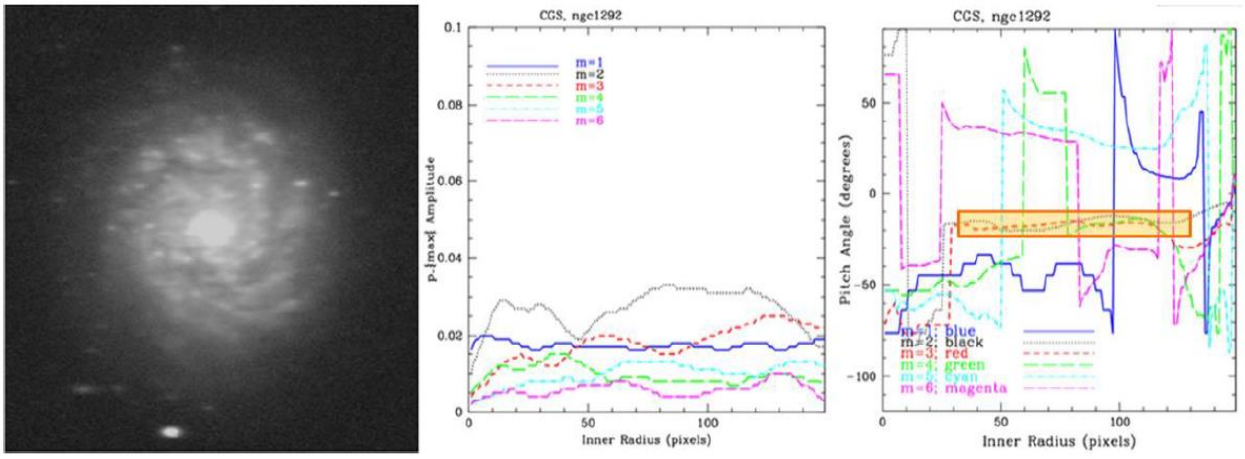

Figure 2.4: Example of spiral arm pitch angle measurement for galaxy NGC 1292 using 2DFFT. Left: Galaxy image in B-Band. Middle: Amplitude of each Fourier mode, with m=2 symmetry being the most prominent for this galaxy. Right: 2DFFT results, with region of stable pitch angle measurement highlighted. Notice the stable region for the m=2 mode also shows stability for some less dominant, higher orders of symmetry, in this case m=3 and m=4. The two arm symmetry is distinguishable in the image, though this flocculent galaxy blends the m=2 spiral with arm segments in different symmetry configurations.

Within the 2DFFT routine, the center of the galaxy and an outer radius are specified by the user, and pitch angles are measured in annuli with an inner and outer radius. The inner radius is iterated from zero by integer pixel radius values to one less than the outer radius of the galaxy. This produces a set of measurements all with the same outer radius but of varying inner radius. Often, the largest annuli will contain the core of the galaxy and any bar features present, resulting in a poor measurement for pitch angle. An inner radius of measurement, outside of which the pitch angle is relatively stable (ideally a large fraction of the total galactic radius) is

selected (see Figure 2.4). On the other end of the measurement, the smallest annuli are in the lowest surface brightness outer regions of the galaxy where signal to noise ratios are lower. These annuli also contain less of the rotation of the spiral as the annulus shrinks. These small outer annuli with unstable pitch angles are excluded. As a result, the measurements with small inner radii or large inner radii compared to the galaxy radius are excluded while a region of medium annuli with stable pitch angle measurements is used to find the dominant pitch angle in the galaxy. This stable region should be characterized by a small variation in the measured value for pitch angle. The error in pitch angle is dependent on the standard deviation of the pitch angle within the stable region as well as the size of the stable region compared to the size of the galaxy. 2DFFT also returns the amplitude of each of the first six non-zero harmonic modes. The dominant mode (number of arms) corresponds to the frequency with maximum amplitude. Full details of our methodology for measuring pitch angles may be found in (Davis et al. 2012).

2.3.2.2 Use of GALFIT in Galaxies with Low Arm-Interarm Contrast

GALFIT version 3.0 is a two dimensional fitting algorithm for galaxies as described in Peng et al. (2007). In addition to elliptical light profile fitting (Sersic profiles, etc.), the up-to-date version of GALFIT allows detailed fitting of complex and non-axisymmetric features in galaxies such as spiral arms, bars, rings, tidal tails, etc. This has proven to be a valuable resource in addressing the less structured spiral galaxies.

There are two beneficial approaches in utilizing GALFIT to assist in pitch angle measurement for a given galaxy. The first is to fully model the galaxy in question, including spiral structure, and extract the pitch angle of the spirals from the model. The main advantage in

this case is foreground stars and clumps in the galaxy structure go unmodeled and instead the focus is on reproducing radial light profiles and measurable spiral arms. A disadvantage to model fitting of spiral arms with GALFIT is the time cost per galaxy to fit a reasonable model. Spiral arms produced through GALFIT modeling behave a bit differently from real arms and may be difficult to match to real galaxy features. When working with large samples of galaxies, basic radial fitting without non-axisymmetric components is the preferred usage, and is the method employed for all galaxies in this sample.

The second possibility for incorporating GALFIT models into pitch angle measurement is to remove the radial light profile of the galaxy from the image before performing 2DFFT. This option offers a more practical route than full modeling. This technique is rapid to implement, and as a consequence is not prohibitively time intensive for measuring large samples of galaxies. Generally, a one or two component Sersic profile (Sersic 1963) is fit to the target galaxy and removed, where the residual image primarily retains the spiral structure. Fitting the galaxy to an elliptical Sersic profile is especially helpful in increasing the relative strength of spiral features at outer radii, as much of the central brightness of the galaxy is removed for fitting. Galaxies before GALFIT light profile removal may be considered as “center-weighted” as most of the brightness of the galaxy is centrally located. By flattening the radial light profile of the galaxy with GALFIT, subsequent pitch angle measurements with 2DFFT tend to be more stable and reach higher galactic radii (see Figure 2.5) as opposed to favoring the inner radius of a given annulus. By employing Sersic profile subtraction, we obtain more and better pitch angle measurements than would be possible otherwise.

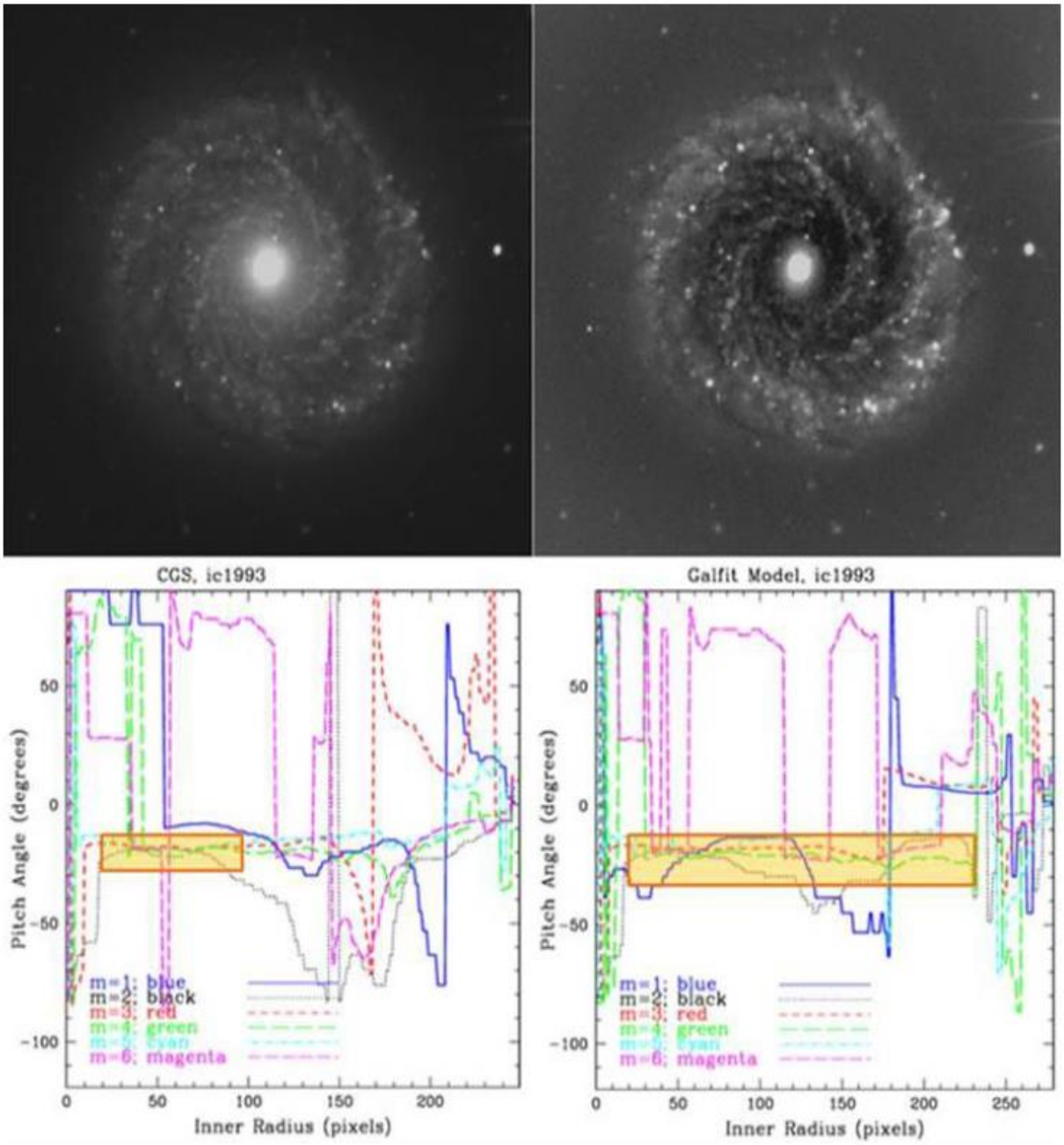

Figure 2.5: Improved 2DFFT measurement of spiral arm pitch angle for IC 1993 by means of GALFIT. Left: Original B-Band image and corresponding pitch angle measurement. Right: Modified image using GALFIT to remove a Sersic profile from the galaxy, amplifying the visibility of the spiral arms. 2DFFT is capable of pitch angle measurement for both images; the stable region for the GALFIT corrected image covers a larger range of galactic radius with a smaller standard deviation, finding a lower measurement error.

2.3.2.3 Symmetrical Components

Another technique for enhancing the accuracy of pitch angle measurements is to extract the symmetrical components of the target galaxy. Such a symmetrical component image is created by dividing the original image into pixel pairs/groups, co-radial from the center of the galaxy and symmetrically distributed in rotation angle (Elmegreen et al. 1992). Pairs/groups then adopt the lowest pixel value among them as the value for all of them. For example, for m=2 symmetry, all points radially opposed from one another at 180º adopt the lowest pixel value of each pair; for m=4, the lowest pixel value of the groups of four pixels 90º apart, and so on.

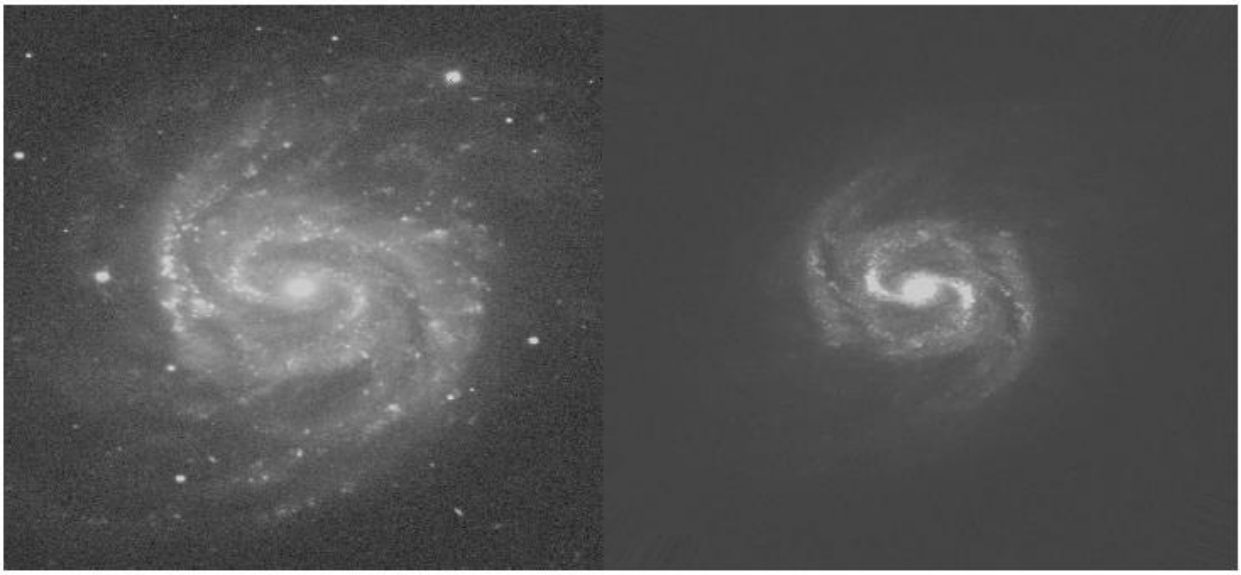

Figure 2.6: m=2 symmetrical component of galaxy NGC 1042. Left: Original B-Band image. Right: Symmetrical component image. Foreground stars and asymmetric bright features are removed and symmetrical features remain, allowing for more accurate measurement of spiral arm pitch angles. Taking symmetrical components, where applicable, is a more rapid process for improving measurement than other methods, such as star subtraction. However, this comes at a cost of loss of information about the galaxy, as arm segments which do not fit the symmetry of the symmetrical component taken are removed.

This method of image preprocessing is applicable to galaxies where the arm symmetry is apparent, but where foreground stars or structural irregularities cause inaccurate measurements of the overall behavior. Taking symmetrical components provides a trade with tension between two characteristics: effective resolution and structural irregularities. They tend to not only remove or reduce the effects of error inducing features such as foreground stars, minor arm spurs, and flocculence from the image (see Figure 2.6), but also remove detail from the galaxy. The effective pixel count of the galaxy is reduced by approximately a factor of the symmetry number as information is lost through taking the symmetry. In most cases, this is a worthwhile trade-off of lost resolution for improved measurement of symmetrical features with lower associated error. For galaxies with many foreground stars, a full star subtraction using DAOPHOT in IRAF or similar may be advisable before taking symmetrical component images for final measurement. Both GALFIT model subtractions and symmetrical component images may be introduced individually or in sequence to galaxy images. Thusfar, the most stable pitch angle measurements are obtained by first removing the radial Sersic profile and subsequently creating a symmetrical component image of the residual from the Sersic profile fit. Applying these techniques in tandem often increases the measurable radius range for the galaxy by 10-25% of the galactic radius and reduces the error in pitch angle measurement for the galaxy by an average of roughly 2º in our error assignment.

2.3.3 Data

Our sample of galaxies draws 74 spiral galaxies from the CGS, with absolute M_B fainter than -19.12 and limiting luminosity distance less than 25.4 Mpc. Of these, galactic spiral arm pitch angles were measured for 51 galaxies. Of the 23 galaxies which we were unable to

measure, the Hubble type of the galaxy being examined greatly affected the measurement success rate. For a, b, bc, and c galaxies, the average measurement rate was 85%, whereas for cd and d galaxies the measurement rate drops to 67%. The measurement rate of Magellanic Spiral (m-type) dwarf galaxies was 0% (all 8 were not assigned a pitch angle). Measurement success did not depend strongly on the M_B of the galaxies examined as measurement failures occurred at all magnitudes. However, no galaxies fainter than M_B =-17 magnitude were successfully measured. The characteristics of measured galaxies is included in table 2.1.

2.3.4 Properties and Measurement of the Faint Sample

Any comparison between two related populations of data requires an examination of which data, if any, is likely to be missing from each population. When the Davis et al. (2014) sample was assembled, it was chosen for reasons of sample completeness, namely, galaxies within its luminosity distance and M_B bounds were selected (bright enough to be observed and identified as spirals). We relax these conditions for the faint sample but partially recover completeness by statistically accounting for missing galaxies.

There presumably exist many galaxies within the distance and luminosity limits of the faint sample which are not observed due to the brightness limits of the CGS survey. This subsample of galaxies which are too faint to be detected in the CGS are missing from our population and need to be accounted for. In addition, we fail to measure pitch angles for some fraction of the sample, with spirals classified as m-type going completely unmeasured. The faint sample is morphologically different from Davis et al. (2014), containing an excess of c, cd, d,

and m type galaxies and a dearth of a, ab, b, and bc types. Hubble types a and ab are nearly absent from the faint sample.

We separate the CGS by Hubble type into three groups to denote this populational difference in M_B, luminosity distance space (see Figure 2.3). We find a and ab galaxies to appear at M_B=-19 or brighter, with an average M_B=-20.2. Meanwhile, the cd, d, and m subgroup populates a lower brightness regime, with an average M_B=-18.5. Intermediate Hubble types span a large range of luminosities but have an average M_B consistent with the a and ab group. Even with m types removed, the cd and d group show a fainter average M_B.

Looking at the pitch angle measurement success rates in the faint sample, we find that m types have a success rate of zero, 67% for cd and d galaxies, and 85% for a, ab, b, bc, and c galaxies. Using Expectation-Maximization clustering, we divide the sample into galaxies with low pitch angle and galaxies with high pitch angle (see Figure 2.13). As expected, galaxies in the high pitch angle cluster are primarily cd and d types with a few c's. This low pitch angle cluster represents galaxies which went partially unreported in Davis et al. (2014).

Table 1. Measured pitch angles and corresponding black hole mass estimates for the CGS Faint sample galaxies.

Galaxy	Hubble Type	B_T	D_L	A_B	M_B	$\log(L/L_\odot)$	P	$\log(M/M_\odot)$
		[mag]	[Mpc]	[mag]	[mag]		[deg.]	
(1)	(2)	(3)	(4)	(5)	(6)	(7)	(8)	(9)
ESO 219-G021	SABc	12.83	14.22	0.707	−18.64	9.59	-19.93 ± 2.36	7.69 ± 0.25
ESO 265-G007	SBc	12.54	13.4	0.498	−18.59	9.57	16.41 ± 2.12	7.69 ± 0.25
ESO 271-G010	Sc	12.90	18.889	0.355	−18.84	9.67	29.54 ± 9.45	7.68 ± 0.39
ESO 383-G087	Sd	11.70	2.675	0.257	−15.69	8.42	9.59 ± 0.76	7.77 ± 0.23
ESO 384-G002	SBd	12.88	17.45	0.232	−18.56	9.56	-11.89 ± 1.45	7.69 ± 0.25
ESO 479-G004	SBd	12.79	19.4	0.066	−18.72	9.62	28.12 ± 3.40	7.69 ± 0.25
IC 1954	Sb	12.10	15.287	0.059	−18.88	9.69	18.32 ± 2.70	7.68 ± 0.26

Table 1 continued

Table 1 *(continued)*

Galaxy	Hubble Type	B_T	D_L	A_B	M_B	$\log(L/L_\odot)$	P	$\log(M/M_\odot)$
		[mag]	[Mpc]	[mag]	[mag]		[deg.]	
(1)	(2)	(3)	(4)	(5)	(6)	(7)	(8)	(9)
IC 1993	SABb	12.52	14.7	0.036	−18.35	9.48	-20.46 ± 2.48	7.70 ± 0.25
IC 2000	SBc	12.82	20.08	0.036	−18.73	9.63	-24.14 ± 1.93	7.69 ± 0.23
IC 2056	Sbc	12.80	20.5	0.067	−18.83	9.66	16.34 ± 5.06	7.68 ± 0.38
IC 2627	SABb	12.68	18.48	0.436	−19.09	9.77	-33.18 ± 23.55	7.68 ± 0.74
IC 5201	Sc	11.95	14.4	0.043	−18.88	9.69	34.92 ± 23.11	7.68 ± 0.70
IC 5273	SBc	12.74	16.557	0.045	−18.40	9.49	21.37 ± 6.88	7.70 ± 0.39
IC 5332	SABc	11.23	8.4	0.060	−18.45	9.52	4.99 ± 0.39	7.69 ± 0.23
NGC 24	Sc	12.14	6.889	0.071	−17.12	8.99	-25.40 ± 23.11	7.73 ± 0.94
NGC 45	SABd	11.39	9.313	0.075	−18.53	9.55	-27.98 ± 3.97	7.69 ± 0.26
NGC 247	SABc	9.72	3.587	0.066	−18.12	9.38	42.90 ± 4.84	7.70 ± 0.24
NGC 300	Scd	8.81	1.972	0.046	−17.71	9.22	33.69 ± 0.75	7.72 ± 0.22
NGC 701	SBc	12.84	22.711	0.091	−19.03	9.75	17.15 ± 1.78	7.68 ± 0.24
NGC 779	SABb	12.27	17.678	0.097	−19.06	9.76	15.58 ± 5.52	7.68 ± 0.41
NGC 1022	SBa	12.32	18.5	0.093	−19.11	9.78	22.44 ± 12.10	7.68 ± 0.58
NGC 1042	SABc	12.11	9.431	0.104	−17.87	9.28	20.71 ± 6.55	7.71 ± 0.38
NGC 1179	Sc	12.83	18.171	0.087	−18.55	9.56	-19.18 ± 5.32	7.69 ± 0.35
NGC 1249	SBc	12.78	15.854	0.060	−18.28	9.45	-17.13 ± 5.93	7.70 ± 0.41
NGC 1292	Sc	12.79	21.475	0.062	−18.93	9.71	-14.87 ± 3.37	7.68 ± 0.31
NGC 1313	SBcd	9.66	3.951	0.396	−18.72	9.62	-41.63 ± 1.08	7.69 ± 0.22
NGC 1337	SBc	12.53	16.075	0.245	−18.75	9.63	-17.57 ± 5.26	7.69 ± 0.37
NGC 1436	Sb	12.86	18.36	0.039	−18.50	9.53	-24.58 ± 4.48	7.69 ± 0.28
NGC 1487	Scd	12.33	8.9	0.043	−17.46	9.12	-69.44 ± 2.21	7.72 ± 0.22
NGC 1493	SBc	11.72	11.3	0.037	−18.58	9.57	14.21 ± 3.67	7.69 ± 0.34
NGC 1494	Scd	12.10	15.217	0.022	−18.83	9.67	22.01 ± 2.05	7.68 ± 0.24
NGC 1518	SBd	12.26	9.596	0.174	−17.82	9.27	-46.01 ± 9.83	7.71 ± 0.30
NGC 1637	Sc	11.63	10.703	0.146	−18.66	9.60	13.76 ± 1.68	7.69 ± 0.25
NGC 1688	SBcd	12.20	15.45	0.125	−18.87	9.68	-38.66 ± 0.95	7.68 ± 0.22
NGC 1744	SBc	11.71	10.853	0.148	−18.62	9.58	10.61 ± 3.75	7.69 ± 0.41
NGC 1796	SBc	12.88	10.6	0.088	−17.33	9.07	15.02 ± 2.92	7.73 ± 0.29
NGC 2082	SBb	12.73	17.978	0.210	−18.75	9.64	22.26 ± 2.41	7.69 ± 0.24
NGC 2090	Sbc	11.66	12.758	0.144	−19.01	9.74	8.29 ± 2.37	7.68 ± 0.36
NGC 2427	SABd	12.30	11.782	0.778	−18.83	9.67	20.87 ± 3.62	7.68 ± 0.28
NGC 3513	SBc	12.04	13.153	0.23	−18.79	9.65	28.76 ± 0.56	7.68 ± 0.22
NGC 4592	Sd	12.9	11.63	0.082	−17.51	9.14	40.30 ± 17.93	7.72 ± 0.49
NGC 4632	Sc	12.63	18.518	0.087	−18.79	9.65	22.92 ± 3.74	7.68 ± 0.27
NGC 4951	SABc	12.58	16.6	0.171	−18.69	9.61	18.51 ± 5.94	7.69 ± 0.39
NGC 5068	Sc	10.64	6.075	0.369	−18.65	9.59	23.60 ± 13.00	7.69 ± 0.59
NGC 5134	SABb	12.46	10.889	0.328	−18.05	9.36	-36.28 ± 5.67	7.71 ± 0.27
NGC 5556	Scd	12.81	18.75	0.254	−18.81	9.66	-14.09 ± 1.31	7.68 ± 0.24

Table 1 continued

Table 1 *(continued)*

Galaxy	Hubble Type	B_T	D_L	A_B	M_B	$\log(L/L_\odot)$	P	$\log(M/M_\odot)$
		[mag]	[Mpc]	[mag]	[mag]		[deg.]	
(1)	(2)	(3)	(4)	(5)	(6)	(7)	(8)	(9)
NGC 7361	Sc	12.82	17.2	0.06	−18.42	9.50	24.12 ± 7.22	7.70 ± 0.37
NGC 7412	SBb	11.92	12.485	0.042	−18.60	9.58	14.66 ± 2.23	7.69 ± 0.26
NGC 7421	Sbc	12.78	22.6	0.054	−19.04	9.75	20.88 ± 7.18	7.68 ± 0.41
NGC 7424	Sc	11.54	11.5	0.039	−18.80	9.66	20.24 ± 6.05	7.68 ± 0.37
NGC 7456	Sc	12.43	16.185	0.039	−18.65	9.60	-18.48 ± 7.27	7.69 ± 0.45
NGC 7496	Sb	12.9	15.02	0.036	−18.02	9.34	-36.03 ± 0.84	7.71 ± 0.22
NGC 7713	Scd	11.87	10.272	0.06	−18.25	9.43	-21.62 ± 2.78	7.70 ± 0.25
NGC 7793	Scd	9.77	4.171	0.071	−18.40	9.50	11.37 ± 1.21	7.70 ± 0.24
PGC 3853	SABc	12.62	12.6	0.48	−18.36	9.48	23.17 ± 5.45	7.70 ± 0.32

NOTE—Columns: (1) Galaxy Name. (2) Hubble type morphological classification. (3) B-Band total magnitude. (4) Luminosity distance (in Mpc). (5) B-Band extinction magnitude from Schlafly & Finkbeiner (2011). (6) B-Band absolute magnitude. (7) Luminosity. (8) Pitch angle (in degrees). (9) Black hole mass.

2.3.5 Pearson Distribution Fitting of Pitch Angles

In Davis et al. (2014), the probability density of pitch angles for their sample was calculated by creating a "binless" histogram which treats the dataset as a sum of Gaussians, with individual P measurements and their error bars representing the means and standard deviations, respectively. This histogram was then statistically fit to a probability density function (PDF) based on the statistical properties of the dataset. This skew-kurtotic-normal fit of the Pitch Angle Distribution could then be transformed into a BHMF through the M-P relation (Seigar et al. 2008; Berrier et al., 2013, Davis et al. 2017). We reproduce these calculations for the current dataset (Figure 7).

The skew-kurtotic-normal fit of the sample does not match well with the binless histogram of the sample. Low N in the faint sample may be a partial cause of irregularities between the histogram and the PDF. Furthermore, this disparity may be due to difficulties in measuring these fainter or lower contrast galaxies, as their higher associated errors potentially alter the shape of the histogram. Manually creating a best fit PDF to match the binless histogram

required much higher values of both skewness and kurtosis than the original fit from the statistics of the sample. Given the peak locations of the bright sample and faint galaxies sample match up reasonably well, the increased skew in the faint galaxies sample is interpreted mainly as a stronger tail of probability density at high (past peak) pitch angles. Moreover, excess kurtosis in the faint galaxies sample is indicative of a heavy tail to the distribution.

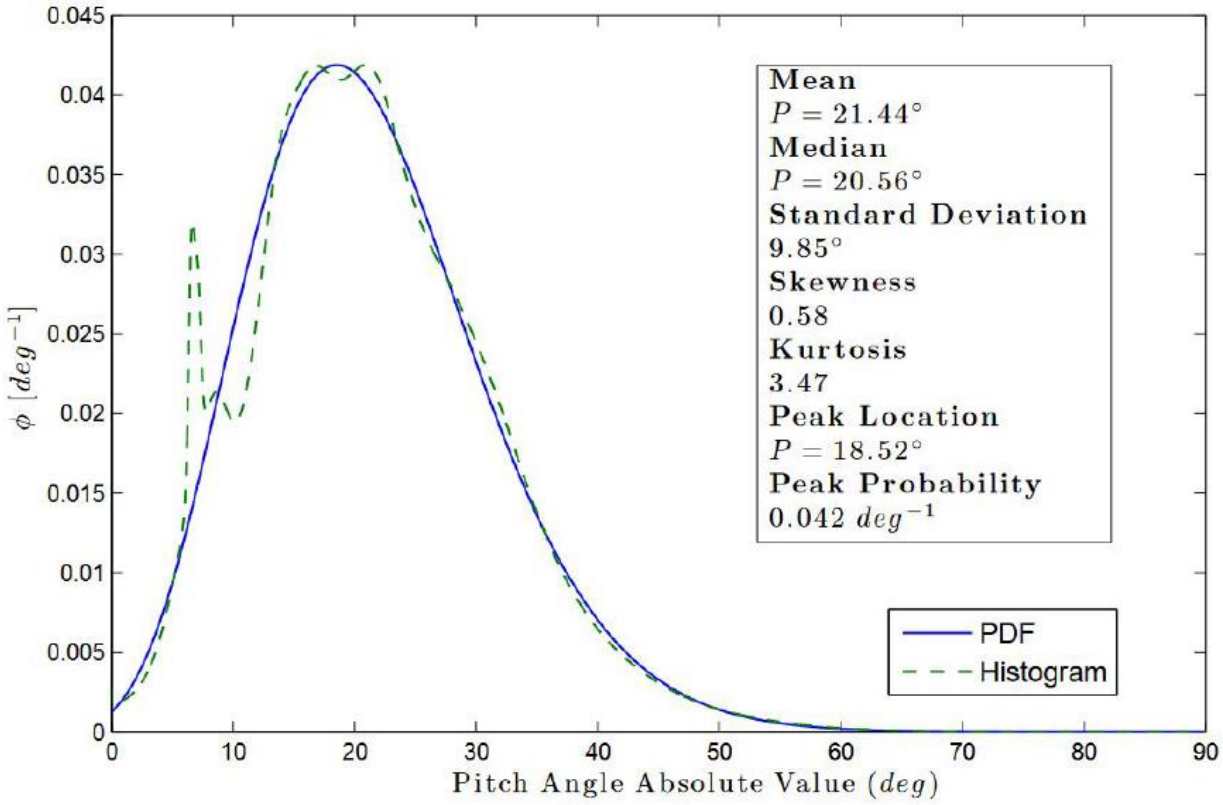

Figure 2.7a: Pitch angle distribution function from Davis et al. (2014).

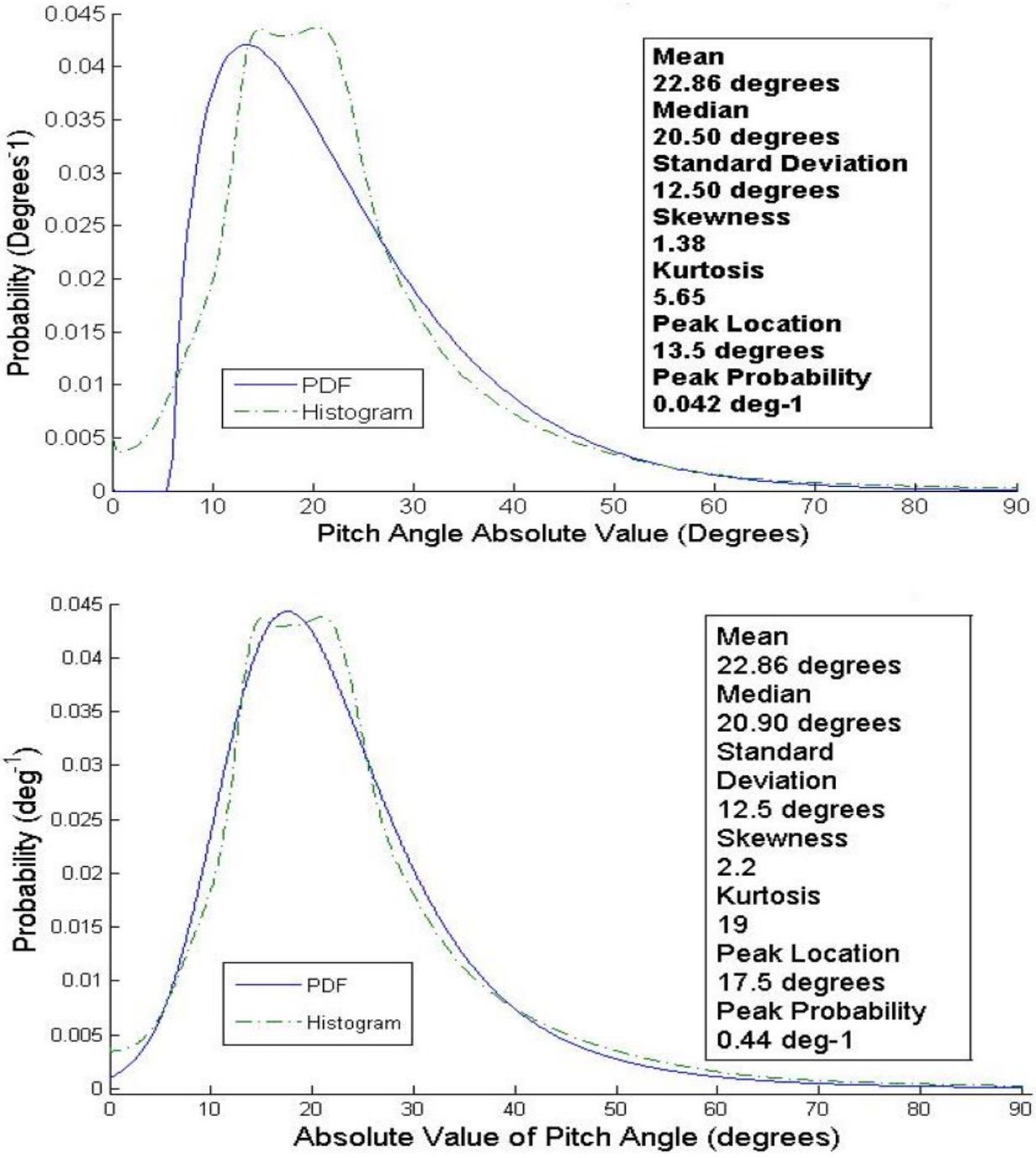

Figure 2.7b: PADFs for the faint galaxies sample. Solid lines are the Probability Density Function fits. Dotted lines are the distribution of P, modeled as a "binless" histogram, where each data point is a Gaussian with mean equal to pitch angle measured and standard deviation equal to associated measurement error. The traditional Probability Density Function fit does not match well to the data. A second attempt at best fitting a skew-kurtotic-normal distribution to the data is shown at the bottom. The faint galaxies sample shows higher skewness and kurtosis than its higher luminosity counterpart, indicating data points with larger associated errors and a heavier tail to the distribution. Graphs generated using Becker (2010).

The excess density at the peak may be related to the excess of m=2 spirals in the faint sample. Galaxies with two-arm symmetry tend toward successful pitch angle measurement as compared to flocculent galaxies or galaxies with higher-order arm symmetry. The two-symmetry galaxies are often more grand design-like, with higher arm-interarm contrast whereas galaxies assigned m=4 or m=6 symmetry have a tendency toward clumpiness, with an agglomeration of many arm segments and spurs rather than sharply defined, contiguous arms. Difficulties associated with the measurement of flocculent galaxies in the sample may bias the measurement toward the peak of the distribution.

Another possible cause of the excess at peak for the faint sample is the measurement success rate by Hubble type, paired with the Hubble type abundance in the sample. As compared to the Davis et al. (2014) sample, ours has fewer a-bc Hubble types and an excess of c-m types. The c-m types more commonly evade pitch angle measurement. Also, the peak excess might be the result of the relative lack of a and ab Hubble types in the faint sample. The absence of these higher mass spiral galaxies from the distribution would naturally raise the probability densities estimated for all other masses. The combination of a and ab types largely missing from the sample and cd and d types more commonly evading pitch angle measurement might account for the lower probability densities on either side of the peak of the pitch angle distribution function (PADF) and a corresponding relative amplification of the peak. When combined with the other previously mentioned causes, it is not all that surprising that the fainter galaxy sample would show a higher peak probability than its brighter counterpart. Finally, The Fundamental Plane, as reported in Davis et al. (2015), would support the idea of smaller bulges of these later type

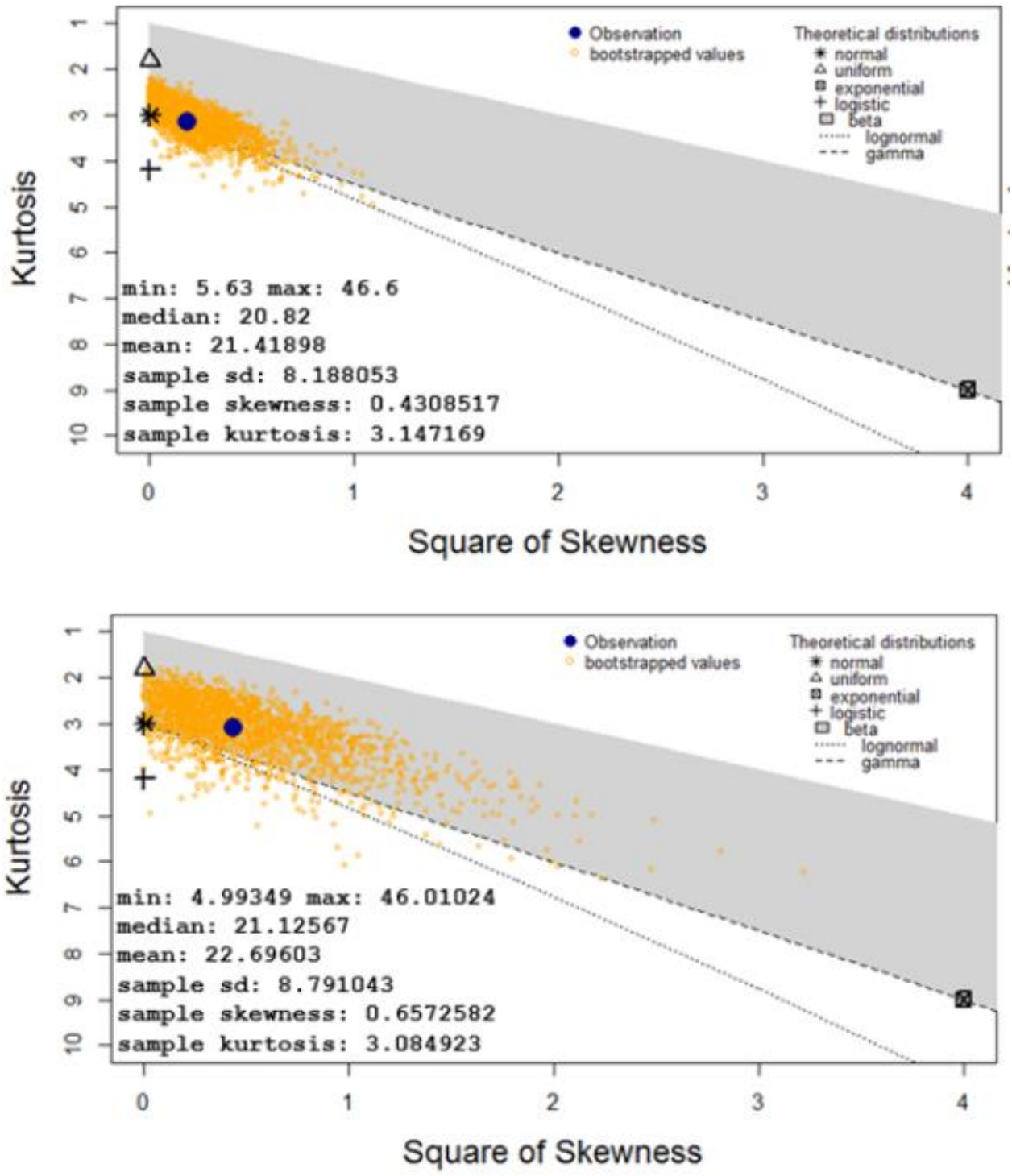

Figure 2.8: Comparison of Cullen and Frey graphs with a 2000 sample bootstrap for the Pearson Distributions of the Davis et al. (2014) sample (top) and faint galaxies sample (bottom). Despite the Pearson Distribution for the faint sample not fitting well to its data (i.e., not enough skewness or kurtosis), it is centered farther from the normal distribution on the Cullen and Frey graphs, illustrating this difference between the two samples.

galaxies being compatible with tighter pitch angles if they had low gas densities in their disks. This is a prospective subject for further study.

Cullen and Frey graphs are used to compare functions in skewness-kurtosis space. They are produced for each sample (Delignette-Muller & Dutang 2015) to further scrutinize distribution shape in the context of these parametric solutions (see Figure 8). Possible values of the skewness and kurtosis are calculated by bootstrapping (here, boot=2000) to illustrate the likely functional form of the parent distribution. The outcome is the bright sample more closely resembling a normal distribution than the faint galaxies sample. The excess skewness and kurtosis of the faint sample as interpreted in this way are somewhat reduced. The statistical fit of these values to the data did not match well to the binless histogram, and scatter in bootstrapped values for the faint sample is much larger. Accordingly, differences retained between the samples at the tail of the distribution are not ruled out. Consequently, we perform non-parametric fitting of the samples to further compare their tail behavior.

2.4 Pitch Angle Distribution

In order to assess whether the BHMF for the faint sample's lower luminosity regime of galaxies resembles those in preceding studies of brighter galaxies, an effective tool is to examine the Pitch Angle Distribution Function (PADF) of these galaxies in comparison to prior work. If the current set of galaxies comprise the same population as their brighter counterparts, their PADFs will mirror one another, whereas if the current sample encompasses a second population of galaxies (presumably at the low mass end of the distribution) this would alter the shape of the BHMF in this regime.

2.4.1 Non-Parametric Fitting

While parametric solutions to distribution fitting are simpler to express in functional forms, with insufficient data they are sometimes overly constrained. It is clear the initial Pearson fit to the faint sample was poor, likely due to the low number of galaxies in the sample. In such a low N case, a non-parametric Kernel Density Estimator (KDE) approach is more appropriate for PDF production and dataset comparison (see Figure 2.9). The distribution of the Davis et al. (2014) sample is closer to Gaussian, due to both morphology trends and to the larger sample size of the Davis distribution. For fuller assessment, KDE is chosen to fit both datasets.

Even though the two samples are morphologically distinct, their pitch angle distributions are appreciably similar. A possible tendency towards very loose spirals at our distribution's tail betrays a sign of the shift to higher P one may presume in a sample dominated by c and d Hubble types. This bump in the tail of the distribution is small, and measurement errors for 2DFFT are known to be larger in higher P regimes. As such, further analysis (below) is required to ascertain the strength of the tail. Kernal Density Estimator (KDE) fits of the two distributions are performed as a method of comparing the samples. As with the parametric (Pearson Distribution) fitting solutions, both samples have very similar peak pitch angles. The bright sample shows a broader and lower peak with excess probability slightly past peak but deficit probability far past peak in the high pitch angle regime. This naive gaussian KDE, however, does not fully take into account some of the behaviors of the data which might affect the probability distribution. Among these factors to correct for are bandwidth selection in performing the KDE and weighting for heteroscedasticity in the data. Confidence intervals around the best fit KDE are also requisite to attain a comparison of samples which best shows their compatibility.

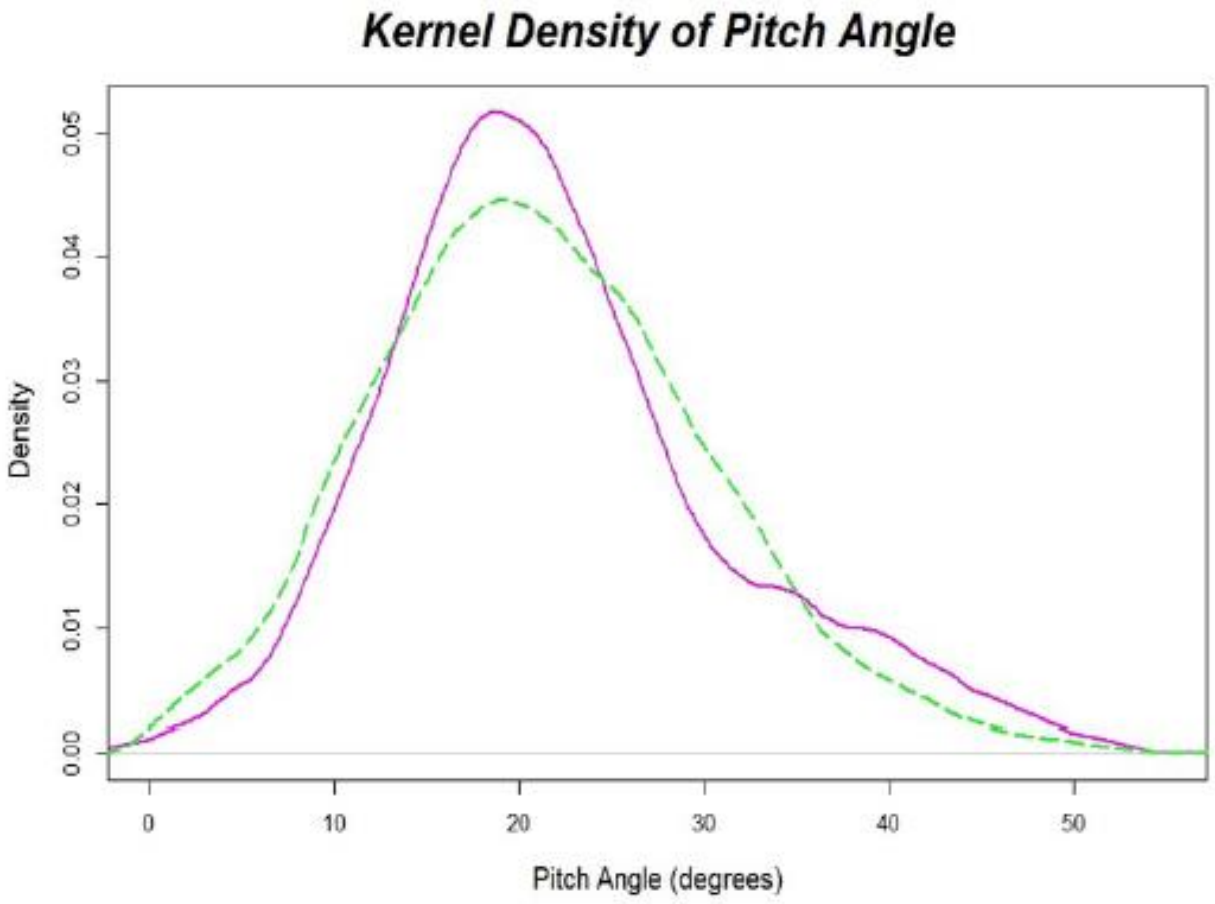

Figure 2.9: Comparison of Initial Kernel Density Estimator fits of the Probability Densities for the bright sample (green dashed) and faint galaxies sample (magenta solid). The faint galaxies sample has a slightly higher peak and heavier tail than its counterpart. Both distributions are strikingly similar at the lower pitch angle (higher mass) end of the function. The two functions reach peak probability density at nearly the same pitch angle. Graphs generated with Guidoum (2015).

2.4.2 Pitch Angle Dependent Errors and Bandwidth Optimization

2.4.2.1 Heteroscedasticity

Heteroscedasticity is an occurrence where the variance of a dataset changes for various subpopulations of the dataset. A common case of this is where the magnitude of the errors in one

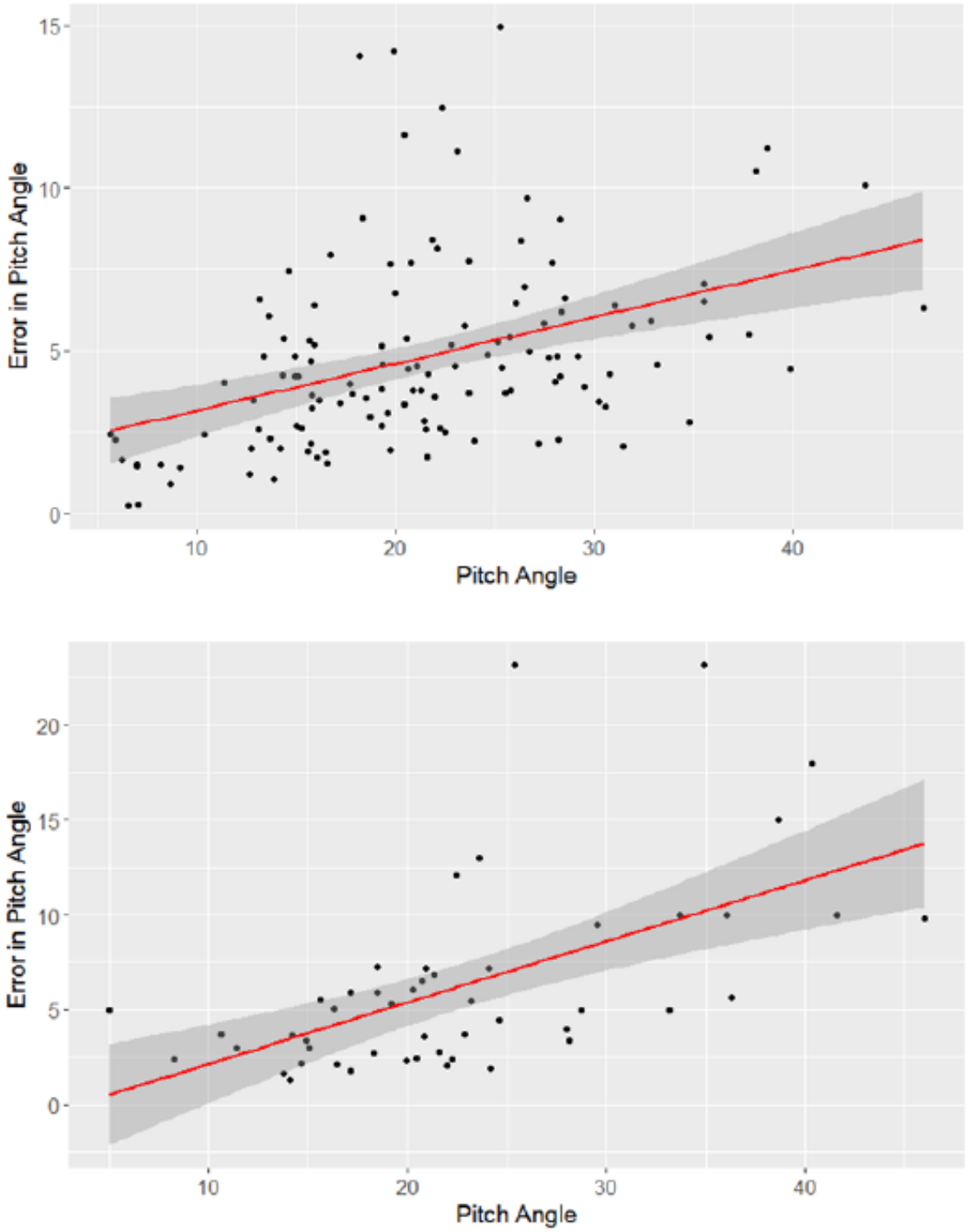

Figure 2.10: Measurements of Pitch Angle are heteroscedastic, for higher absolute values of pitch angle, the associated error in measurements is larger. Above: Error in P as a function of P for the Davis et al. (2014) sample. Below: Error in P as a function of P for the faint galaxies sample. Linear fits of heteroscedasticity are the red lines, 95% confidence intervals are shaded. Both data sets show increasing measurement errors as a function of pitch angle. Graphs generated using Fox and Weisberg (2011).

variable are covariant with the magnitude of another of the variables being examined. In order to properly KDE fit the PDFs of the two samples, heteroscedasticity of the datasets is assessed.

In the case of galactic pitch angle measurement, recorded errors are expected to grow with pitch angle. Spiral galaxies with small pitch angles (tightly wound) tend to be measured with more accuracy than those with large pitch angles (loosely wound). One reason for this error growth with pitch angle is largely the result of the measurement technique employed. Galaxies with tight spirals have a broader swath of phase angles (more rotations) of spiral arm to measure, while very loose spirals might not have even one measurable rotation.

It is shown in Figure 2.10 that both samples do have errors which grow as a function of pitch angle, in accordance with expectations. A linear model is fit to these errors. Robust Regression is applied in order to assign weights which minimize the impact of outliers to the fit. From this linear fit to the heteroscedasticity of the data, Huber weights are calculated which may be applied to each galaxy in distribution fitting. In this way, the excess error on the tail of the distribution is accounted for in the determination of the probability density.

2.4.2.2 Bandwidth Selection

Bandwidth selection is required to produce a more correct KDE. Maximum Likelihood Cross Validation (MLCV) assesses the optimal bandwidth for the data. Bandwidth in KDE may be thought of as a smoothing parameter of the fit when the number of observations is low. Higher bandwidths create functions with more smoothing while smaller bandwidths correspond to fits which are allowed more local variance. To avoid over or under smoothing the fit, we explore the effects of bandwidth selection on the behavior of the distribution. While peak height of the faint sample varies with bandwidth, the tail behavior of the distribution is largely

bandwidth independent (see Figure 2.11). This means we can trust the tail behavior of interest to be similar regardless of the bandwidth chosen, though the MLCV bandwidth is likely to be the most representative of the sample.

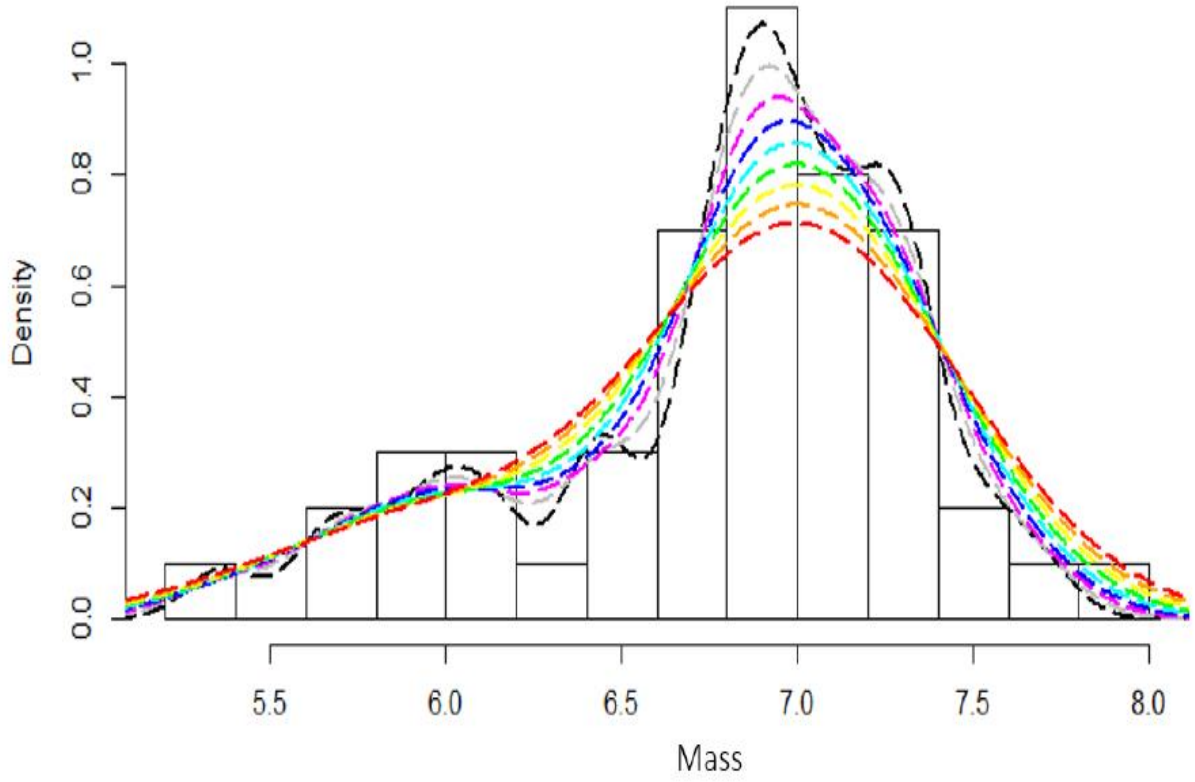

Figure 2.11: Bandwidth Comparison for Faint Sample. At higher bandwidths, the Faint Sample closer resembles the previous sample, while at lower bandwidths, some differences emerge. Bandwidth optimization techniques yield a bandwidth of 0.22 as optimal. Bandwidth selection does not strongly impact the height of the low mass tail of the distribution, and most strongly affects the density peak. Bandwidths: (0.1, 0.13, 0.16, 0.19, 0.22, 0.25, 0.28, 0.31, 0.34).

Using our MLCV-generated bandwidth with our Robust Weighted, Heteroscedasticity-corrected samples, we convert from Pitch Angle to Black Hole Mass using the M-P relation and produce a KDE of the BHMF for the two samples (see Figure 2.12). Errors are assessed using bootstrapping to find the 90% confidence interval around each density estimate. Another

alternate technique tested is Adaptive Bandwidth Kernel Density Estimation, wherein the shape of the kernel used to produce the density is allowed to change shape (broaden or tighten) based on local properties of the data. Adaptive bandwidth techniques are most applicable when estimating density for heavy tailed or multimodal distributions such as our faint galaxies sample. Confidence intervals are assessed around each sample using a 10000 sample bootstrap of the density estimation.

2.5 Black Hole Mass Function

The PADF is transformed to a BHMF using the M-P relation as described in Davis et al. (2014). Error propagation is performed before distribution fitting for the BHMF of each sample. Careful treatment of KDE produces updated estimates of the BHMF for these sets of spiral galaxies in the local universe. The distribution of masses for the faint galaxies sample largely mirrors that of Davis et al. (2014), with the anomalies mentioned earlier in the description of the PADF translated to mass space, namely, excess of density at the peak and somewhat for the tail for the faint sample, and under density of the faint sample at black hole masses higher than the mass of peak probability.

2.5.1 Pitch Angle Clustering

In order to further understand the behavior of the faint sample, various clustering techniques are employed. As the tail of the distribution of faint sample galaxies is heavy, and there is some indication of population differences between the Faint Sample and its brighter counterpart despite similar peak behavior, it is useful to explore whether the tail of the faint

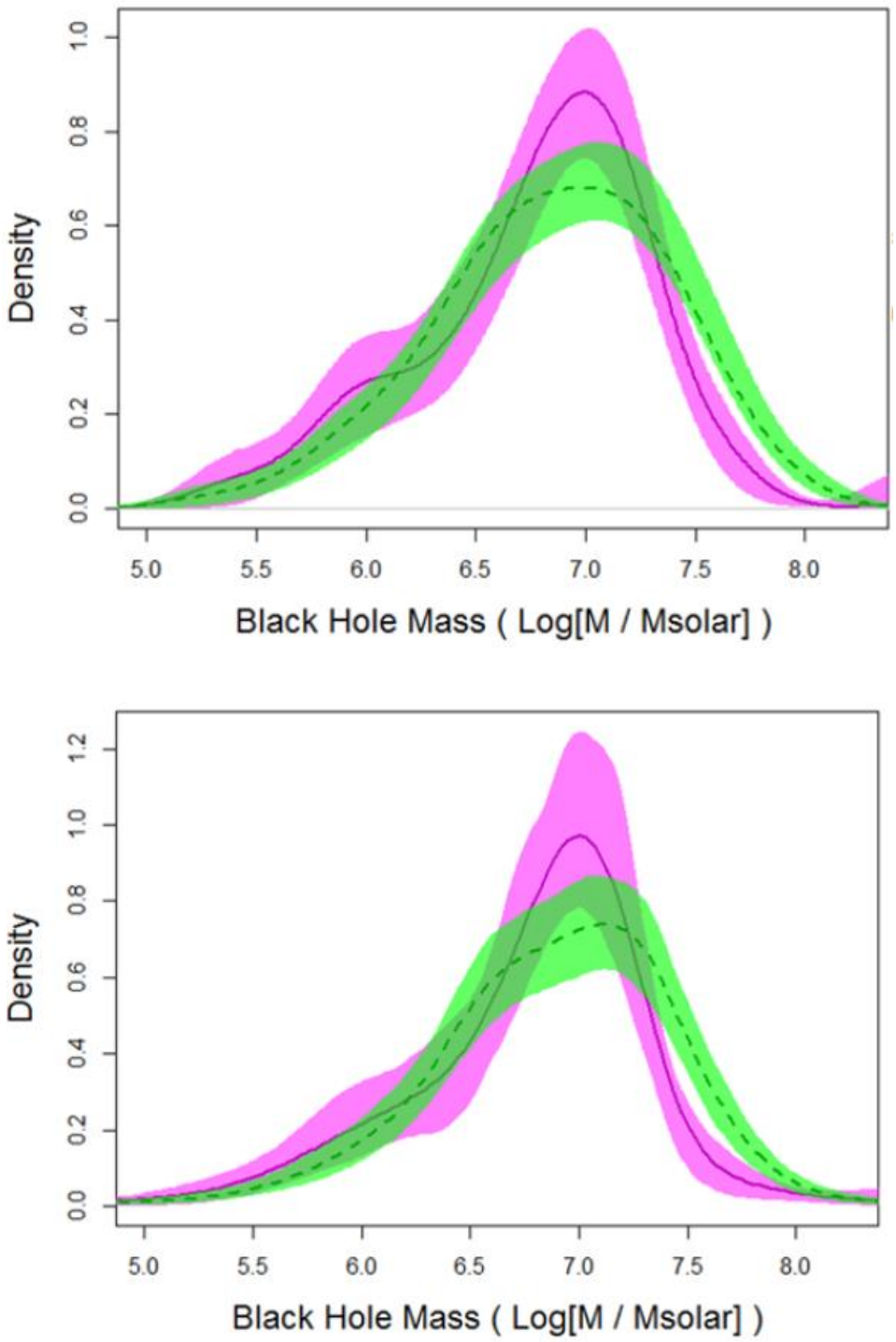

Figure 2.12: Top: Faint sample (magenta, solid line) and Davis et al. (2014) sample (green, dotted line) BHMF's as fit with Bandwidth Selected Kernel Density Estimator (bandwidth=0.22) and robust weighting. Bottom: Adaptive Bandwidth Kernel Density Estimator BHMF's. 90% confidence interval found using a 10,000 sample bootstrap is shown for each estimate. The faint sample shows a slight excess at the low mass tail of the distribution while the Davis et al. (2014) sample shows an excess at the high mass end which is likely due to more a and ab type galaxies in their sample.

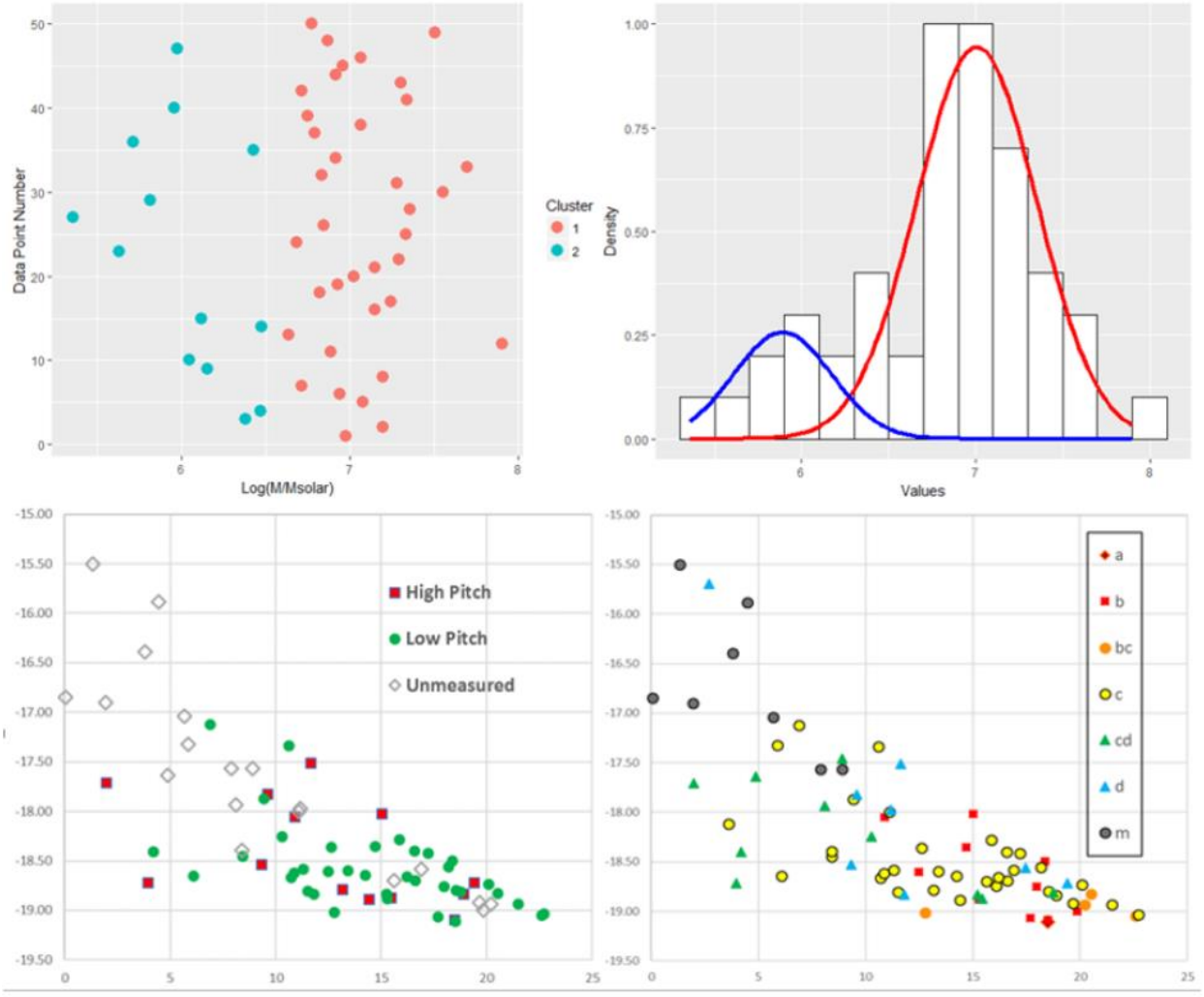

Figure 2.13: Top-left: Clustering of the faint sample into two clusters in black hole mass. Top-right: Histogram overlaid with distribution fits for each cluster. Graphs generated using Wickham (2009). Bottom-left: Faint sample galaxies plotted by cluster. Low pitch / high mass (green circles), high pitch / low mass (red squares), and unmeasured pitch angles (gray diamonds). Bottom-right: Faint sample by Hubble type. Note: m dwarf Hubble types comprise nearly all the galaxies fainter than M_B=-17. All of these galaxies went unmeasured in pitch angle.

sample represents a second population. We perform E-M clustering analysis of the pitch angle distribution to divide the faint sample into a High Pitch and Low Pitch subsample. Simple normality tests are not conclusive as to whether there is a true second population within the sample. However, examining the coincidence of population sorting with Hubble type reveals the

high pitch galaxies to consist of c, cd, and d hubble types. Not all of the c, cd, and d types were sorted into the high pitch cluster but none of the a-bc types were assigned to the high pitch cluster. From this examination it is shown some fraction of the very late Hubble types compose the second population. If the distribution is to be treated as one function rather than two, the single population carries a heavy tail made up of these latest hubble types.

To further flesh out this relationship, we fit the KDE probability densities of the sample by hubble type. We find the cd and d type galaxies to indeed peak at a higher pitch angle (lower SMBH mass). If the measured galaxies in the faint sample are divided by hubble type, c types make up half the sample at 25 measured galaxies, with a, ab, b, bc together making up about a quarter (all but one measured being b, bc) and cd, d, m making up the final quarter (no m galaxies were measured). When a, ab, b, bc, c are grouped together and cd, d, m are grouped together we find the tighter pitch angle, high mass group is well behaved with a very weak tail, but the cd, d group has a broad peak shifted to higher pitch angles (max P=23.24 degrees, mean P=28.69 degrees). This is not unexpected, as Hubble types are defined in part by the tightness of spiral arm winding. Hubble type letters past c should indeed correspond to loose spirals.

Using the two clustering populations, we produce a possible two-population model for the probability density which matches closely with the global population. The faint Sample population may be described with the superposition of two near-normal distributions or as one population with a heavy tail. In either case, the behavior at the extreme high P / low M end of the distribution is explained by the cd and d type galaxies in the sample.

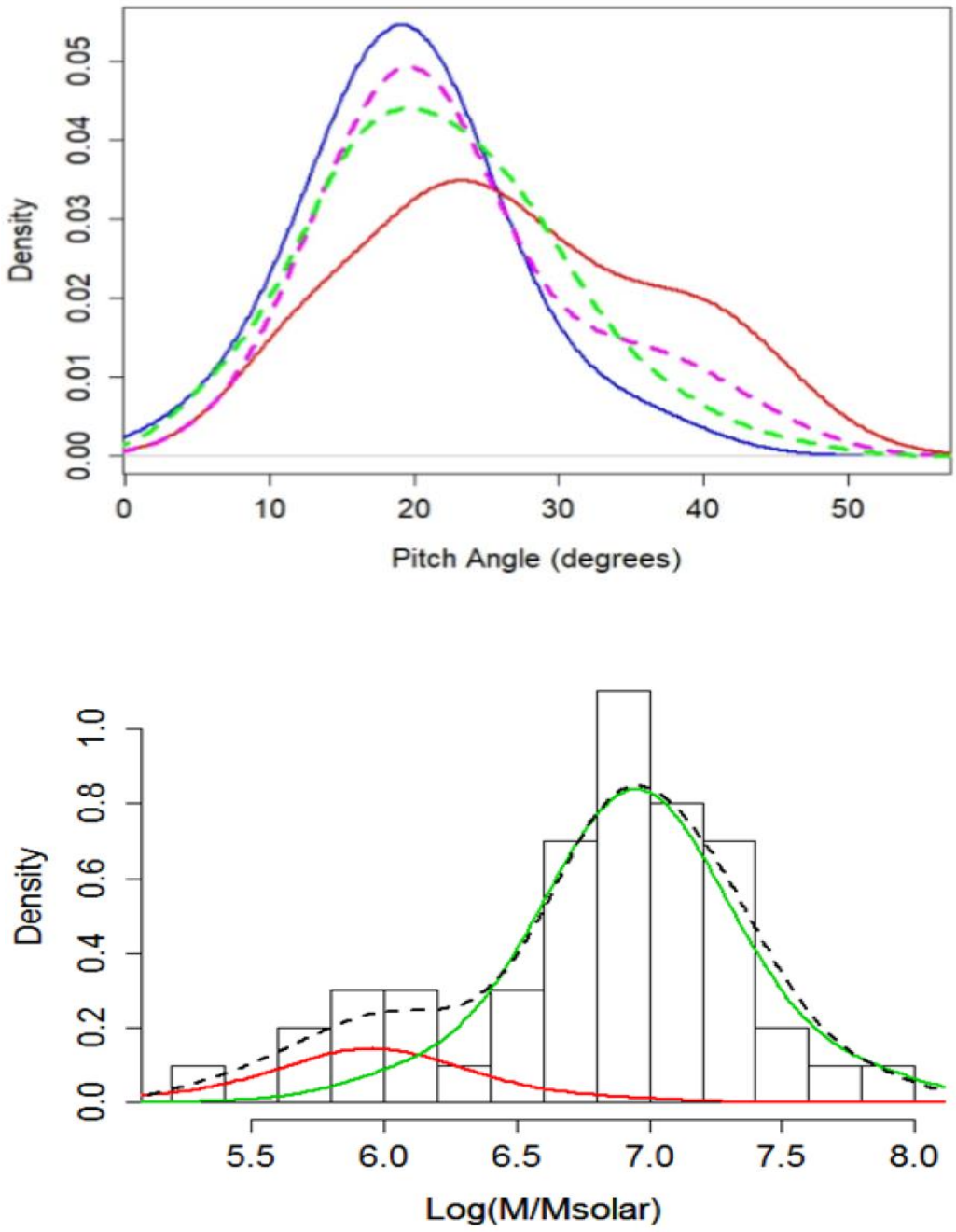

Figure 2.14: **Top:** Corrected PADFs of key subsamples. Green: bright limited Sample. Magenta: Faint Sample. Blue: Faint subsample of Hubble types a-c. Red: Faint subsample of Hubble types cd, d. From this figure it is clear that while the cd, d type galaxies make up a small fraction of the faint sample, they are the cause of most of the behavior at the tail of the distribution. It is also apparent that the excess peak height in the faint sample is a result of the comparative overabundance of Hubble Type c galaxies, which cluster strongly around the peak.

Bottom: BHMF of the faint sample decomposed into a low-mass and high mass-population. Curves are semiparametric fits to the cluster data. Dotted line is KDE of original distribution.

2.5.2 Combined BHMF for Local Spiral Galaxies Accounting for Sample Completeness

In order to construct the BHMF of local spiral galaxies we combine the bright sample from earlier work with the faint sample to eliminate the M_B constraint on the mass function. To do this properly, galaxies missing from the faint sample due to detection limits must be accounted for. This is accomplished by reweighting the galaxies from both samples based on the effective comoving volume of galaxies by M_B. The fainter the galaxies targeted, the smaller effective comoving volume in which such a galaxy could be detected. Our corrected Luminosity Function uses a Pearson Distribution fit of the number of galaxies by magnitude with the effective comoving volume to up-correct the number of galaxies at very faint magnitudes. We check the Pearson Distribution Fit against a KDE and find a reasonable match to the data, providing confidence in the computed Luminosity Function. With this new weighting based on effective comoving volume it is possible to properly combine the complete sample and adjusted incomplete sample into one population which describes the Black Hole Mass Function in the local universe. The BHMF is calculated in the same manner as with each individual sample, but with a reweighting of the combined input data to attempt to account for missing galaxies. The result of this combination retains some of the properties of each of the samples from which it originated, as it is effectively a weighted average of the two distributions. As such, the peak location remains largely unchanged. There is some retention of a heavier tail to the distribution at high P / low SMBH mass. This BHMF describes the distributions of non-dwarf spiral galaxies in the local universe.

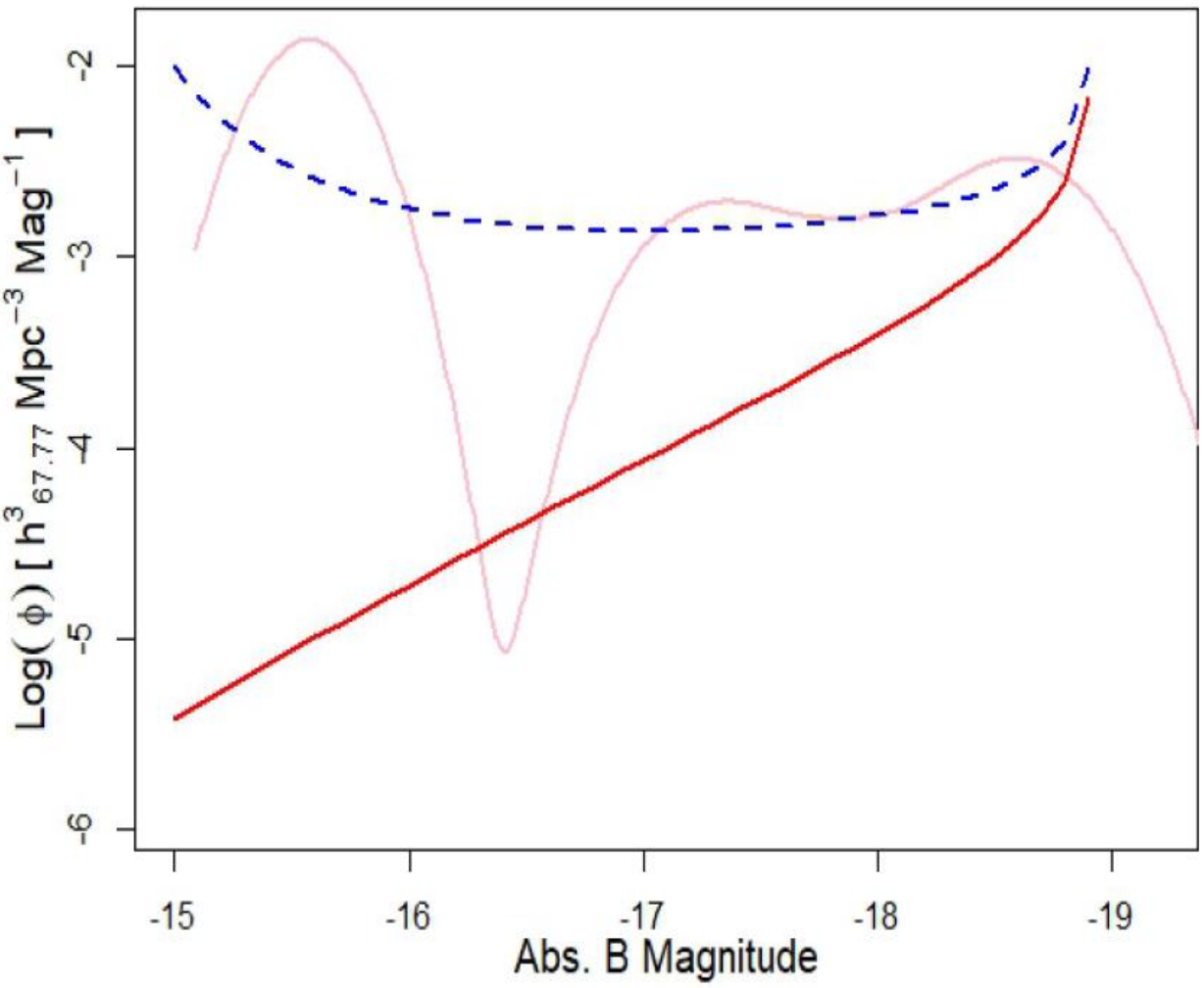

Figure 2.15: Luminosity Functions for CGS Faint Galaxies. Red: Uncorrected Luminosity Function of the Sample. Blue: Luminosity Function Fit as corrected for effective comoving volume of the galaxies in the sample. Pink: KDE check of the corrected Luminosity Function, showing the probability density based on actual galaxies. The number of measured galaxies at fainter than $M_B = 17$ was very small, accounting for the spikes below and above the functional fit correction. The corrected Luminosity Function produces reasonable galaxy abundances for the corrected sample. Galaxies in this regime are reweighted for density calculations with this correction to produce the BHMF for all measurable local spiral galaxies.

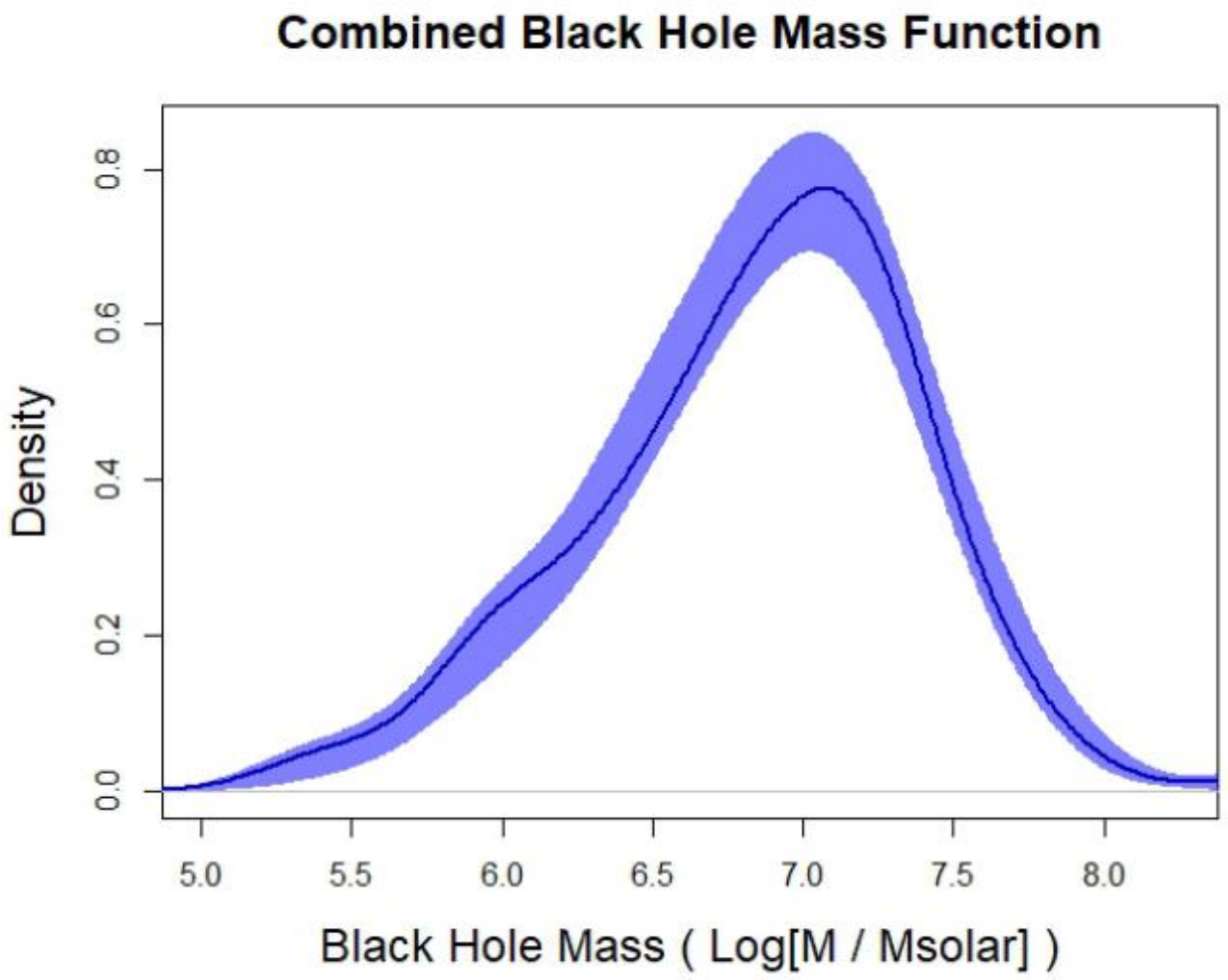

Figure 2.16: Combined Black Hole Mass Function with 90% confidence intervals for CGS galaxies with limiting luminosity distance of 25.4 Mpc. This Mass Function is representative of all spiral galaxies of Hubble Types a-d (m type spiral dwarf galaxies were not measured with any accuracy).

2.6 Discussion

The PADF and BHMF established from our latest sample of local disk galaxies resembles Davis et al. (2014). These subsets are mirrored at low pitch angles / high masses. However, they may diverge at the high pitch angle end of the dataset. The faint sample has a higher probability of large pitch angles (loose spirals) and a reduced probability of containing

small pitch angles (tight spirals). The difference between the two samples as denoted by our KDE approach is small, and the errors and biases in the pitch angle measurement process are not yet well enough defined to make an assertive distinction (see Figure 14). However, the morphological differences between the galaxies on the heavy tail of the distribution and those at the peak do suggest two separate populations.

The CGS sample contains a difference in Hubble type across abs. B mag. space, which illustrates the major difference between the two samples in question. The faint sample is largely missing its a and ab types and as a result has an excess of all other types. The Davis et al. (2014) sample, meanwhile, is missing the m types and perhaps some cd and d types as well, given the luminosity limit. The excesses and scarcities of the samples are borne out in density estimation of their PADFs and BHMFs. In comparison to the Davis et al. (2014) sample, the faint sample expresses scarcity at low P (high M) and overabundance at the distribution peak, with hints of slight overabundance at the distribution tail. The tail of the faint sample is heavy, suggesting the possibility of a multimodal distribution. We show that the cd and d galaxies cluster apart from the a and ab types in M_B, and largely comprise the "high pitch angle" subgroup found by two group clustering. Removal of this subgroup and replacement with typical a and ab galaxies from the faint sample would likely cause the faint sample and the Davis et al. (2014) sample to have convergent BHMFs.

As a whole, the resulting BHMFs of our sample and Davis et al. (2014) may be construed to be nearly identical once differences in population subgroups are accounted for. The weight of the low-mass tail of the BHMF remains somewhat unknown. Due to missing faint galaxies and poor pitch angle measurement rates in this regime, we are likely to be underestimating the density of the BHMF at its tail. The pitch angle measurement success rate for a-c types was

better than the cd, d, m tpye galaxies. Since the distribution for cd, d types peaks at higher pitch angles, it follows the tail of the distribution may be heavier than we measure. The extreme low-mass end (m types and other dwarfs) remains unmeasured to date. By correcting our sample for effective comoving volume, we attempt to recover a more representative distribution of galaxy pitch angles by accounting for galaxies missed due to their low surface brightness. In so doing, a combined sample is produced containing all galaxies within the CGS whose pitch angles were measured and whose limiting luminosity-distance was 25.4 Mpc. This combined sample is representative of the Local BHMF of spiral galaxies (excluding Magellanic spirals) in the local universe.

The lowest mass end of the spiral galaxy portion of the population is a strong candidate set for further study toward characterizing Intermediate Mass Black Holes (IMBH). Graham et al. (2019) examine a sample of 74 IMBH candidates in Virgo Cluster galaxies with three different black hole mass scaling relations and find 33 galaxies predicted to have masses less than 10^5-10^6 M_{solar} range, with many in the 10^4-10^5 M_{solar} range. Late type spirals with very loose (high pitch angle) arms represent a good candidate set for further IMBH study. Spiral galaxies with Pitch Angles greater than 27 degrees correspond to masses 10^5 M_{solar} and likely fall into the IMBH range (Graham et al. 2019). However, errors in pitch angle measurement at this pitch angle regime tend toward 5-10 degrees in pitch, which corresponds to more than an order of magnitude in mass. Precise mass estimates for these galaxies are challenging without the application in tandem of other black hole mass scaling relations for late type galaxies. Dwarf galaxies are also promising candidates for IMBHs, although those dwarfs without clear spiral structure must rely solely on other mass scaling relations for measurement. Filling the gaps in knowledge surrounding this low mass regime continues to be a desirable result.

2.7 Conclusions

The latest sample of CGS spiral galaxies have a pitch angle distribution function (and corresponding SMBH BHMF) analogous to that of Davis et al. (2014). There is strong indication of high-mass black holes missing from the faint sample, and some indication of an excess of lower mass black holes on the distribution tail. It may be claimed although populational differences exist between the two samples, the BHMF of spiral galaxies in the local Universe is not strongly altered at its low-mass end by the inclusion of galaxies with cd and d Hubble types. Excesses at the tail of the BHMF may be larger than recorded in our data, due to galaxies too faint to be observed and unmeasurable pitch angles for latest Hubble types. Davis et al. (2017) claim that galaxies with pitch angles greater than ~26.7° are candidates for hosting Intermediate Mass Black Holes (masses $<10^5$ M_{Solar}). It may be the case that the heavy tail of our pitch angle distribution is composed in part of galaxies hosting these objects.

Sellwood and Carlberg (2019) provide evidence of self-excited instabilities as the cause of spiral patterns in simulations of unperturbed disks. They find that although individual spiral modes are transient, fresh instabilities are excited as the old modes fade away, resulting in a recurrent instability cycle. If spirals are primarily driven by density waves, the newly birthed modes should have the same pitch angle as their dying parents. This has been shown to be the case in some simulations (Berlanga, 2010)**.** If this is the case, pitch angle measurement as a method for probing other galaxy characteristics is likely to be robust for a given galaxy across time, perhaps with the exception of transitional periods between dominant modes.

There exists a planar relationship among the quantities of central bulge mass, pitch angle, and galactic neutral hydrogen gas density (Davis et al. 2017). It has also been shown that higher disk masses favor lower multiplicity spiral patterns (Berrier & Sellwood, 2015; Sellwood &

Carlberg, 1984; Athanassoula et al. 1987). Galaxies with lower disk densities should, then, have a tendency toward higher number of arms and less m=2 grand design spirals. These lower disk density galaxies could produce spirals with similar pitch angles to their heavy disk counterparts if their bulges are less massive. Going forward, A census of neutral hydrogen gas density in galaxies targeted for pitch angle measurement should be taken, such that the populational differences among these parameters may be better explored. This is especially relevant for galaxies without grand design spiral structure, as their disks are likely to be less massive. In order to accurately produce the BHMF for late type galaxies, this alteration of pitch angle due to different gas densities should be taken into account.

The performance of pitch angle measurement techniques as a function of galaxy morphology, luminosity, and redshift, is yet to be surveyed. Studies in these areas, as well as in selection effects and biases, should reduce measurement errors and improve measurement success rates for future work. For now, we largely reaffirm the BHMF for local spiral galaxies of Davis et al. (2014), with the possibility of another population of lower mass black holes at the very late Hubble type, high pitch angle tail of the distribution.

2.8 Bibliography:

Athanassoula, E., Bosma, A., & Papaioannou, S. 1987, A&A, 179, 23

Bae, J., Nelson, R. P., & Hartmann, L. 2016, ApJ, 833, 126

Becker, M. 2010, PearsonDS: Pearson Distribution System, r package version 0.92. http://CRAN.R-project.org/package=PearsonDS

Berlanga Medina, J., "Dark Matter Halo Concentration and the Evolution of Spiral Structure in N-Body, Barred Spiral Galaxies" (2015). *Theses and Dissertations*. 1439. https://scholarworks.uark.edu/etd/1439

Cuzzi, J. N., Lissauer, J. J., & Shu, F. H. 1981, Nature, 292, 703

Dalla Bont_a, E., Ferrarese, L., Corsini, E. M., et al. 2009, ApJ, 690, 537

Davis, B. L., Berrier, J. C., Shields, D. W., et al. 2012, ApJS, 199, 33 |. 2016, 2DFFT: Measuring Galactic Spiral Arm Pitch Angle, Astrophysics Source Code Library,ascl:1608.015

Davis, B. L., Graham, A. W., & Seigar, M. S. 2017, MNRAS, 471, 2187

Davis, B. L., Berrier, J. C., Johns, L., et al. 2014, ApJ, 789, 124

Davis, B. L., Kenne_ck, D., Kenne_ck, J., et al. 2015, ApJL, 802, L13

Delignette-Muller, M. L., & Dutang, C. 2015, Journal of Statistical Software, 64, 1. http://www.jstatsoft.org/v64/i04/

Elmegreen, B. G., Elmegreen, D. M., & Montenegro, L. 1992, ApJS, 79, 37

Ferrarese, L., & Merritt, D. 2000, ApJL, 539, L9

Fox, J., & Weisberg, S. 2011, An R Companion to Applied Regression, 2nd edn. (Thousand Oaks CA: Sage). http://socserv.socsci.mcmaster.ca/jfox/Books/Companion

Franceschini, A., Vercellone, S., & Fabian, A. C. 1998, MNRAS, 297, 817

Gebhardt, K., Bender, R., Bower, G., et al. 2000, ApJL, 539, L13

Graham, A. W., Driver, S. P., Allen, P. D., & Liske, J. 2007, MNRAS, 378, 198

Graham, A. W., Scott, N., & Schombert, J. M. 2015, Publication of Korean Astronomical Society, 30, 335

Graham, A. W., Soria, R., & Davis, B. L. 2019, MNRAS, 484, 814

Guidoum, A. 2015, kedd: Kernel estimator and bandwidth selection for density and its derivatives., r package version 1.0.3. http://CRAN.R-project.org/package=kedd

Ho, L. C., Li, Z.-Y., Barth, A. J., Seigar, M. S., & Peng, C. Y. 2011, The Astrophysical Journal Supplement Series, 197, 21

Lin, C. C., & Shu, F. H. 1964, ApJ, 140, 646

Marconi, A., Risaliti, G., Gilli, R., et al. 2004, MNRAS, 351, 169

Natarajan, P. 2011, ArXiv e-prints, arXiv:1105.4902

Peng, C. Y., Ho, L. C., Impey, C. D., & Rix, H.-W. 2010, AJ, 139, 2097

P_erez, L. M., Carpenter, J. M., Andrews, S. M., et al. 2016, Science, 353, 1519

Puerari, I., Block, D. L., Elmegreen, B. G., Frogel, J. A., & Eskridge, P. B. 2000, A&A, 359, 932

Richstone, D., Ajhar, E. A., Bender, R., et al. 1998, Nature, 395, A14

Richstone, D. O. 2002, Reviews in Modern Astronomy, 15, 57
Rodriguez, S., & Padilla, N. D. 2013, MNRAS, 434, 2153

Salucci, P., Szuszkiewicz, E., Monaco, P., & Danese, L. 1999, MNRAS, 307, 637

Savorgnan, G., Graham, A. W., Marconi, A., et al. 2013, MNRAS, 434, 387

Schlay, E. F., & Finkbeiner, D. P. 2011, ApJ, 737, 103

Schrodel, R., Ott, T., Genzel, R., et al. 2002, Nature, 419, 694

Seigar, M. S., Kenne_ck, D., Kenne_ck, J., & Lacy, C. H. S. 2008, ApJL, 678, L93

Sellwood, J. A., & Carlberg, R. G. 1984, ApJ, 282, 61—. 2019, arXiv e-prints,
arXiv:1906.04191

Sersic, J. L. 1963, Boletin de la Asociacion Argentina de Astronomia La Plata Argentina, 6, 41

Shankar, F. 2009, New Astronomy Reviews, 53, 57

Shankar, F., Salucci, P., Granato, G. L., De Zotti, G., & Danese, L. 2004, MNRAS, 354, 1020

Shu, F. H. 2016, ARA&A, 54, 667

Tully, R. B., & Fisher, J. R. 1977, A&A, 54, 661

Tundo, E., Bernardi, M., Hyde, J. B., Sheth, R. K., & Pizzella, A. 2007, ApJ, 663, 53

Vika, M., Driver, S. P., Graham, A. W., & Liske, J. 2009, MNRAS, 400, 1451

Wickham, H. 2009, ggplot2: Elegant Graphics for Data Analysis (Springer-Verlag New York).
http://ggplot2.org Xu, W., & Goodman, J. 2018, MNRAS, 480, 4327

3 UGC 4599: Revealing the Extended Structure of a Giant Low Surface Brightness Hoag's object analog with HERON

3.1 Abstract

The Halos and Environments of Nearby Galaxies (HERON) Survey employs a 0.7m telescope to explore low surface brightness structures in nearby galaxies. UGC 4599 was targeted for early imaging, as it is an early type galaxy with a UV excess, and deep images revealed a disk**.**

Prior photometric studies of UGC 4599 were focused on the bright core and star forming ring of the galaxy. However, the HERON Survey is capable of probing the fainter, extended halo. With an eight hour integration, we find a very faint extended disk with an extrapolated central surface brightness of I_o=26 r magnitudes per square arcsecond and a scale length of 18 kpc, with a distinct spiral arm surrounding the core and ring of UGC 4599. The spiral is detected to approximately 40kpc in radius and the disk continues to beyond 60 kpc. The main ring of the galaxy is broken with an m=2 (180 degree) symmetry, suggesting a two armed spiral structure. However, once the core and ring of UGC 4599 are modeled, a well defined single arm spiral emerges, extending from the central region to several times the radius of the ring. This spiral structure corresponds well with an m=1 spiral in the HI profile as seen in Very Large Array (VLA) radio column density mapping. The arm is also seen in Galex UV. Though the ring appears to break in two places and there are some indications of a weaker second arm, the spiral structure is comprised mainly of one dominant arm.

Using a stacked u band image from Lowell Observatory's 4.3-m Discovery Channel Telescope, we measure the star formation rate of UGC 4599 in its disk/arms, as well as in the galaxy as a whole. For the entire galaxy, we find an SFR of 0.143±0.013 M_{solar}.

In late-type galaxies, the pitch angle of spiral arms has been shown to correlate with the mass of the central Supermassive Black Hole (SMBH) in an M-P relation. The pitch angle of the one arm spiral of UGC 4599 is measured to be $6.49^{o}\pm1.49^{o}$. This corresponds to an SMBH mass of $6.98*10^{7}$ M_{Solar}.

The outermost edge of UGC 4599 as detected in our imaging is best modeled as an extension of this one armed spiral from the center of the galaxy. There are also some indications of a second, fainter spiral arm with the same pitch angle as its brighter counterpart.

3.2 Introduction

UGC 4599 is a nearby (26.9 Mpc) galaxy with an unusual ring morphology resembling that of Hoag's Object. Finkelman & Brosch (2011) identify it as the nearest target of its kind, and therefore a promising candidate for learning more about Hoag's type galaxies. Hoag's Object (Hoag 1950) is characterized by an elliptical-like yellow core surrounded by a blue star forming ring. Hoag's Object was also found to contain an extended HI ring outside the star forming ring (Brosch et al. 2013).

Ring galaxies may be formed through a variety of possible pathways. These include secular evolution through bar-related resonances (Buta and Combes 1996), collisions/major-mergers of two or more galaxies (Lynds & Toomre 1976; Appleton & Struck-Marcell 1996), and gas rich accretion or minor mergers (Buta & Combes 1996; Reshetnikov & Sotnikova 1997). Yet another possibility is that of a polar ring galaxy, thought to generally be formed by orthogonal or at least aplanar galactic collisions (Schweizer et al. 1983). Roughly 0.5% of nearby S0 Hubble Type galaxies are shown to contain polar rings (Whitmore et al. 1990).

In their photometric study of UGC 4599, Finkelman & Brosch (2011) find UGC 4599 to be comprised of a red core conforming to a de Vaucouleurs surface brightness profile, a blue star forming ring which on closer inspection appears to contain some evidence of a spiral structure, and an extended HI disk. They also rule out bar evolution as a formation mechanism for this galaxy feature and instead propose a major interaction of two spiral galaxies as the history. It remains a possibility the extended HI structure was directly accreted from the Intergalactic Medium (IGM) rather than through a major merger.

As ground based telescopes develop in observing capabilities, both through the use of single small-aperture telescopes (Rich et al. 2017) and arrays (Abraham & Van Dokkum 2014), the identification and characterization of low surface brightness objects has become more common. Giant Low Surface Brightness Galaxies are very large, very faint galaxies up to 250 kpc in diameter (Boissier et al. 2016) which are characterized by massive dark matter halos (Das, 2013), high hydrogen gas surface densities (Bothum et al. 1987), and generally low metallicities. Their extended disks have extrapolated central surface brightness values less than the Freeman (1970) value for disk galaxies of μ_{oB}=21.65 mag/arcsec^2. These galaxies sometimes have a High Surface Brightness central component, which may be elliptical, spiral, or lenticular. They generally lack bars and have loosely wound spiral arms (Bothun et al 1997) but if there is a bulge dominated central component they may have tighter spiral arms (Das 2013). Giant Low Surface Brightness Galaxies also sometimes show ring structures, as in the case of UGC 6614 (Das 2013). Formation histories are not well understood but include catastrophic collisional models (Zhu et al 2018) and isolated secularly evolved models, either through dynamical evolution involving bars (Noguchi 2001) or through very slow star formation models in a low

surface density disk (Boissier et al. 2016). We identify UGC 4599 as a low surface brightness galaxy with an HSB component analogous to Hoag's Object.

We observe UGC 4599 as part of the Halos and Environments of Nearby Galaxies (HERON) Survey (Rich et al. 2017). Deep imaging of UGC 4599 is performed in the Luminance filter. Initial results revealed a faint extended structure to UGC 4599 in the optical extending to a few times the radius of the bright star forming ring. Due to the obscuration of a bright foreground star, this structure was initially thought to be a second, much fainter outer ring structure. However, upon further examination it is revealed to be a one armed spiral with a low pitch angle near 6 degrees. This one armed spiral matches in position to an m=1 spiral in the HI density map of the galaxy. There are some signs of an even fainter spiral arm in between the windings of the one arm, making a possible m=2 spiral with one dominant and one lesser arm. Some star formation in the one arm spiral is also detected in GALEX UV images of UGC 4599. As such, it appears the radial morphology of UGC 4599 is comprised of a central elliptical-like core region, bright star forming ring, and faint m=1 (possibly m=2) outer spiral embedded in a massive HI disk and coplanar with the inner ring structure.

3.3 Observations and Image Processing

New images of UGC 4599 were acquired using dedicated 28 inch (0.7m.) Centurion telescopes in California and Israel. The C28 has its detector at f/3.2 prime focus, resulting in images as good as 1.5 arcsec resolution. The California site is near Frazier Park, northwest of Los Angeles, and has an altitude of 1583 m. The zenith on moonless nights at the site is typically 21.65 mag/sq. arcsec, and very dark in the west (away from L.A.). The sister telescope is at the

Wise Observatory in Israel. For full description of the telescope and observing methods, see Brosch et al. (2015).

For imaging of UGC 4599 and other low surface brightness objects, we make use of the Luminance (l) band filter. This filter samples a wide bandpass of optical wavelengths with high transmission. With luminance filter images, we are able to reveal faint outer structures of galaxies and their companions with the use of a relatively small telescope. Imaging through the Luminance filter rather than some other standard band filter has the primary purpose of decreasing the integration time required for very deep imaging of local galaxies.

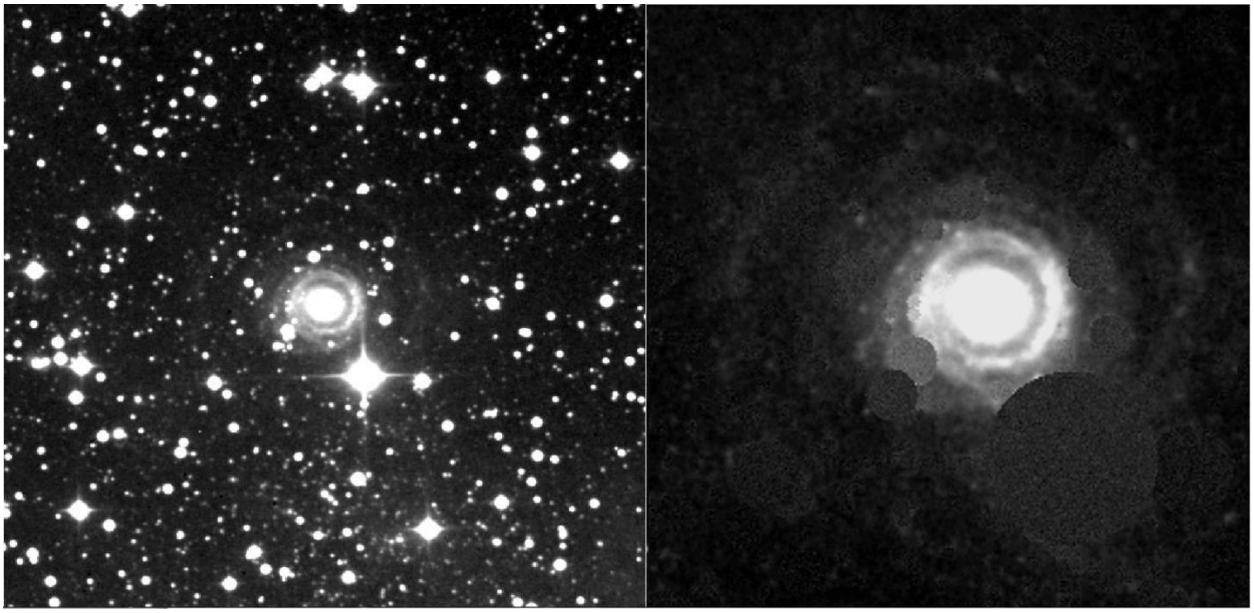

Figure 3.1 Left: Luminance filter image of UGC 4599, 8 hour integration time. Note the field is crowded with foreground stars. Right: Star masked and cropped version of the left image. Star removal by circular masks brings out underlying ring and spiral structure which extends to much larger galactic radii than noted in past studies.

By gathering photons from the entire visible spectrum, we are able to detect the equivalent of a Sloan Digital Sky Survey (SDSS) r filter surface brightness of approximately 30th magnitude per square arcsecond with an 8 hour integration. For collections of pixels

(surface brightness regions rather than single pixels), it is possible to extend detection of structure to marginally fainter than the 30 magnitude limit through averaging flux above sky values from grouped pixels. An initial disadvantage of the luminance band is the difficulty in converting to other optical bandpass magnitude equivalents. This requires an availability of stars of known magnitudes and colors in the field and some color information about the observed galaxy itself. Follow up or archival observations of the object in other bands are useful to this end. Luckily, spiral arms and the ring of UGC 4599 are relatively blue, and the color of the b-r ring of the system is well characterized in Brosch et al. (2013). As a result, we apply the color of the inner ring and assume the outer spiral is similarly colored.

Observations of UGC 4599 were also carried out on the night of November 29, 2016 with Lowell Observatory's 4.3-meter Discovery Channel Telescope (DCT), located forty miles southeast of Flagstaff, AZ. Images were obtained with the Large Monolithic Imager (LMI), which uses a single 6144 x 6160 e2v CCD. All images were binned 2 x 2, which yields a pixel scale of 0.24 arcsec. and a 12.3 x 12.3 arcminute field of view. Five individual exposures, each of 1200s duration, were obtained using the SDSS u filter, with dithering between exposures to remove the effects of bad pixels and to improve flat fielding. Seeing was poor, 1.7 arcsec, with some thin cirrus. Standard data reduction techniques were used to reduce and co-add the images. Archival GALEX UV and VLA HI column density radio images were also utilized.

3.3.1 Star Mask and Symmetrical Components

With the presence of several bright foreground stars, substantial image processing is required to detect the faint outer structures of UGC 4599. The use of star masks and/or star subtraction are included in this processing. By replacing the major foreground stars in the image

with circular masks at sky values, images of the structure of the galaxy may be produced with better scaling. Masking also improves modeling of the galaxy using various techniques.

Symmetrical component images involve taking pixels separated by a rotational symmetry (for m=2, 180 degrees apart, for m=3, 120 degrees apart, etc.) from the original image and replacing all pixel sets with the value of the lowest group member (Shields et al. 2015). If the galaxy contains symmetric structures such as spirals, this technique assists to remove asymmetric components such as foreground stars. This is often useful in preprocessing for the measurement of quantities such as the logarithmic spiral arm pitch angle. Foreground stars and asymmetric structures have a tendency to blow up the associated errors for most pitch angle measurement techniques, and sometimes result in a wrong recorded pitch angle if measurements fit through one or more bright stars instead of the actual galactic spiral.

It is clear the central star forming ring of UGC-4599 is broken in at least two places with an m=2 symmetry. Our confirmation of this feature reaffirms the observation of breaks in the ring noticed by Finkelman & Brosch (2011). The m=2 and m=4 symmetrical component images of the core of UGC 4599 both show at least somewhat symmetrical (with m=2 symmetry) breaks in the star forming ring of UGC 4599. These breaks are seen in both UV and optical images of the galaxy.

In addition to the breaks in the ring structure, we observe the presence of spiral structure extending well beyond the star forming ring. On first examination this appeared to be a second faint outer ring structure. The masked foreground stars had made it difficult to discern whether this structure was a complete ring or broken, and it did not appear centered on the core of the galaxy. Due to these characteristics, it was suspected the outer ring might actually be a spiral

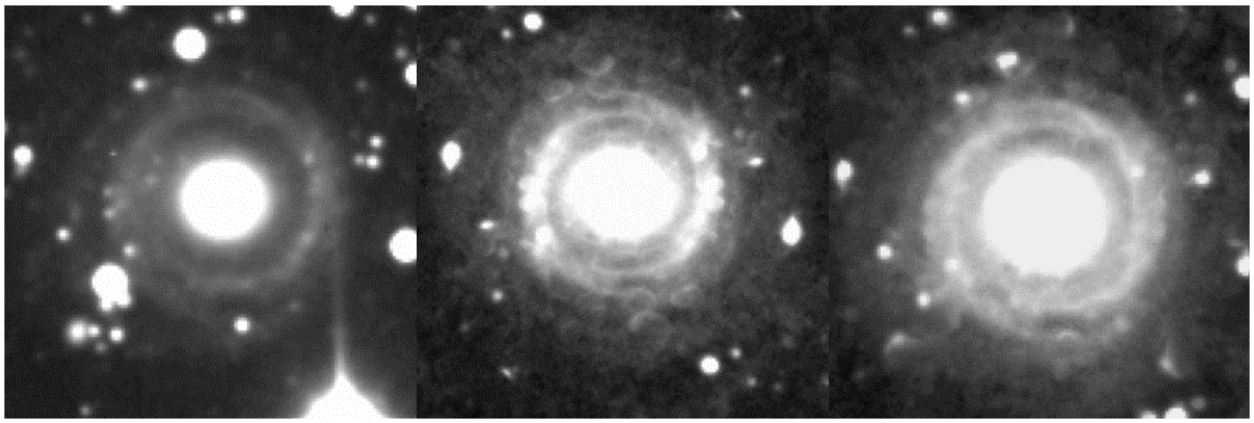

Figure 3.2 Original (left), m=2 (center), and m=4 (right) symmetrical component images of the central region of UGC 4599. In the original image, spiral structure breaking the ring is visible. This becomes even more apparent in the symmetrical components. Breaks at the rings top and bottom appear to form spiral arms.

structure with low pitch angle (close to circular) extending from the center of the galaxy but partially hidden by foreground stars. More rigorous star subtraction instead of masking revealed this to indeed be the case, with confirmation in Galex UV and VLA HI column density mapping, discussed later.

3.3.2 Star Subtraction

Star subtraction using the IRAF routine DAOPHOT allows the retention of more of the structure of the galaxy than masking techniques. Star subtraction in crowded fields is a relatively time consuming process, but worthwhile here as the circular masking technique mentioned earlier throws out a significant fraction of measurable galaxy data (parts of the galaxy/spiral hidden in the circular masks). However, even a relatively good parameterization of DAOPHOT falls short of completely removing the imprint of the stars from the image.

Imperfect subtraction is largely the result of issues relating to the Point Spread Function (PSF) generated for the image. An imperfectly created PSF leads to the removal of stellar profiles which either peak too shallowly or too sharply. After subtraction, the removal of an imperfect psf shape results in torus shaped regions of over/under subtraction at the location of the stars being removed. These over/under residuals from star subtraction may contain positive or negative counts with large values relative to the sky counts. These donut shaped star residuals interfere with producing aesthetic surface brightness maps of the galaxy, as well as interfering with pitch angle measurement. Mitigating the effects of these residual remnants of foreground stars is essential in creating a more accurate map of the surface brightness of the galaxy and in preparing for pitch angle measurement of the observed spiral structure of UGC 4599.

In addition to the problem of imperfect PSF creation, stars in the image which are saturated do not subtract well. Heavily saturated stars exhibit diffraction spikes which do not at all conform to a smooth PSF subtraction. Unfortunately, one very bright foreground star in the field of UGC 4599 completely obscures an interesting section of the galaxy which likely contains a large segment of the m=1 spiral structure. Galex and DCT UV images are useful for this section of the galaxy, as the foreground star is not as bright in the UV.

3.3.2.1 Sigma Clipping

One solution to the issue of minimizing star subtraction remnants is to remove both the undersubtracted and oversubtracted portions of the residuals through sigma clipping of the image. The simplest form of this technique would be to revise all pixels greater than some chosen sigma above the sky average with the sky value and all pixels lower than some other

chosen sigma below the sky average with the sky value. Unfortunately, this method of clipping dramatically limits the degree to which the bright portion of the remnants can be brought down and corrected toward the sky value. This technique is limited by the value of the brightest pixels in the core of UGC 4599. The center of the galaxy in the image is relatively bright and revising all pixels above this value to the sky mean leaves foreground star residuals in the outer sections of the galaxy much brighter than the surrounding galactic structure.

To solve the issue of basic sigma clipping leaving large residuals in the faint outer regions of the galaxy, of the galaxy, we performed iterative sigma clipping in selected regions, proceeding in steps from the outer regions of the image inward, with the upper bound on the brightness of pixels clipped being repeatedly revised so as not to erase any galaxy information while rejecting as many hot and cold pixels from imperfect star subtraction as possible. The threshold to select for a given image square is very clear as too low a sigma removes galaxy pixels and too high leaves bright foreground star remnants. In this way, the limit for the brightest unclipped pixel varies radially with the galaxy and is set to be as close to this brightest galaxy pixels as possible for a given radius.

Instead of clipping being limited by the brightest pixels at the center of the galaxy, this iterative version of clipping allows the residuals of star subtraction in the outer edges of the galaxy to be nearly as faint as the galactic structure itself. Since we are most interested in the faint spiral structure at the outermost regions of UGC 4599, the user input based iterative clipping method is by far the best practice.

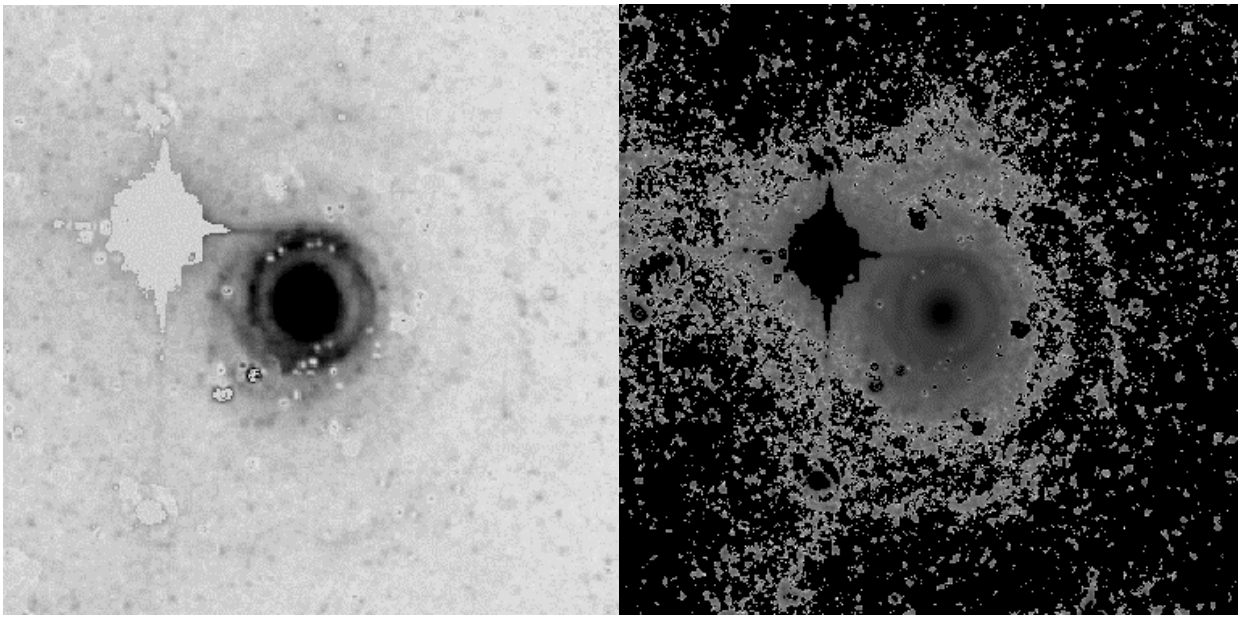

Figure 3.3 Left: Star subtracted and sigma clipped luminance image of UGC 4599 showing extended spiral structure. Star subtraction performed using the IRAF routine DAOPHOT. Sigma clipping to help remove extreme values (foreground stars and imperfect star subtraction) futher cleans up the image.

Right: Luminance image of UGC 4599, with values at or below sky values characterized as Not a Number and colored black. The image has been star subtracted with DAOPHOT and sigma clipped to remove extreme values. The one spiral arm is very clearly distinguishable from the sky background. A possible second arm is with m=2 symmetry to the first is very faintly visible.

3.4 Image Decomposition using GALFIT

The software GALFIT (Peng et al. 2002) is an algorithm which fits functions to point sources and galaxies in images. The program allows simulated galaxies to be built from scratch or model building to fit the parameters of existing galaxies from images. Originally designed for elliptical galaxy shapes, the newest version of GALFIT (Peng et al. 2010) now allows for fitting of more complex structures including spirals, boxy bulges, and tidal tails. Here we make use of GALFIT in two ways: a model fitting of the galaxy using various offset truncated ring stuctures, and a removal of a core plus ring profile in order to amplify the visible spiral structure in the residuals.

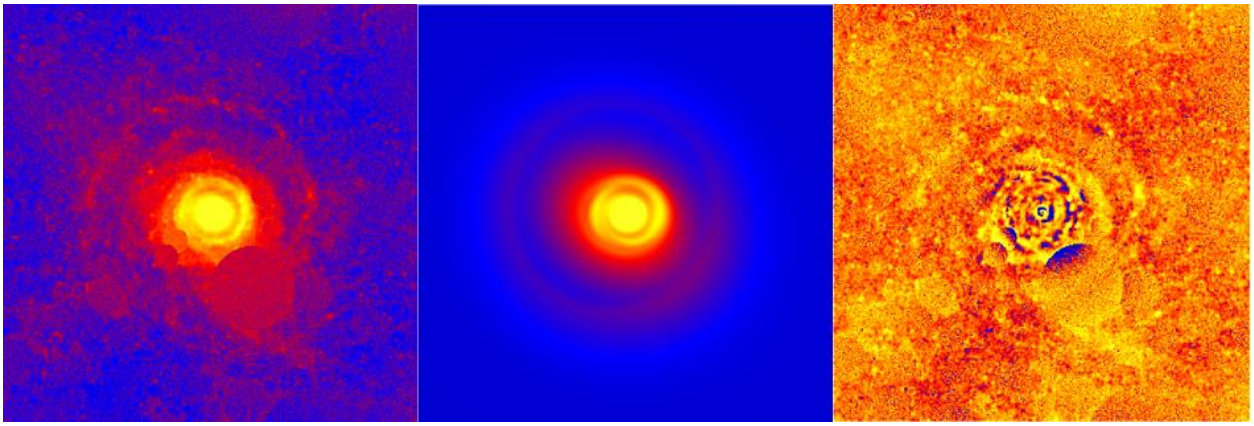

Figure 3.4 Left: Masked Luminance image of UGC 4599. Center: Galfit model using off-center truncated rings to reproduce observed structure. Right: Residual Image after subtraction of model from original.

Creating a GALFIT model for UGC 4599 involves decomposing the galaxy into several components. In this case, there is the Sersic profile core region, an exponential disk region, a bright star forming ring, and the spiral structure. Modeling of the galaxy was attempted with spirals as well as truncated ring structures. Although the galaxy image is likely composed of a large spiral structure, because of the interference of foreground stars, especially the very bright star near the galaxy, modeling of the spiral using broken rings produced better residuals and illustrates the breaking of the galaxy's inner ring well.

Another model was made, ignoring nonaxisymmetric structure entirely and instead solely reproducing the Sersic profile core of the galaxy, an exponential disk, and the star forming ring. The residuals of this model strongly bring out the spiral structure of the galaxy. It should be noted, as the image produced is a residual of subtracting the core-ring model from the original image, some of the interior spiral structure may not be true signal, but rather artifacts from subtracting an imperfect model from the original image. This is especially true in the case of the

ring structure, which is not completely symmetrical in the real galaxy and therefore imperfectly subtracted. Even so, the illustration of the likely location of the inner part of the spiral (which appears to extend inward beyond the star forming ring) is helpful in confirming the pitch angle measurement of the galaxy.

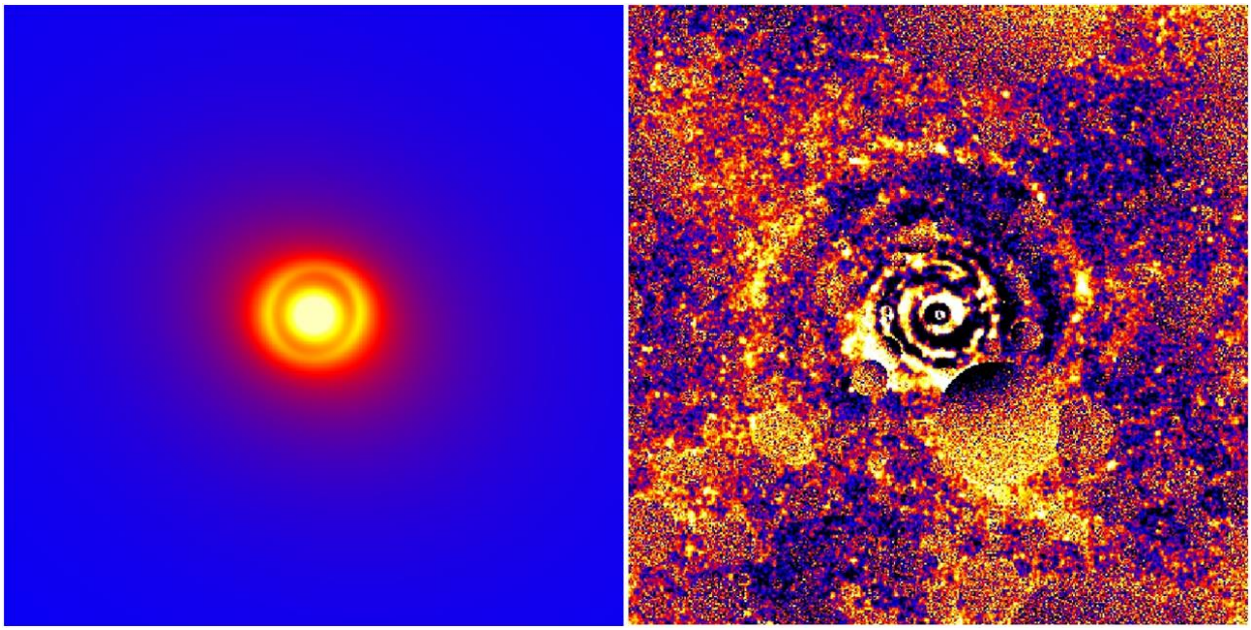

Figure 3.5 Left: GALFIT model of elliptical-like core and star forming ring of UGC 4599. Right: Residuals of Core plus Ring model for UGC 4599. One arm spiral extending in to the center of the galaxy is visible, as well as hints of a second (weaker) arm. Imperfect removal of the star forming ring makes it difficult to determine whether a second spiral is truly present. Ring removal may introduce artifacts in the residual image. Extension of the one dominant spiral arm to large galactic radii is also apparent.

3.5 Galactic Spiral Arm Pitch Angle

There are many techniques in use to measure the pitch angle of galactic spirals. Here, we use three different methods: a simple image overlay code, a Two Dimensional Fast Fourier Transform (2DFFT) (Davis et al. 2016), and a template fitting code called Spirality (Shields et al. 2015) which optimizes median pixel brightness along the arms in a spiral coordinate system.

Both 2DFFT and Spirality require images to be prepared in such a way that spiral structure is the dominant feature in the image. Galaxies must be deprojected to be face-on for measurement. Deprojection is often accomplished using the IRAF routines ellipse and magnify to find and correct for the ellipticity of the galaxy by stretching it back to a circular structure. Though the bright foreground stars in the image for UGC 4599 make it difficult to tell the shape of the disk, the nearly circular star forming ring provides a good reference point. Luckily, the ring of UGC 4599 is already very close to face-on.

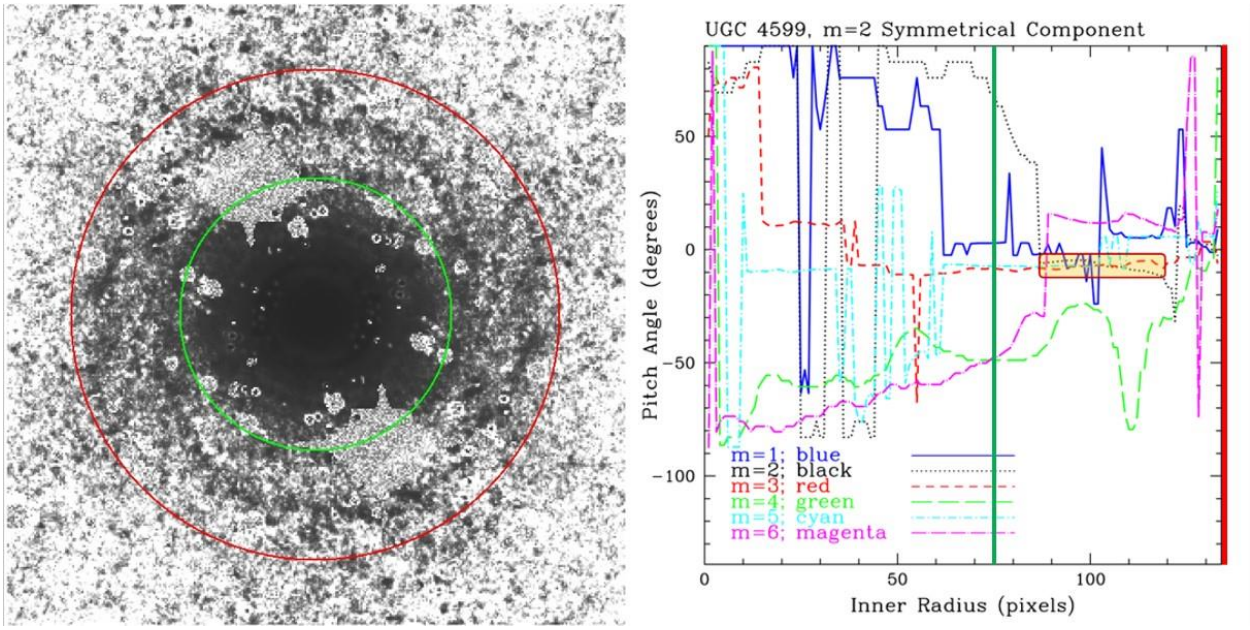

Figure 3.6 Left: Symmetrical component image (m=2) of UGC 4599 for pitch angle measurement. The inner and outer radii (green and red) shown correspond to the region of the galaxy where pitch angle measurement was possible. Right: 2DFFT results for UGC 4599. A region of stable pitch angle is identified (shaded box) in the outer region of the galaxy and pitch angle is measured. The absolute value of the pitch angle is near 6 degrees.

The bright foreground stars in the field of UGC 4599 initially caused both 2DFFT and Spirality to either fail or produce poor measurements of the pitch angle. This occurred even after masking or star subtracting the images. Instead of using the original image, an m=2 symmetrical component image of the galaxy is produced and used to measure the logarithmic spiral arm pitch

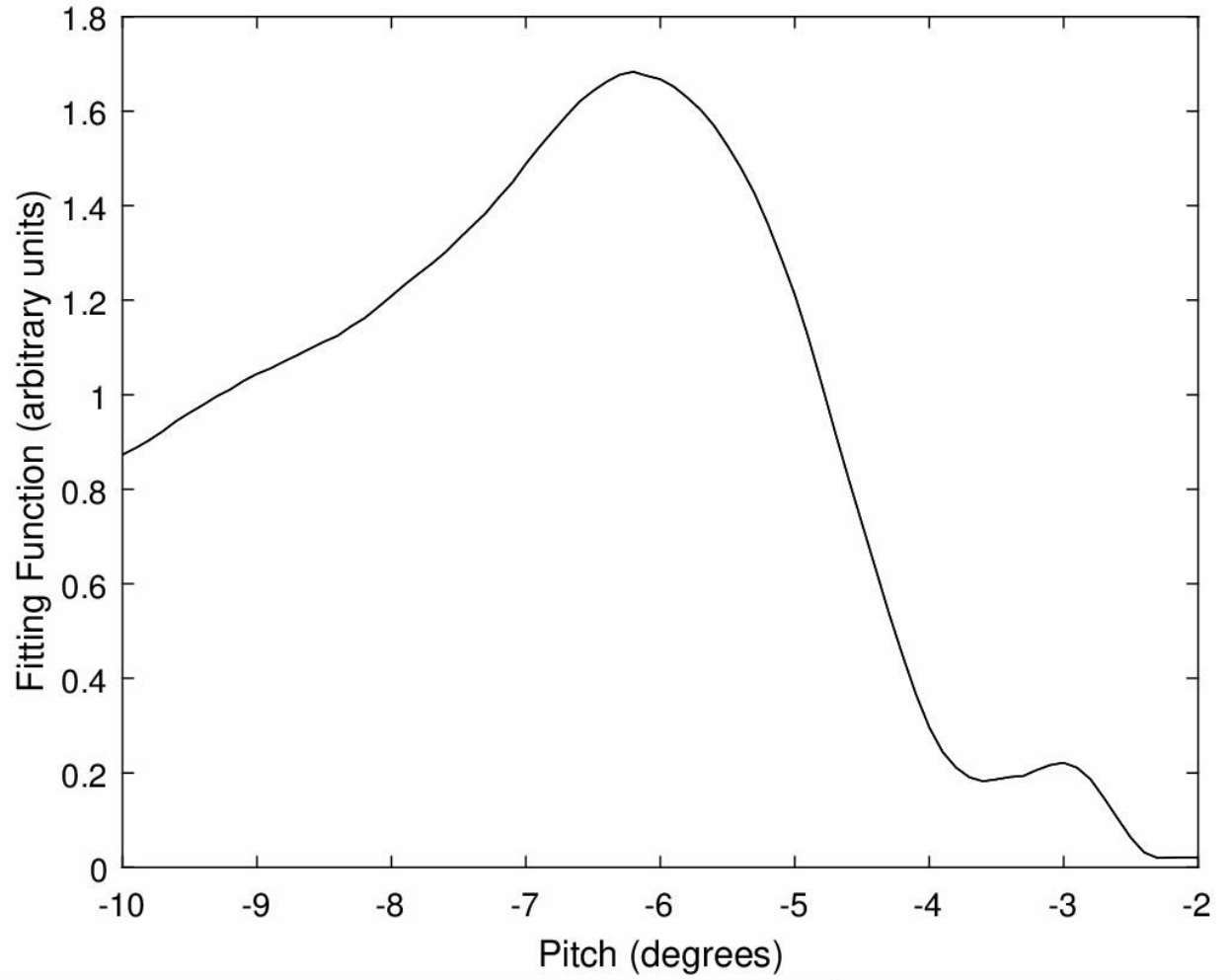

Figure 3.7 Spirality fit for the m=2 symmetrical component image of UGC 4599. The fitting function shows a peak near an absolute value of 6 degrees for the pitch angle of the spiral, in agreement with the results from 2DFFT and manual spiral overlays.

angle of the dominant spiral arm in the outer regions of the galaxy. The two methods largely agree on the pitch angle of the galaxy from the symmetrical component image.

Their results are confirmed using a manual input spiral overlay with m=1 or m=2 spiral arms. The m=2 overlay at the best fit pitch angle appears to overlap with some signal in the galaxy which is not nearly as clear an arm as the m=1 feature, but nonetheless is consistent with a fainter second arm.

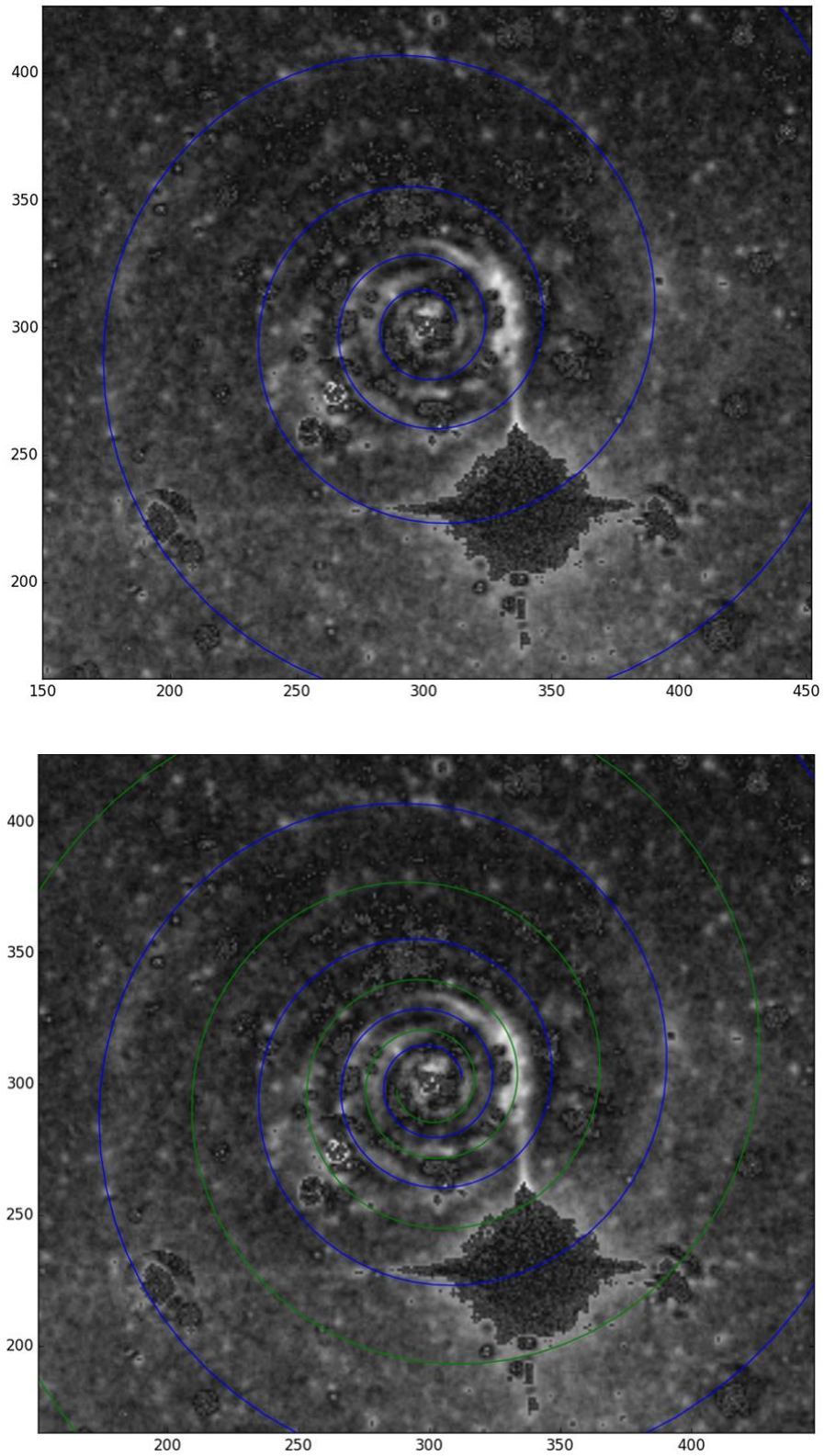

Figure 3.8 Spiral overlays of 1 arm (top) and 2 arm (bottom) best fit spiral structure for UGC 4599. One of the arms is much more apparent; the other there are hints of spiral structure, though not as clearly defined.

The manual best fit spiral overlay, 2DFFT, and Spirality together produce a weighted average result of $6.49^{o}\pm1.49^{o}$. The individual results are as follows: 2DFFT gives $6.85^{o}\pm3.55^{o}$, Spirality gives $6.55^{o}\pm2.88^{o}$, and a spiral overlay gives $6.5^{o}\pm2.0^{o}$. All three measurement methods result in pitch angles within one degree of one another. A pitch angle of $\sim6^{o}$ falls on the low end of spiral galaxy pitch angles, which corresponds to the higher mass end of SMBH masses for spiral galaxies.

3.5.1 The M-P Relation and Density Wave Theory

A correlation between the mass of galactic supermassive black holes and spiral galaxy pitch angle is observed in (Seigar et al. 2008; Berrier et al. 2013; Davis et al. 2015,2017). This so called M-P relation is helpful in measuring the SMBH masses of galaxies who do not have well defined velocity dispersions or where other spectrographic methods for measuring pitch angles are not available. The M-P relation has also been shown to have less scatter than some other methods when applied to spiral galaxies (Davis et al. 2017).

The basis for the M-P relation is Modal Density Wave Theory (Lin et al. 1969), which describes galactic spiral structure as a density wave pattern generated at the inner and outer Linblad resonance orbits in the galaxy. The pitch angle of the spiral arms depends on the ratio of the mass density in the disk to the mass in the central region of the galaxy. A fundamental plane relation among SMBH mass, pitch angle, and density of neutral hydrogen gas is discussed in Davis et al. (2015). Higher central masses result in tighter spiral arm windings, as do higher neutral hydrogen gas densities.

Spiral density waves have been observed in gravitational systems at many different scales. The rings of saturn have been shown to contain complex patterns of density waves (Shu 1984). Protoplanetary disks have also been more recently confirmed to contain density wave spiral structure (Perez et al. 2016). Both of these cases (planetary ring and stellar system scale) are examples of resonances which are forced by a companion body to the central mass. In the case of Saturn the companions are the many moons, while in planetary disks the growing planets are likely drivers of the spiral structure. For grand design spiral galaxies, there are some striking examples of very well defined spiral structure driven by companion dwarf galaxies, an example case being M51. However, while density waves are amplified when driven by a companion, no companion is strictly necessary to create spiral structure.

In the case of UGC4599, we have a galaxy which appears to have the central structure of an elliptical galaxy, but also spiral structure. It would be expected, and it is indeed shown from pitch angle measurement that the central SMBH of UGC 4599 is estimated to have a mass consistent with the high mass end of spiral galaxies or on the lower mass end of elliptical galaxies.

For UGC 4599 we measure the pitch angle as $6.49^{o}\pm1.49^{o}$. Using the equation from (Davis et al. 2017) below, we arrive at an estimated SMBH mass for UGC 4599 of $\text{Log10}(M/M_{o})=7.81\pm0.19$, corresponding to a black hole mass of $6.46*10^{7}M_{o}$. This places UGC 4599 on the high end of spiral galaxy SMBH masses and the lower end of elliptical galaxy SMBH masses (for late type SMBH mass functions see Davis et al. (2014), for a thorough review of black hole mass functions see Kelly and Merloni (2012)). UGC 4599 shares some characteristics with both elliptical and spiral galaxies; it is not all that surprising it would fall in this intermediary mass range as the galaxy may be the result of a major merger history.

3.6 Surface Brightness Mapping

In order to quantify the brightness of the faint outer spiral structure of UGC 4599 a surface brightness map of the galaxy in a more common filter system than luminance is desired. This is accomplished by calculating a conversion from the instrumental luminance filter magnitude to Sloan r magnitude. Several stars of known u,g,r,i,z magnitudes in the field of UGC 4599 were selected. Aperture photometry of 18 of these stars is completed using the IRAF routine DAOPHOT. Luminance instrumental magnitudes for the stars are then compared to the SDSS g and r magnitudes of these objects to derive an equation which may be used to convert from pixel counts in our image to values of r mag. per square arcsecond for each pixel in the image.

In this way, we are able to produce a surface brightness map of UGC 4599 in a close approximation for Sloan r. Using this method to get from luminance to r band, we must adopt a g-r value for each pixel we convert. In this case, we assign a global g-r value of 0.16 to the image, in accordance with the Finkelman & Brosch (2011) value for the star forming ring of UGC 4599. The choice of this global g-r value is due to the outer spiral structure we are most interested in being likely to have similar color characteristics to the bright star forming ring, namely young and blue. However, this global assumption results in the redder core of the galaxy producing slightly inaccurate (skewed high) r surface brightness values in our map. As the surface brightness calculated depends on the g-r value chosen, it is possible to check how the surface brightness map is changed with different values of g-r assigned as the global image value. The effect of varying the globally assumed g-r across a reasonable range of values is to shift inward or outward the contours of the surface brightness map by a few kpc.

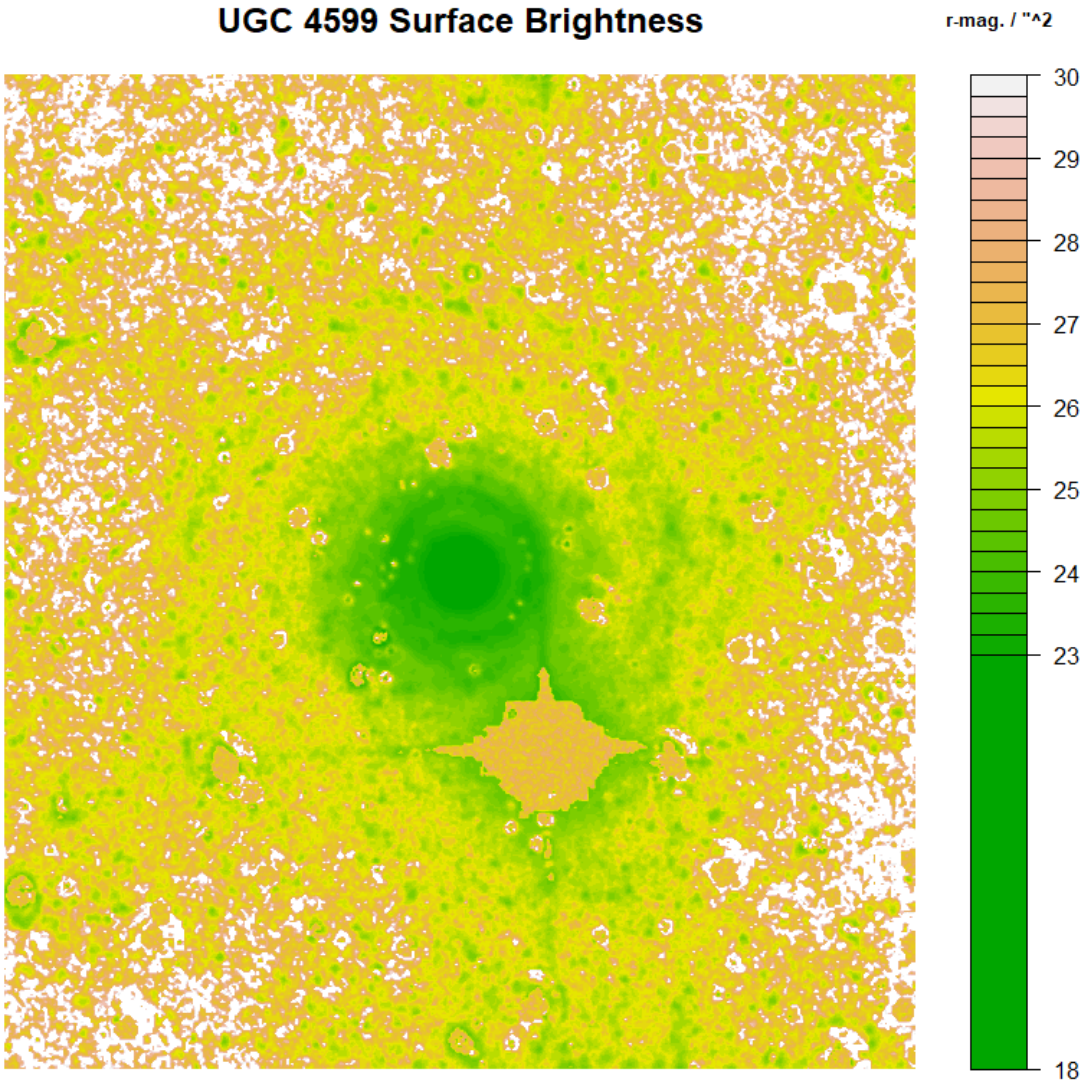

Figure 3.9 Surface brightness profile of UGC 4599 in r magnitudes per square arcsecond. Map is created by converting from Luminance filter instrumental magnitudes to r magnitudes through use of comparison stars in the field. An assumed global g-r value of 0.16 is used in the conversion, as consistent with the g-r in the star forming ring as found by (Finkelman & Brosch, 2011).

If our surface brightness map is imperfect, the contours are systematically either too high or too low depending on the input value of our assumed g-r compared to that of the outer region of the galaxy.

3.6.1 Error

Error propagation is completed taking into account the errors in g,r magnitudes of the 18 comparison stars, the errors in our instrumental photometry, and the goodness of fit of the comparison between our instrumental and the archival magnitudes. These errors are propagated through the conversion from counts per pixel to surface brightness in r magnitudes per square arcsecond for each pixel to find a final error value.

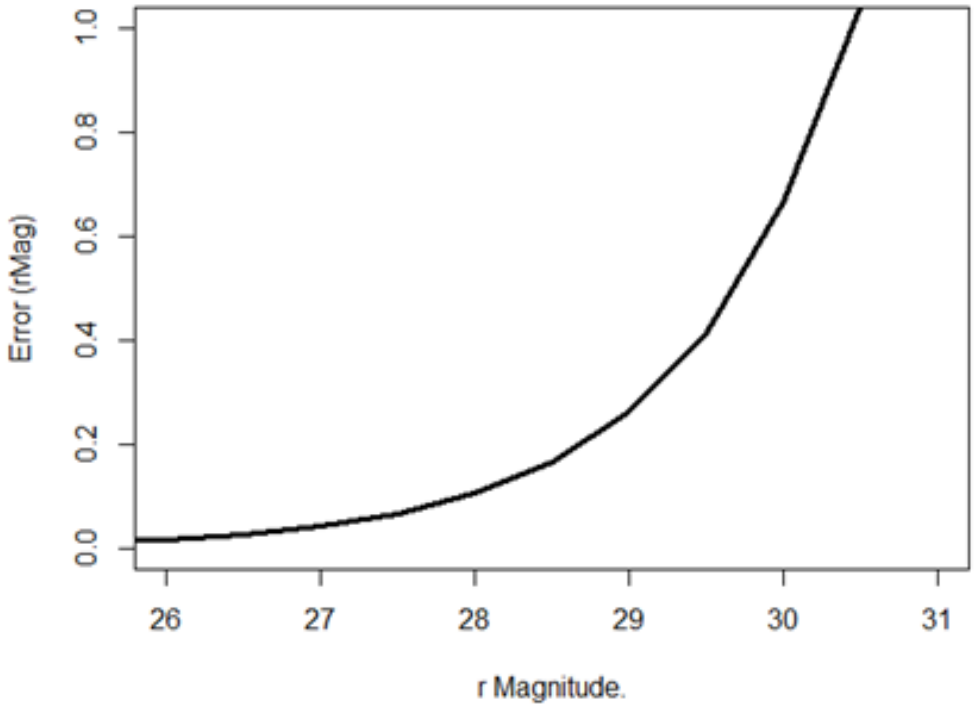

Figure 3.10 Error propagation in converting from our Luminance filter counts to r filter magnitudes. Each pixel in the surface brightness map images has an associated r magnitude error which depends on the original recorded counts for that pixel. Associated errors begin to grow after 26th magnitude per square arcsecond, with uncertainty reaching .5 magnitudes at roughly 29th magnitudes per square arcsecond. These error estimates corroborate our observations of structure becoming indiscernible by eye near these values.

Error in r magnitudes as a function of magnitude is calculated. Our errors increase as the number of counts of signal approaches zero, with the error for an individual pixel reaching 0.5 r magnitudes at roughly 29.5th r magnitude, and over 1 r magnitudes at 30.5th r magnitude. To some extent, this error estimate is a proxy for the observing limit of the telescope, where the elbow of the error curve for individual pixels occurs somewhere near the faintest surface brightness objects which may be observed by the telescope for this integration time. This error curve is, however, for individual pixels while real features extend across many pixels. While an individual pixel may fade into the sky noise a group of pixels which are together slightly above the sky mean may produce enough signal to be viewed.

In terms of finding errors within regions rather than individual pixels, if we assume no pixel to pixel covariance for an approximation, pixels in the region might be treated as individual measurements and a standard error calculated as $\sigma/\sqrt{n}$. For example if you have a 5x5 pixel region near 30.5th magnitudes per square arcsecond, each pixel has roughly ±1 magnitude associated error, but the error in the mean of the region is something like $1/\sqrt{25}$, or a more reasonable 0.4 mag. This extension of what can be called the limiting magnitude is seen in the outermost structure of UGC4599, where individual pixels fade into the sky noise but radially concentric regions of pixels are collectively high enough above the noise to be noticed as signal.

As there are so few counts of signal in the outer region of the galaxy, the outermost contours of surface brightness depend very strongly on knowledge of the mean of the sky counts. Having a flat sky value across the image is important for producing an accurate map. A mask to flatten the sky value was applied to remove a slope in sky value (on the order of 1-2 counts) across the image. In the star subtracted image as displayed in DS-9, it is possible for the human eye to pick out some extremely faint structures even where the surface brightness profile has

reached its limit. This suggests while we can make an accurate mapping of the surface brightness out to 29th magnitude or so, the true limiting magnitude of our instrumentation when examining extended features extends perhaps another magnitude or two from the measurement limit.

3.7 Radial Surface Brightness Profiles

In more fully characterizing the structure of UGC 4599 it is useful to produce radial profile maps of the galaxy. A radial profile of the galaxy is made through the use of a routine developed for IRAF called Isofit which is an improvement on the commonly used routine Ellipse (Ciambur 2015), paired with the use of a python software designed to decompose I(r) tables, ellipse tables, or isofit tables into galactic components called Profiler (Ciambur 2016). These components include sersic cores, truncated or antitruncated exponential disks, gaussians to model features like rings, and others. We also make use of the software IMFIT (Erwin, 2015), with similar model parameters.

Radial cuts of UGC4599 were taken along several different axes from the center of the galaxy out to its edge. These radial cuts were converted into I(r) tables and imported into the Profiler 2.0 for fitting. In reproducing the radial structure of UGC4599 some features are more apparent than others. First is the Sersic profile core region of the galaxy. Outside this is the star forming ring, modeled as a gaussian. There may be some disk structure present in the radial cuts but a better fit is arrived at using a sersic core plus gaussians for the ring and spirals. Finally, we have the two spiral arms, crossed through twice each in the radial cuts. This m=2 spiral is more readily observed in radial I(r) cuts than by eye or in attempting pitch angle measurement techniques. Both arms are present in several radial cuts through the galaxy. When the four radii points of the arms are paired and plugged into the equation for spiral pitch angle, both arms

return values of approximately 6 degrees for the associated spiral, in yet another confirmation of the spiral arm pitch angle as measured earlier with other methods.

In addition to radial cuts, the code Isofit is used to create tables of the profile of the galaxy. These are similar to IRAF ellipse tables, with a few extra features. Unfortunately, even

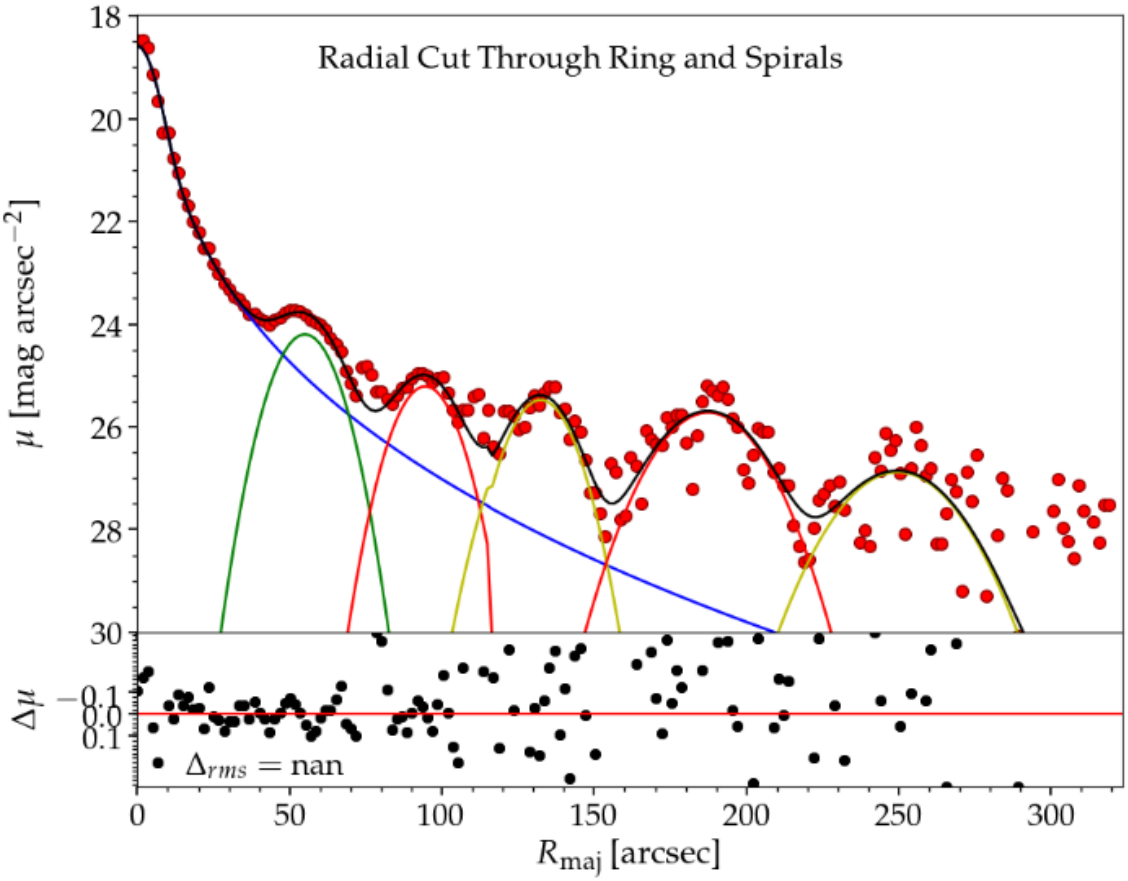

Figure 3.11 Radial surface brightness profile of UGC 4599 calibrated to SDSS r magnitudes per square arcsecond. This profile takes cut of pixels in a line through a part of the galaxy where the spiral structure and ring are clearly present. Star forming ring and spiral arms are modelled using gaussian functions and show up as bumps in the radial profile. The star forming ring is marked in green, and each arm is marked in red and gold respectively, showing a two arm spiral structure. The radius values of the arm locations for both arms, when inserted into the equation of a logarithmic spiral, correspond well with the 6 degree spiral we have calculated through other methods. Residuals of model from data are shown below main chart.

after star subtraction, the many foreground stars in the field of UGC 4599 make it difficult to trust the harmonic values beyond the simple ellipticity and position angle parameters. However, there is still some utility in getting the Isofit profile of the galaxy. In the Isofit profile, the disky component of the galaxy is better incorporated into the model while the spiral structure largely disappears as it is not a radially symmetric feature. The star forming ring and sersic core are still visible.

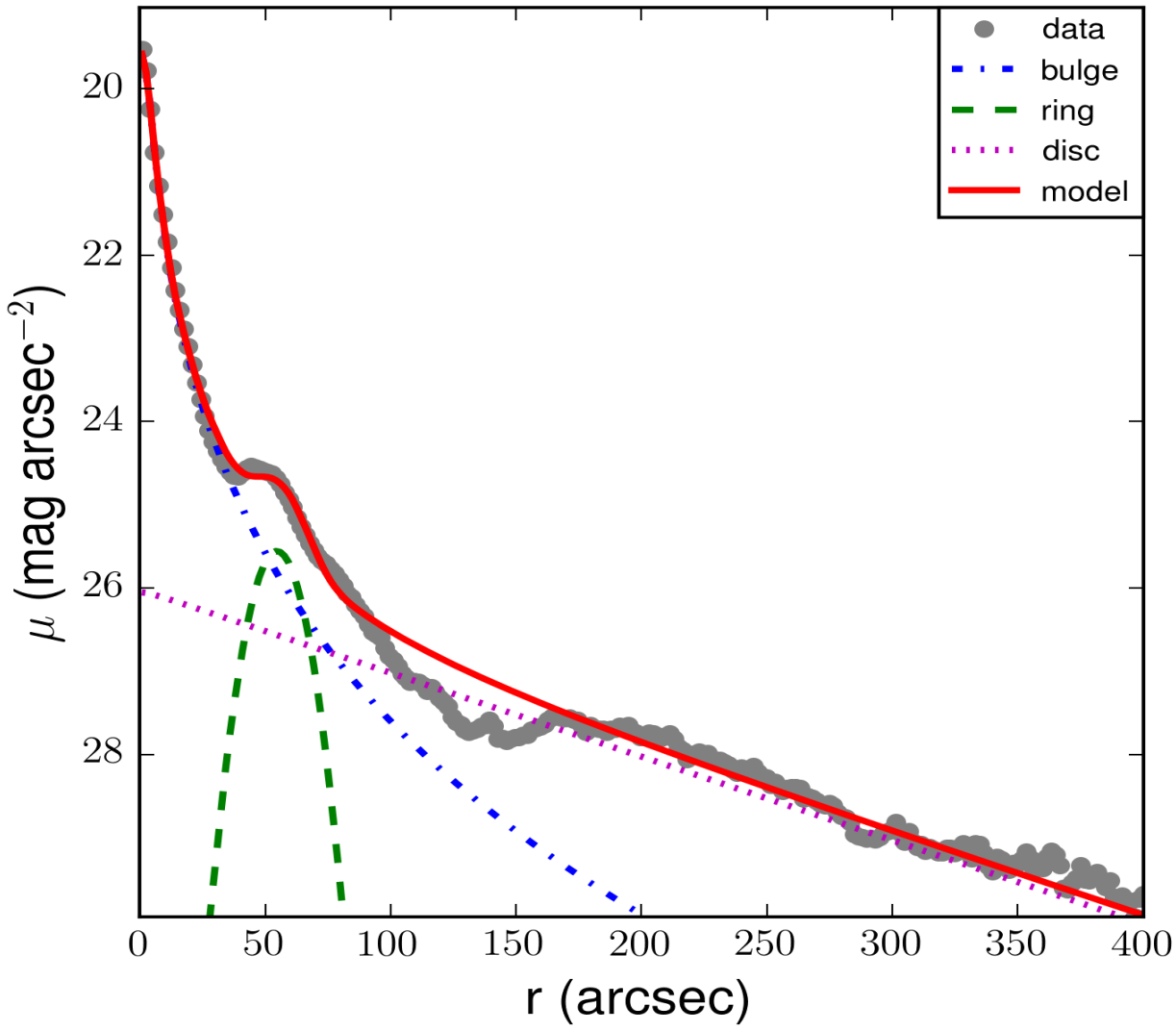

Figure 3.12 : IMFIT fit of UGC 4599 Luminance band image in r equivalent azimuthal surface brightness. Components include central bulge, star forming ring, and exponential disk. Spiral structure is masked in preprocessing before this fit. Note the extrapolated central surface brightness of the disk component is very faint, at 26th magnitude per square arcsecond.

With the combination of the Profiler fits for the radial I(r) tables and the Isofit tables of UGC 4599, and IMFIT fitting, the structure of the galaxy may be characterized as a central Sersic component, a star forming ring near 70 arcsec(~9 kpc), a very faint disk with central surface brightness of I_o=26 mag/arcsec^2 and H=17.96 kpc extending to beyond 450 arcsec (~60kpc), and two optical spiral arms extending to roughly 300 arcsec (~40 kpc), with one arm being more prominent than the other, both with pitch angles near 6 degrees.

3.8 UGC 4599 in UV and HI

The faint spiral structure of UGC 4599 is now confirmed in several different wavebands. While present in GALEX UV images, we reimage UGC 4599 in u band with the DCT at Lowell. Reimaging with the DCT allows a much better resolution than GALEX images (0.24" on DCT vs. 1.5" with GALEX). This image (see Figure 3.12) clearly shows the spiral structure and has the benefit of less interference from the foreground stars than the optical images of the galaxy. The ALFALFA survey (Giovanelli et al. 2005) at Arecibo has imaged UGC 4599 in radio. Column density mapping of HI in UGC 4599 on the Karl G. Jansky Very Large Array (VLA) shows a clear one armed spiral in the gas.

When overlaid with both the optical and the u band images of UGC 4599, the contours of the m=1 HI spiral match very well with the u and l band one armed spiral. However, both optical and uv images of UGC 4599 show some indicators of an additional spiral arm, making the symmetry m=2 rather than m=1. It may be that the gas has a strong m=1 symmetry while the stars show a weaker second arm.

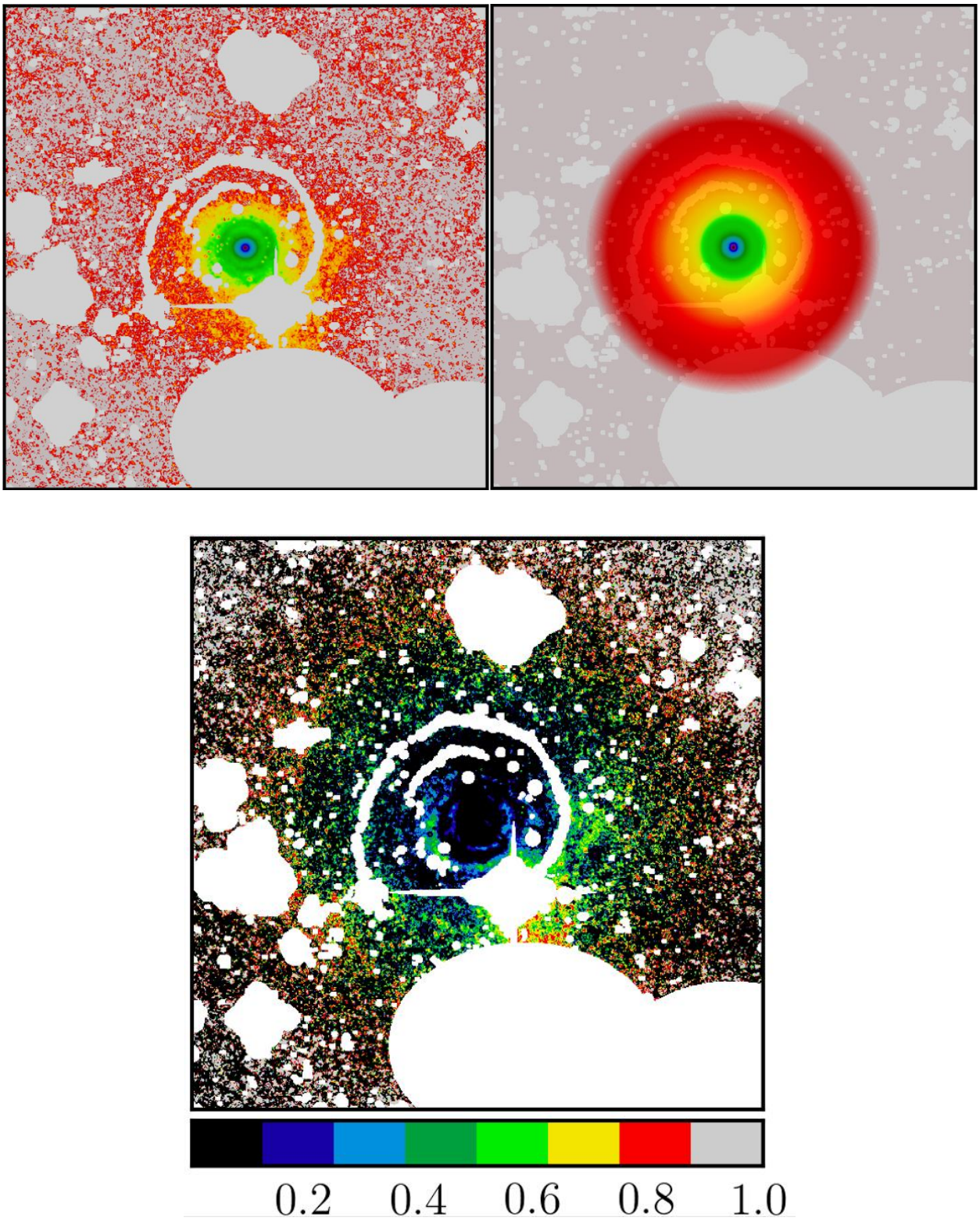

Figure 3.13: Top-left: Masked Image of UGC 4599 with spirals and foreground stars masked to NaN. Top-right: IMFIT Model fit of radial surface brightness profile for UGC 4599. Bottom: Relative Residual Image of (Observed-Model)/Observed for the image.

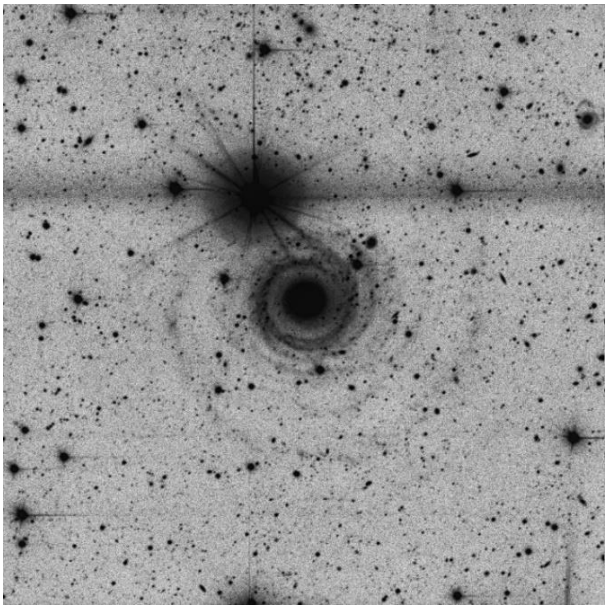

Figure 3.14 UGC 4599 u band image obtained with the DCT. Strong one armed spiral is clearly visible with some fainter sprial structure between the outer spiral and the star forming ring.

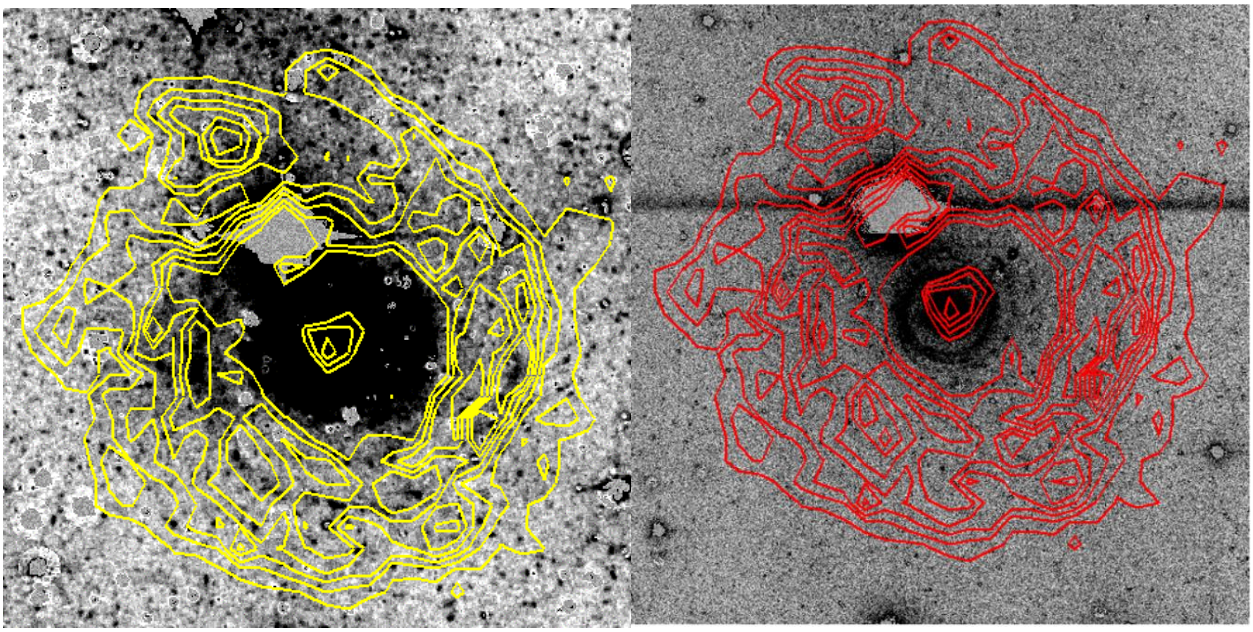

Figure 3.15 Left: Overlay of UGC4599 Luminance band image with contours of Neutral Hydrogen as detected by the Very Large Array. The contours of the one armed spiral seen in the hydrogen gas overlay cleanly with the optical spiral. This suggests the stars in the spiral to be young (blue) as is confirmed in their UV detection in the GALEX survey and in the DCT u band image.

Right: Overlay of UGC4599 u band image from the DCT with contours of Neutral Hydrogen as above. Similarly to the optical spiral, the UV spiral fits well with the HI m=1 arm.

3.8.1 Star Formation Rates of UGC 4599 from u Surface Brightness

With the u band image from the DCT, it is possible to measure the star formation rate in the various regions of UGC 4599. We divide the galaxy into three main regions of star formation: the core region, the ring, and the disk/spirals. The core region in our model is defined from the center of the galaxy to a radius in the gap between the bright center and the star forming ring, from a radius of 0 kpc to 4.4 kpc. We define the ring region as the annulus from 4.4 kpc to 8.3 kpc. Finally, we define the disk/spiral region as the annulus from 8.3 kpc to 28.2 kpc. There may be some flux outside the 28.2kpc radius but it is at very low signal to noise compared to the background sky. We also calculate a total SFR for the galaxy using the sum of the SFRs in each of these regions.

The formula (equation 3.1) used to derive the SFR is that of Wyder et al. (2009), which uses a modification of a relation between UV luminosity and star formation from Kennicutt (1998) to surface brightness.

Equation 3.1: $\log10(\Sigma\ SFR) = 7.413 - 0.4 * \mu\ UV$

This method assumes a constant star formation rate and Salpeter (1955) stellar initial mass function (IMF). Since our galaxy is near to face on, we assume a face-on orientation and optically thin disk. We do not account for dust reddening or extinction.

We calculate the u surface brightness in umag per square arcsec for each pixel using similar methods as earlier in this paper for the luminance band images. Star subtraction of the u image was performed using DAOPHOT, and iterative sigma clipping implemented in order to decrease the value of the residuals left over from star subtraction. Three foreground stars with known Sloan u magnitudes in the field of view of the image are selected and photometry

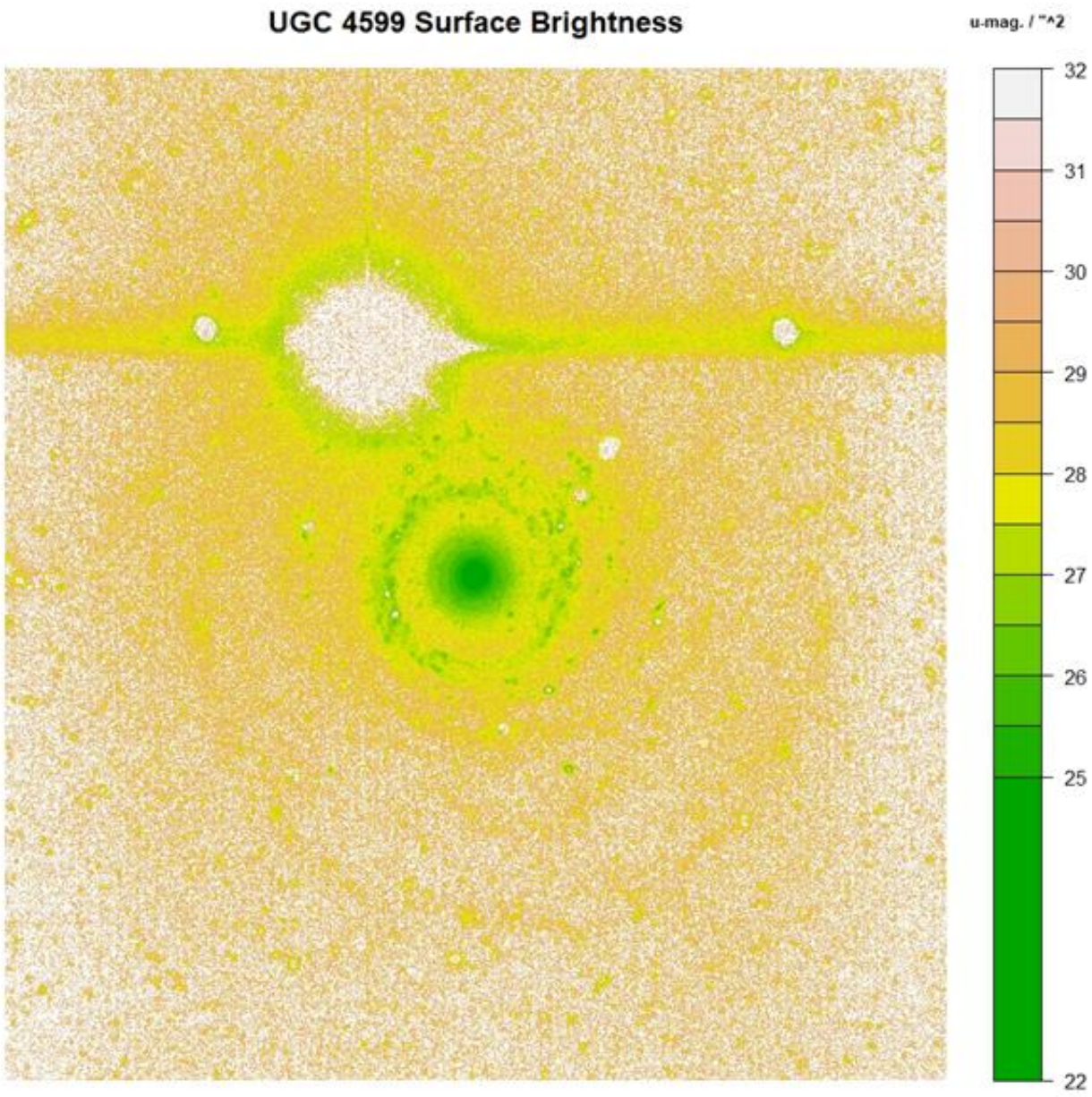

Figure 3.16 Surface brightness image of UGC 4599 in u filter. Stars have been subtracted with DAOPHOT and image has been iteratively sigma clipped to reduce star subtraction residuals. Spiral structure is visible outside the star forming ring in UV as in optical.

performed. These stars were then used to convert pixel values from counts to surface brightness values.

The Wyder et al. (2009) method for finding the SFR relies on a measure of the FUV surface brightness of the galaxy. While our images are in Sloan u, we are able to correct to FUV using the FUV-NUV color for UGC 4599 of 0.6±0.06 as reported in Finkelman & Brosch (2011). After doing so, we find the SFRs for the three regions of UGC 4599. For the core region, the SFR is $5.07\pm0.68*10^{-4}$ $M_o/yr/kpc^2$, with a total of 0.031±0.004 M_o/yr. For the ring region, the SFR is $1.52\pm0.2*10^{-4}$ $M_o/yr/kpc^2$, with a total of 0.024±0.003 M_o/yr. For the disk/spiral region, the SFR is $0.45\pm0.13*10^{-4}$ $M_o/yr/kpc^2$, with a total of 0.088 M_o/yr. In total, we find the SFR for UGC 4599 to be 0.143±0.013 Mo/yr.

In the ring, Finkelman & Brosch (2011) report an estimated SFR using the method from Salim et al. (2007) of 0.04 M_o/yr, which is in better agreement with our ring values before correcting from u to FUV. However, Finkelman & Brosch (2011) use a different annulus to define the ring of the galaxy (5.1-8.5 kpc as compared to our 4.4 to 8.3 kpc). There is substantial flux at the outer edge of our ring but we consider this to visibly be part of the spiral structure. At the inner edge, it appears they chose the inner edge of the ring while we chose a point in the gap between the ring and the core. This should not have much effect on the SFR as the UV flux in the gap is small.

The process for measuring the UV flux outside the star forming ring is a bit more arduous than that of the rest of the galaxy, as stray light from the extremely saturated foreground star, along with light from imperfect star subtraction become factors in producing an accurate SFR. Pixels in the disk/spiral region from which to determine an average surface brightness, and in turn SFR for this region, were selected to minimize the amount of false positive flux from foreground stars. The preprocessing step of iteratively sigma clipping the image at different radii was helpful here in that the maximum value of the star subtraction residuals in the outer regions

of the galaxy are not much higher than the highest values of the spiral arms at that radius. We estimate the upper bound of this false positive flux and its effect on the estimated SFR. Our SFR for the disk/spiral is likely high by no more than 0.006 M_o/yr. This yields a corrected disk/spiral SFR of 0.082±0.013 M_o/yr.

Even after down-correcting to account for imperfectly subtracted foreground stars, it is interesting to note that while the star formation rate per square kpc is highest in the core region and lowest in the spirals, 62% of the total star formation in the galaxy is contributed by the faint outer spiral structure, while the core and ring contribute roughly 21% and 17% respectively. Though the outer spiral structure is much fainter than the core or ring, the diffuse star formation over a larger area adds up to a higher total contribution.

3.9 Conclusion

This research more closely examines the galaxy UGC 4599 in its low surface brightness outer regions. We confirm and extend findings of previous work which identify the possibility of spiral structure in the galaxy. The surface brightness of this spiral structure is measured in luminance, Sloan r equivalent, and u filters, as well as overlaid with an HI map of the galaxy. In HI, optical, and UV, one spiral arm with a pitch angle of P=6.49°±1.49°, corresponding to an SMBH mass for UGC 4599 of $6.98*10^7$ M_o. This falls on the high end of masses for late type galaxies. There are also some indications in the spiral structure of a second, fainter arm at m=2 symmetry to the first, dominant arm. We measure star formation rates for the core, ring, and disk/spiral rings of the galaxy as well as the galaxy as a whole. A majority of the star formation occurring in the galaxy is actually contained in the faint spiral regions rather than the core/ring. We measure a

total star formation rate of 0.143±0.013 M_o/yr. UGC 4599 should be considered a Giant Low Surface Brightness Galaxy with a High Surface Brightness central region composed of a core and ring analogous to Hoag's Object.

3.10 Acknowledgements

These results made use of the Discovery Channel Telescope at Lowell Observatory. Lowell is a private, non-profit institution dedicated to astrophysical research and public appreciation of astronomy and operates the DCT in partnership with Boston University, the University of Maryland, the University of Toledo, Northern Arizona University and Yale University. The Large Monolithic Imager was built by Lowell Observatory using funds provided by the National Science Foundation (AST-1005313). This research was funded in part by NASA through the Arkansas Space Grant Consortium.

3.11 Bibliography:

Abraham, R. G., & van Dokkum, P. G. 2014, PASP, 126, 55

Appleton, P. N., & Struck-Marcell, C. 1996, Fundamentals of Cosmic Physics, 16, 111

Berrier, J. C., Davis, B. L., Kennefick, D., et al. 2013, ApJ, 769, 132

Boissier, S., Boeselli, A., Ferrarese, L. et al. 2016, A&A, 593, A126

Bothun, G., Impey, C., & McGaugh, S. 1997, PASP, 109, 745

Brosch, N., Finkelman, I., Oosterloo, T., Jozsa, G., & Moiseev, A. 2013, MNRAS, 435, 475

Brosch, N., Kaspi, S., Niv, S., & Manulis, I. 2015, Ap&SS, 359, 914

Buta, R., & Combes, F. 1996, Fundamentals of Cosmic Physics, 17, 95

Ciambur, B. C. 2015, ApJ, 810, 120—. 2016, PASA, 33, e062

Das, M. 2013, Journal of Astrophysics and Astronomy, 34, 19

Davis, B. L., Berrier, J. C., Shields, D. W., et al. 2016, 2DFFT: Measuring Galactic Spiral Arm Pitch Angle, ascl:1608.015

Davis, B. L., Graham, A. W., & Seigar, M. S. 2017, MNRAS, 471, 2187

Davis, B. L., Berrier, J. C., Johns, L., et al. 2014, ApJ, 789, 124

Davis, B. L., Kennefick, D., Kennefick, J., et al. 2015, ApJ, 802, L13

Erwin, P. 2015, ApJ, 799, 226

Finkelman, I., & Brosch, N. 2011, MNRAS, 413, 2621

Freeman, K. C. 1970, ApJ, 160, 811

Giovanelli, R., Haynes, M. P., Kent, B. R., et al. 2005, AJ, 130, 2598

Hoag, A. A. 1950, AJ, 55, 170

Kelly, B. C., & Merloni, A. 2012, Advances in Astronomy, 2012, 970858

Kennicutt, Robert C., J. 1998, ARA&A, 36, 189

Lin, C. C., Yuan, C., & Shu, F. H. 1969, ApJ, 155, 721

Lynds, R., & Toomre, A. 1976, ApJ, 209, 382

Noguchi, M. 2001, MNRAS, 328, 353

Peng, C. Y., Ho, L. C., Impey, C. D., & Rix, H.-W. 2002, AJ, 124, 266 —. 2010, AJ, 139, 2097

P´erez, L. M., Carpenter, J. M., Andrews, S. M., et al. 2016, Science, 353, 1519

Reshetnikov, V., & Sotnikova, N. 1997, A&A, 325, 933

Rich, R. M., Brosch, N., Bullock, J., et al. 2017, in IAU Symposium, Vol. 321, Formation and Evolution of Galaxy Outskirts, ed. A. Gil de Paz, J. H. Knapen, & J. C. Lee, 186–189

Salim, S., Rich, R. M., Charlot, S., et al. 2007, ApJS, 173, 267

Salpeter, E. E. 1955, ApJ, 121, 161

Schweizer, F., Whitmore, B. C., & Rubin, V. C. 1983, AJ, 88, 909

Seigar, M. S., Kennefick, D., Kennefick, J., & Lacy, C. H. S. 2008, ApJ, 678, L93

Shields, D. W., Boe, B., Pfountz, C., et al. 2015, arXive-prints, arXiv:1511.06365

Shu, F. H. 1984, in IAU Colloq. 75: Planetary Rings, ed.

R. Greenberg & A. Brahic, 513–561
Whitmore, B. C., Lucas, R. A., McElroy, D. B., et al. 1990, AJ, 100, 1489

Wyder, T. K., Martin, D. C., Barlow, T. A., et al. 2009, ApJ, 696, 1834

Zhu, Q., Xu, D., Gaspari, M., et al. 2018, MNRAS, 480, L18

4 An Assessment of Capabilities and Limitations of Logarithmic Spiral Arm Pitch Angle Measurement Techniques

4.1 Abstract

This study evaluates the galactic spiral arm logarithmic pitch angle measurement capabilities of the commonly used code sets 2DFFT and Spirality. This is accomplished through performing pitch angle measurement on a set of simulated galaxies created using the software GALFIT. The simulated galaxies are inserted into a portion of Hubble Ultra Deep Field with Poisson noise added. A survey of the pitch angles of these galaxies is conducted in an attempt to recover the initial pitch angles of the templates.

We find the 2DFFT and Spirality methods to perform similarly under most conditions, with Spirality having a slight favorability for galaxies with high (>40º) pitch angles. The main failure modes for both code bases are the radial pixel size of the galaxy being too small (<20pixels), the inclination angle being too large (>75º), the arm-interarm contrast of the galaxy being too low. These weakening and failure of measurement are expressed through either outright failure to converge on a pitch angle or through higher associated errors in the pitch angle measurement. For galaxies with bars, the effective measurement radius is the distance from the outer edge of the bar to the outer edge of the galaxy. False positive rates are low (~1%), and when they occur the expressed pitch angle is usually either very small, wrong chirality, or a factor of 2 off from the correct pitch angle.

4.2 Introduction

The logarithmic spiral arm pitch angle of late type galaxies has been shown to correlate to several other galactic properties. There are covariances among several galactic properties including rotational velocity (Davis et al., 2019), galaxy luminosity (Tully & Fisher, 1977), bulge mass (Graham, 2016 for review), dark matter halo properties (Loeb & Rasio 1994, Haehnelt et al. 1998, Silk & Rees 1998). One such correlation of interest is the Supermassive Black Hole (SMBH) Mass – Pitch Angle, or M-Φ relation (Seigar et al., 2008). The M-Φ relation is based in modal density wave theory (Lin & Shu, 1964), but the same correlation might also apply in other theories of spiral arm origins such as swing amplification (Kormendy, 1981) **.** There are many techniques commonly used to measure SMBH masses, but many of these require spectroscopy and have more scatter than the M-Φ relation when applied to late type galaxies without classical bulges (Davis et al., 2017). The M-Φ relation, on the other hand, only requires sufficiently resolved images of the galaxy to observe spiral arms in order to make a mass estimate for the central black hole. This non-spectral approach is able to be extend SMBH mass measurements to higher redshifts in an effort to study the evolution of SMBH in spiral galaxies. In the early universe, most galaxies show less defined grand spiral structure, with the oldest spiral galaxy considered to be at a redshift of z~2 (Law et al., 2012).

The M-Φ relation has also been extended to a planar relationship among SMBH mass, pitch angle, and neutral hydrogen density in the galactic disk with improved scatter compared to the traditional M-Φ relation (Davis et al., 2015). This plane results from the dependency of pitch angle on the mass ratio of the central object and the disk. If there is gas mapping information available for the galaxies studied, the SMBH estimate may be corrected along this plane.

Two commonly used techniques for the measurement of logarithmic spiral arm pitch angle are the codes 2DFFT (Berrier et al., 2013) and Spirality (Shields et al., 2015). These scripts approach the problem of spiral arm measurement in very different ways. 2DFFT is a two dimensional fast Fourier transform code which decomposes the galaxy a sum of spirals, outputting the dominant pitch angle for the galaxy. Measurements are taken in annuli, varying the inner radius of measurement from zero to the outer edge of the galaxy. Spirality is a script written in MATLAB which generates template spirals in a spiral coordinate system and fits the observed galaxy spiral to the best fit template in order to find the pitch angle.

While the scripts 2DFFT and Spirality have been used in previous studies to measure the spiral arm pitch angles in galaxies, the limitations of performance of these techniques for different galaxy morphologies and observation conditions has not been assessed to date. In this study, we simulate a large range of realistic two armed galaxy morphologies in GALFIT (Peng et al., 2002), and evaluate the performance of 2DFFT and Spirality at measuring their pitch angles. Understanding the limitations of these pitch angle measurement codes will assist in correcting studies of pitch angle distributions for galaxies whose pitch angles evaded measure due to intrinsic properties or image properties. We provide a fuller assessment of the errors associated with these measurement techniques toward this end.

4.3 Methods

In order to test the failure modes of the pitch angle measurement codes 2DFFT and Spirality we measure the effect of several different parameters on pitch angle measurements and their associated errors. These include the pitch angle itself, arm-interarm contrast for the spiral arms, radius of the galaxy in pixels, surface brightness of the galaxy (signal to noise), inclination

angle, and radial bar fraction. To this end, we must create a set of galaxies which allows these parameters to be manipulated from galaxy to galaxy.

4.3.1 Galaxy Template Creation with GALFIT

GALFIT (Peng et al., 2002) is a galaxy modelling software which is capable of either fitting real galaxies or generating model galaxies from scratch. The latest iteration of GALFIT (Peng et al., 2007) has a variety of new capabilities including the inclusion of nonaxisymmetric features such as spiral arms. This serves to our advantage in creating a set of initial template galaxies for our study.

We generate a set of high resolution template spiral galaxies with large (1000 pixel) radii in GALFIT. These galaxies are comprised of a core Sersic profile fixed with n=1.25, an m=2 spiral structure with five different Fourier mode strengths (0.1 to 0.5 by 0.1), eight different pitch angle settings (from 5 to 40 degrees by 5 degrees), and three different bar settings (none, 1/3 of galactic radius, 2/3 of galactic radius).

The value of n in the Sersic profile core was chosen as a typical value for spiral galaxies and held constant in order to isolate this variable from the other variables to be tested. The parameter of Fourier mode strength is a proxy for arm-interarm contrast, with higher Fourier mode strengths presenting higher contrast spiral arms. There is no direct input parameter in GALFIT for pitch angle (controlled by 3+ input variables), and the hyperbolic tangent spirals GALFIT uses to incorporate bars are not perfectly logarithmic. The pitch angle issue is corrected by setting the pitch angle manually by marking points along the generated spiral and recording the pitch angle. Our spirals are forced to be logarithmic by setting the 95% asymptotic radius (where the GALFIT spiral function asymptotes to logarithmic) to less than one pixel greater than the bar radius. This forces the spirals generated at the ends of the bar to very rapidly approach

logarithmic winding. With pitch angle, Fourier mode strength, and bar fraction controlled we produce 120 template galaxies with 40 for each bar setting.

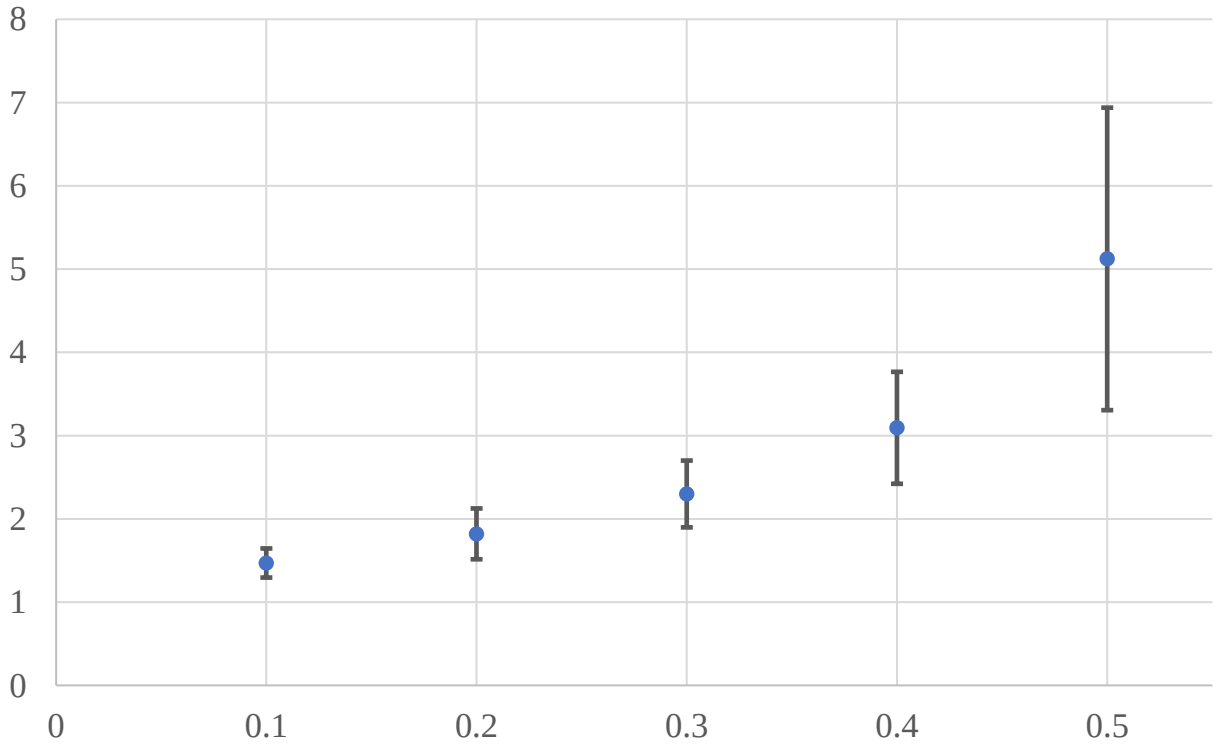

Figure 4.1: Arm-Interarm contrast as a function of Fourier mode strength, as measured using radial I(r) cuts of galaxy images. The arm-interarm contrast of the low Fourier mode strength galaxies is similar, but the failure rates for f=0.1 galaxies are much higher. This might be the result of the broadness vs peakiness of the arms rather than the magnitude of peak to trough.

When the pitch angles of the template galaxies are measured in 2DFFT and Spirality, we find the observed pitch to slightly disagree with the expected pitch from manual fitting. Specifically, the pitch angle measurement codes have a tendency to undershoot the pitch angle for some of these GALFIT model galaxies in the range 10º-25º, with the largest deviation from expected pitch angle of approximately 3º too tight at 15º pitch. We apply these offsets in the pitch angle from the first measurements of the high resolution template images as corrections for the manipulated and degraded versions of these galaxies in our main study.

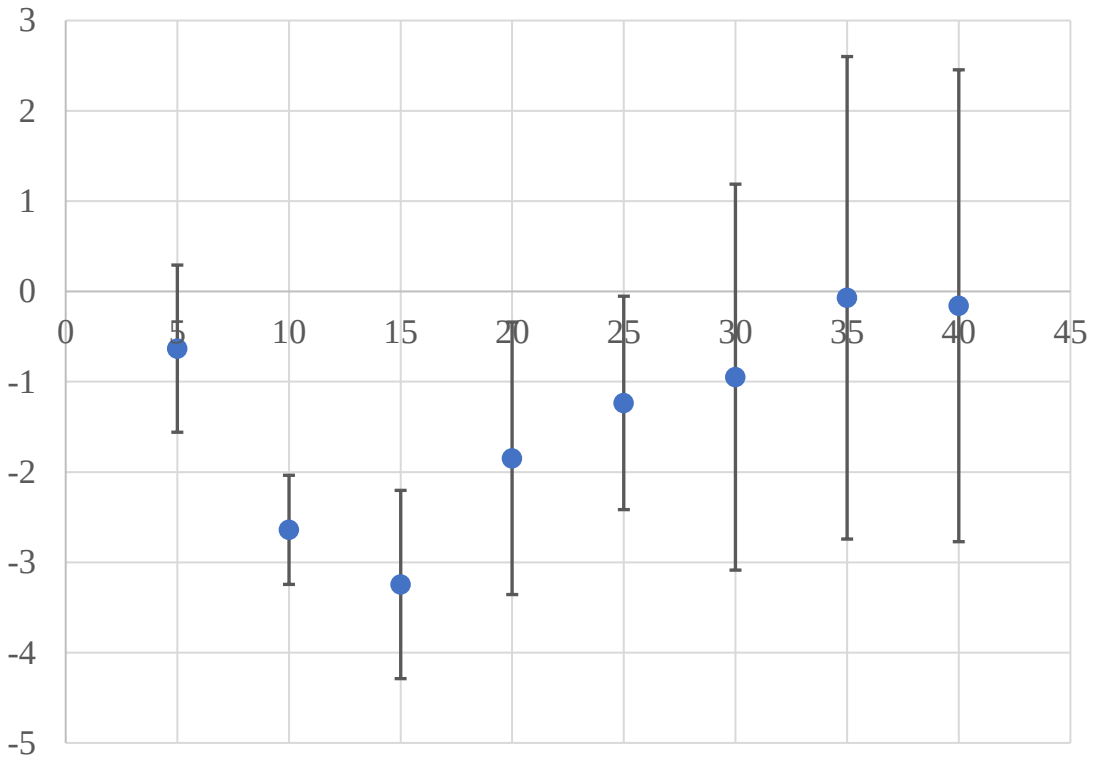

Figure 4.2: Deviation from selected pitch angle as a function of pitch angle. 2DFFT and Spirality are systematically fitting tighter than expected pitch angles, especially in the pitch range from 10º-25º. This may be caused by some properties of the GALFIT template galaxies such as not fully reaching the asymptote to logarithmic pitch angles. We use this measure of the deviation of the templates from their intended pitch angles as a correction table for the manipulated versions of the template galaxies.

When the results of 2DFFT galaxy template measurement are compared against the results of Spirality galaxy template measurement, the recorded pitch angles are nearly identical and fit very closely to a y=x line. This shows that, at least for high resolution images of somewhat idealized smooth and symmetric galaxies, the two pitch angle measurement codes will result in a consistent measure of the pitch angle of the galaxy. Deviations from the expected pitch angle in each pitch angle bin were greatest for galaxies with the largest bars. While 2DFFT and Spirality both appear to encounter some difficulties in measuring barred galaxies, in this case the two codes largely agree in their recorded pitch angle for the barred galaxies. This systematic

undershoot of the value of pitch angle, especially in barred galaxies, might be related to the way these galaxy models are generated in GALFIT. Both 2DFFT and Spirality are somewhat centrally biased for any given measurement, as the core of the galaxy contains more counts than the outer edge. Central biasing may come into play if the pitch angle of the GALFIT templates varies a bit between the bar radius and the outer edge of the galaxy. Deviations from y=x are largest at higher pitch angles, though 2DFFT and Spirality never disagree by more than 2º, and often agree to within a fraction of a degree.

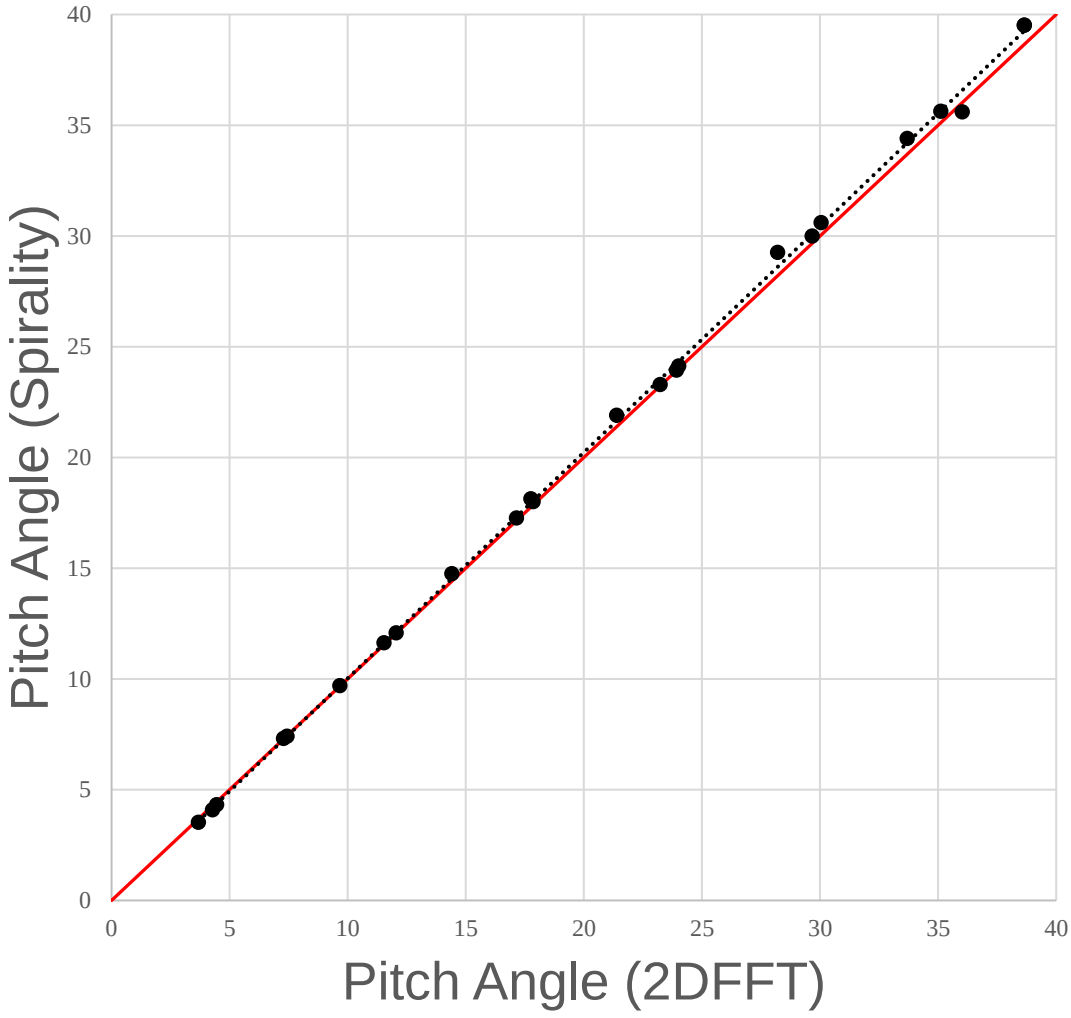

Figure 4.3: Spirality and 2DFFT measurements of template galaxies agree in pitch angle. Dotted line is linear fit to the data, with y=1.02x-0.1721. Solid line is y=x.

4.3.2 Python Pipeline for Template Manipulation

A script was written in Python to input sets of template galaxies and further manipulate them in new sets of variables. These include Dimming Factor (controls surface brightness of the galaxy within user defined range), Chirality (coin toss for winding direction), Rotation Angle (randomly oriented between 0-360 degrees), Inclination angle (randomly inclined within a user set range of inclination angles), and Binning factor (resolution reduction).

Figure 4.4: Left: Template barred galaxy. Right: Post-Python-Pipeline noise added version of the same galaxy. While the noisy versions of the GALFIT template resemble real galaxies, their symmetry is still more perfect than field galaxies.

Poisson Noise is added to the galaxies and they are placed into a field image. The field we have chosen for this study is the Hubble Ultra Deep Field (UDF), in B-band (F435W). Our goals were to identify the limitations of the pitch angle measurement codes in terms of generalizable parameters such as pixel size, arm-interarm contrast, and signal to noise rather than physical units such as arcseconds. This allows the findings here to be applied to galaxies in any field image rather than only being valid for any one survey.

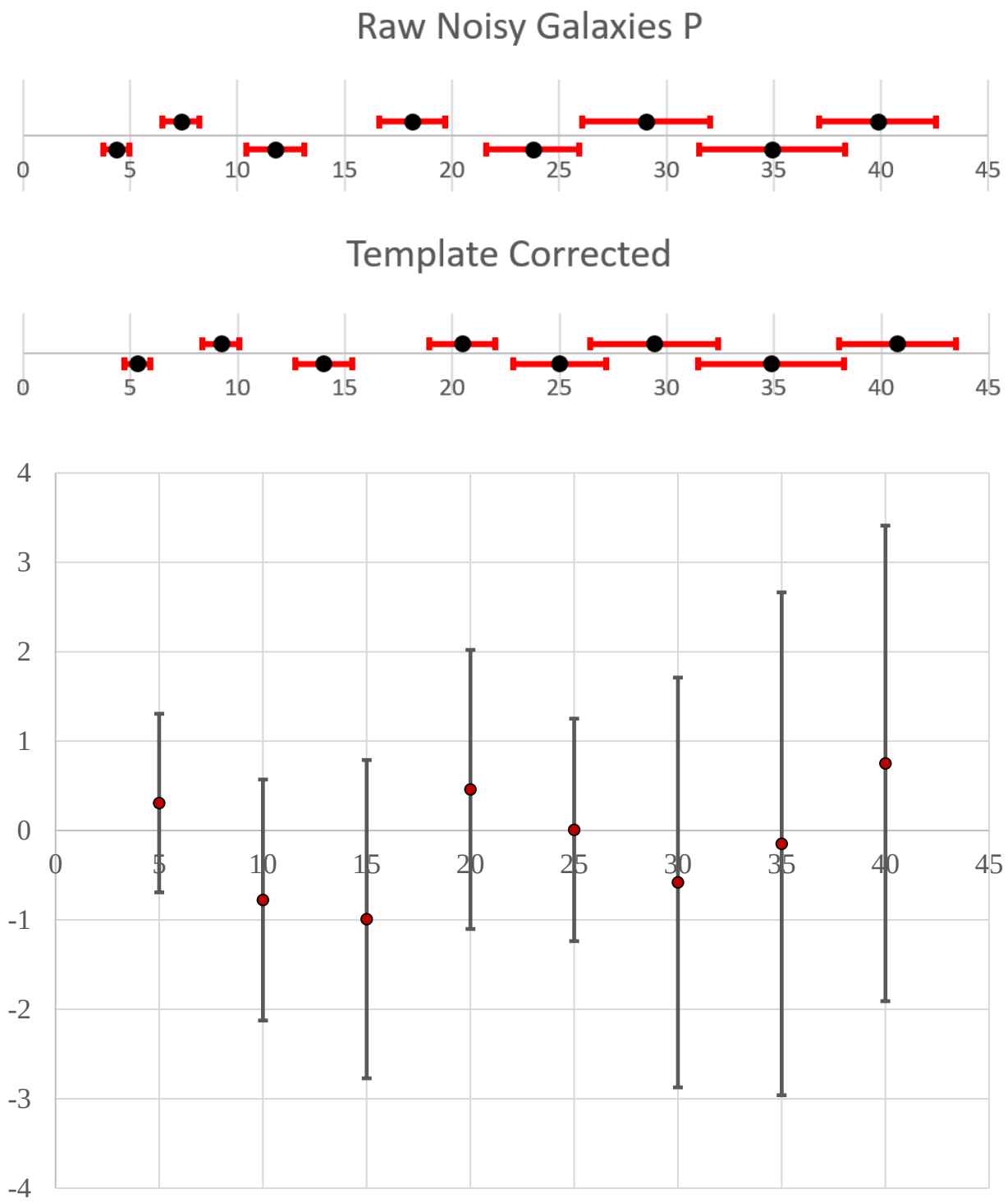

Figure 4.5: Top: 2DFFT and Spirality both systematically undershot the pitch angle for the template galaxies. Applying this correction to the Noisy galaxies yields the desired pitch angles to within error bars.
Bottom: Offset of measured Noisy galaxy pitch angle from template corrected pitch angle. When galaxy measurement is successful, the recorded pitch angle closely matches that of the template galaxy.

Each original set of 40 template galaxies is expanded by a factor of 10, building out a set of 400 galaxies, with the above semi-randomly generated variables. This final set of 1200 galaxies spans a wide subset of possible morphologies, although for now the symmetry is limited to m=2, as 2 armed galaxies are common. This set of galaxies, called here the Noisy set as opposed to the Template set, are then corrected using the offsets in pitch angle from the template galaxy measurements. After correction, the pitch angles of the galaxies fall within error bars of the intended template pitch angles.

4.3.3 Quantization Error

Both 2DFFT and Spirality have associated quantization errors. For 2DFFT, the spacing of possible pitch angles varies as a function of the pitch angle, with the spacing between allowed values of P growing with P. This quantization error becomes the dominant source of error for galaxies with high pitch angles, especially once $P>20^{o}$. In Spirality, this source of error may be remedied for high pitch angle galaxies by controlling the galaxy templates which are generated for fitting in the user input. Correcting this error for 2DFFT would require reworking the source code to deal with high pitch angle galaxies. In this case, Spirality has the potential to outperform 2DFFT in measurement error by simply generating many high pitch angle galaxy templates to compare against.

4.4 Results

The 1200 galaxies of the Noisy galaxy set are measured in 2DFFT and Spirality. These results mainly focus on the subset of 400 galaxies with no bar. The presence of galactic bars mainly increases the associated error as a function of galaxy size and causes pitch angle

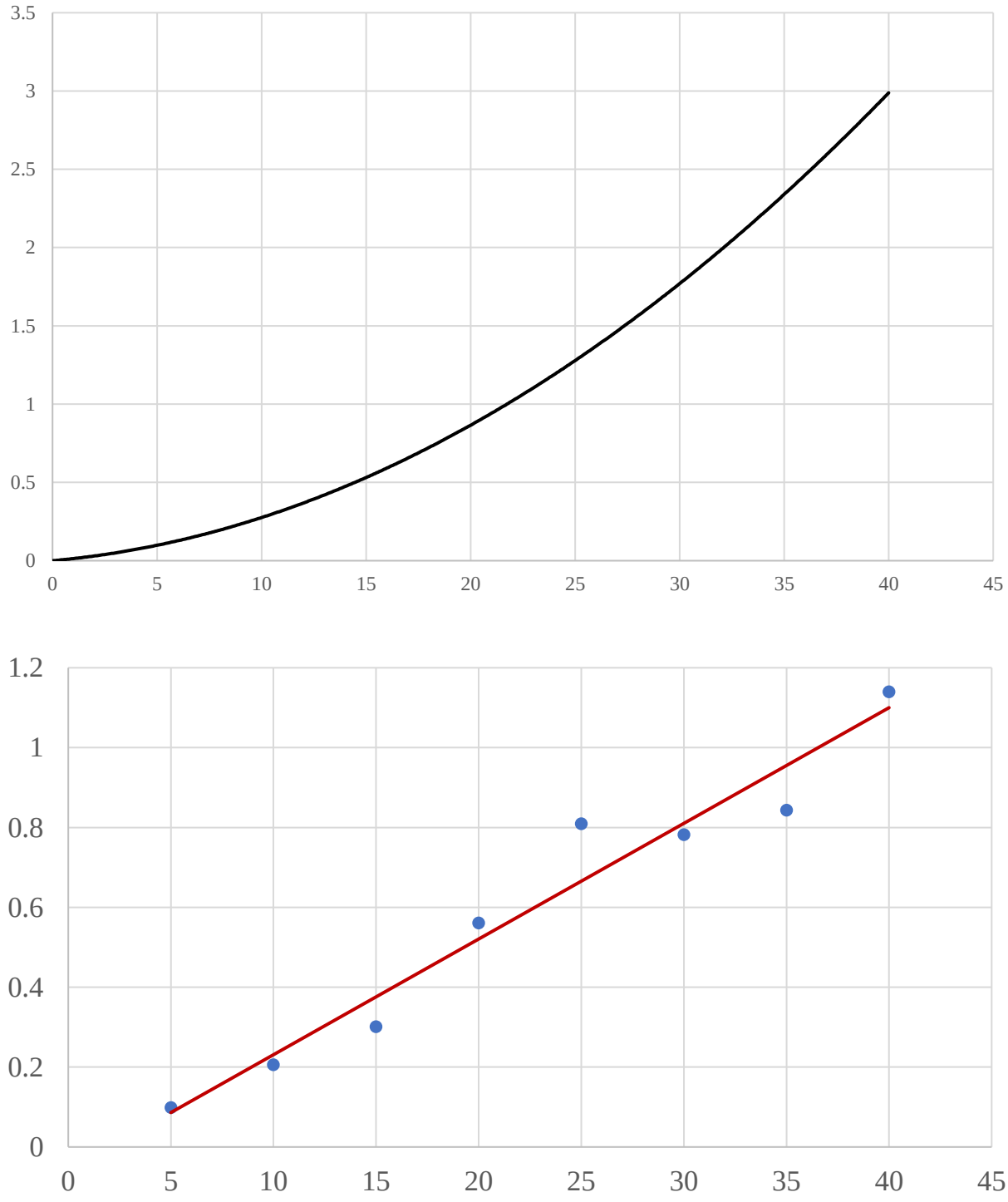

Figure 4.6: Top: Average Intrinsic Error (degrees) due to quantization of pitch angles as a function of P (degrees) for 2DFFT. This source of error contributes to the observation of error in pitch angle measurements growing with the value of P.
Bottom: Fraction of recorded error which is the result of quantization as a function of pitch angle (degrees) for 2DFFT. For pitch angles greater than ~20º, the quantization error becomes the dominant source of error.

measurement failure at smaller radii than the equivalent non-barred versions of the same galaxy. For example, an unbarred galaxy with a radius of 20 pixels which is near the limit of measurement capabilities would have a different minimum radius limit than a galaxy which has 2/3 of its radius as bar. For the same quality of pitch angle measurement, the barred version would need to have ~60 pixels of total radius such that the measurement annulus is near the 20 pixel value.

The capabilities of pitch angle measurement should be assessed along a few different sets of guidelines. First, measurement success rate should be considered. We define a successful measurement as any galaxy which returns a stable region of pitch angle which might be considered a result. However, this pitch angle is not necessarily the 'correct' (template matched) pitch angle for the galaxy. Deviations of the measured pitch from the template pitch are treated as the 'offset error'. The size of this stable region of pitch angles is also recorded, as larger stable regions are associated with lower pitch angle measurement error. Finally, each pitch angle measurement has an associated error value which varies with the quality of the measurement.

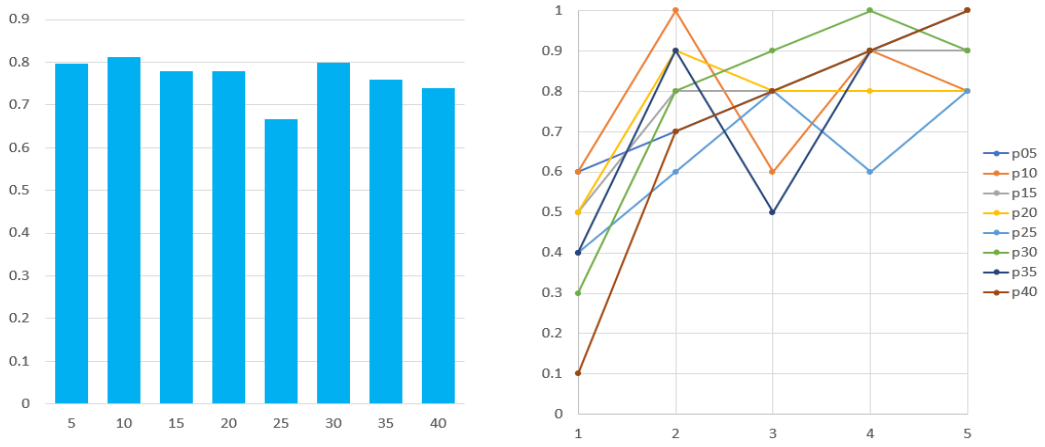

Figure 4.7: Left: Measurement success rate as a function of pitch angle. There is a weak decrease in success rate with P.
Right: Measurement success rate as a function of Fourier mode strength (f=0.1-0.5). High pitch angles at low Fourier mode strengths fail the most often. At low arm-interarm contrasts and high pitch angles, the likelihood of retrieving a pitch angle for the galaxy is low.

4.4.1 Measurement Success and Galaxy Measurement Fraction

We first examine measurement success rate as a function of pitch angle, and as a function of Fourier mode strength. Measurement success rates were near 80% across all pitch angles. The failure rate for the set of 25º galaxies is the result of a few measured galaxies overlapping with real galaxies in the field image. The slightly lower success rates at 35º and 40º pitch are not the result of galaxy overlap and are considered to be a real falloff in success rate. When the galaxies are binned by pitch angle and success rate is plotted against Fourier mode strength, a clear falloff in measurement success rate is visible for the lowest arm-interarm contrast galaxies. When the arm-interarm contrast falls below ~2, the measurement success rate drops off rapidly, with the most drop occurring in galaxies with high pitch angles.

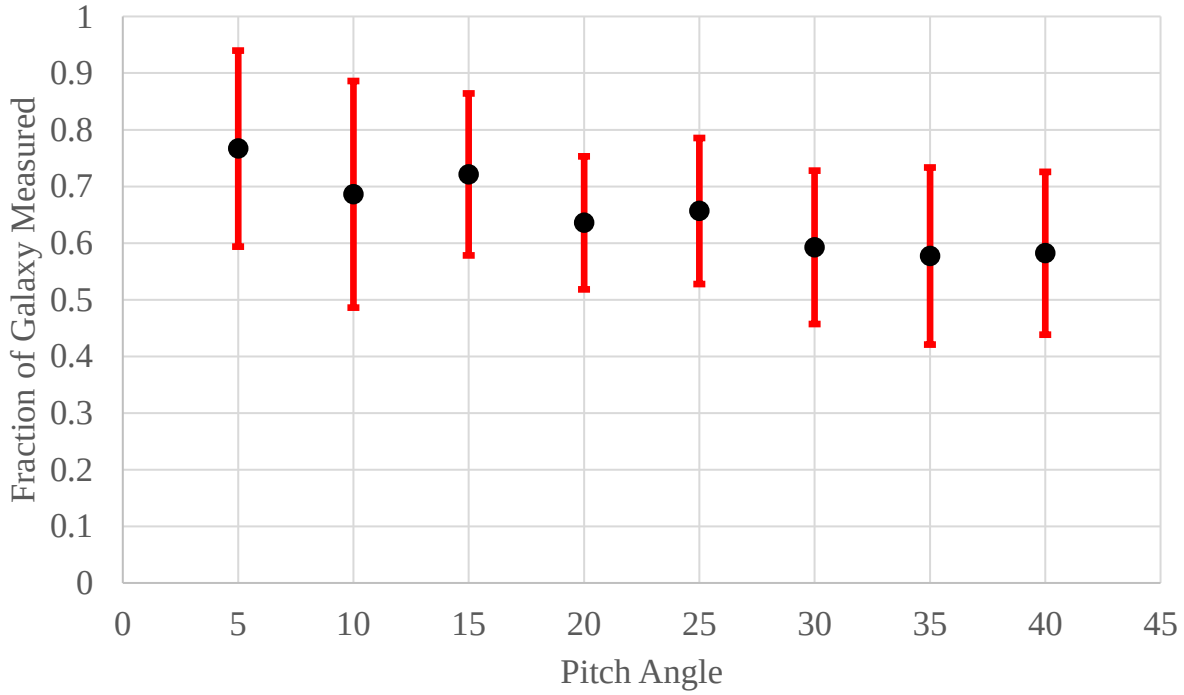

Figure: 4.8 Fraction of the galaxy measured as a function of Pitch Angle for the 400 unbarred galaxy set. The measurement fraction falls off from about 80% at 5º pitch to below 60% at 40º.

The fraction of the galactic radius within the stable region of pitch angles is shown to vary with the pitch angle of the galaxy, with lower galaxy measurement fractions at higher pitch angles. This corresponds to the observed higher error bars for these higher pitch angle galaxies. For the barred galaxy set these fractions are understandably lower by roughly the bar fraction. It should be noted that the low end of the range of fraction measured tends to be populated by the lower Fourier mode strength galaxies and the high end with the higher Fourier mode strength galaxies. Galaxies with 5º pitch and f=0.5 have more than 90% of their total radius as measurable annuli. Meanwhile, galaxies 30º and higher with low Fourier mode strengths may only have 50% or less of their total radius as measurable annuli.

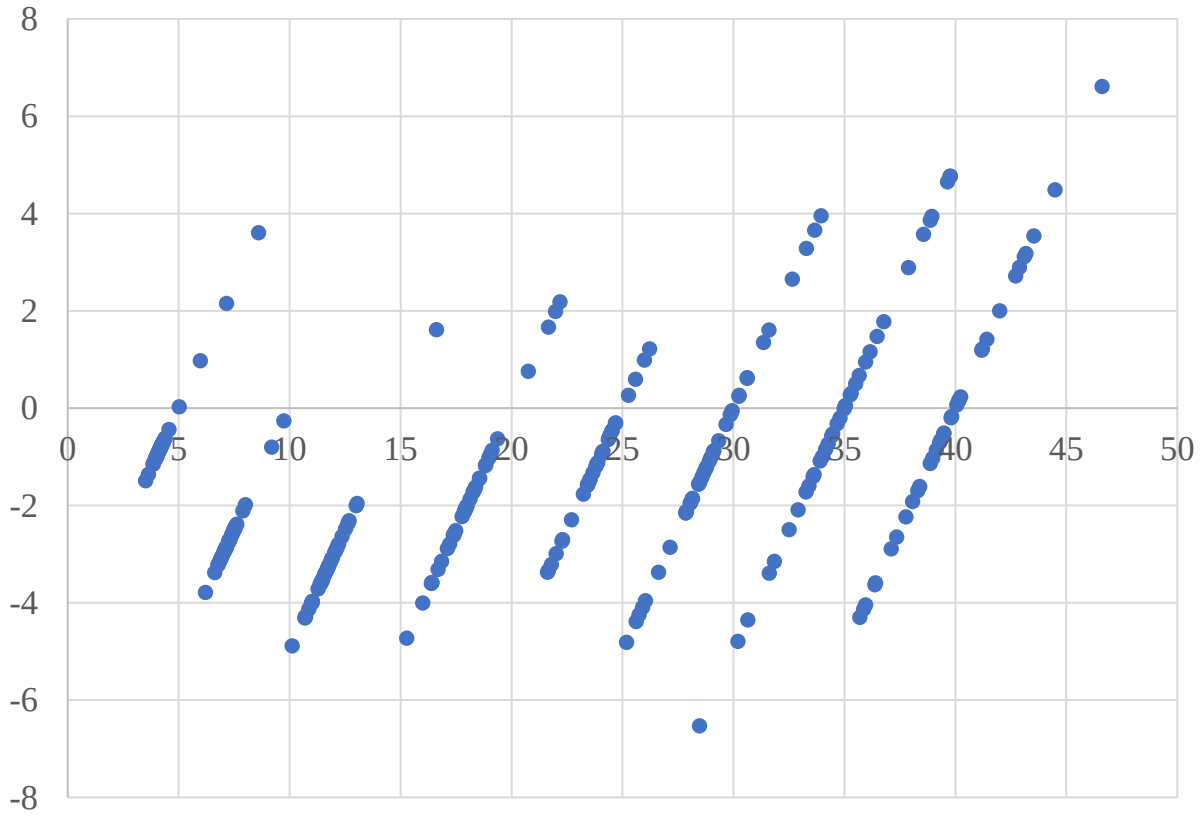

Figure 4.9: Offset of measured pitch angle from template pitch angle (degrees) as a function of measured pitch angle (degrees). The undershoot in measured pitch angle in the low-medium pitch range of galaxies is apparent. The spread of offsets is larger for higher pitch angle galaxies.

Even the noisy set of GALFIT galaxies are highly idealized model structures without the dust lanes, star forming regions, and other clumpy asymmetries of real galaxies. These measurements represent the upper bounds of measurement success. Indeed, even high resolution real galaxies often have radial measurement fractions below 50% and some less than 25% of the galactic radius. The size of the stable region of pitch angle measurement is increased if a simple Sersic profile fit, and possibly exponential disk fit, are subtracted from the galaxy image before pitch angle fitting. This partially eliminates the center-biasing of the codes and amplifies the relative strength of the spiral arms compared to the partially subtracted core/disk. Galaxy stable regions may be expanded by from a few percent to more than a factor of two depending on the galaxy.

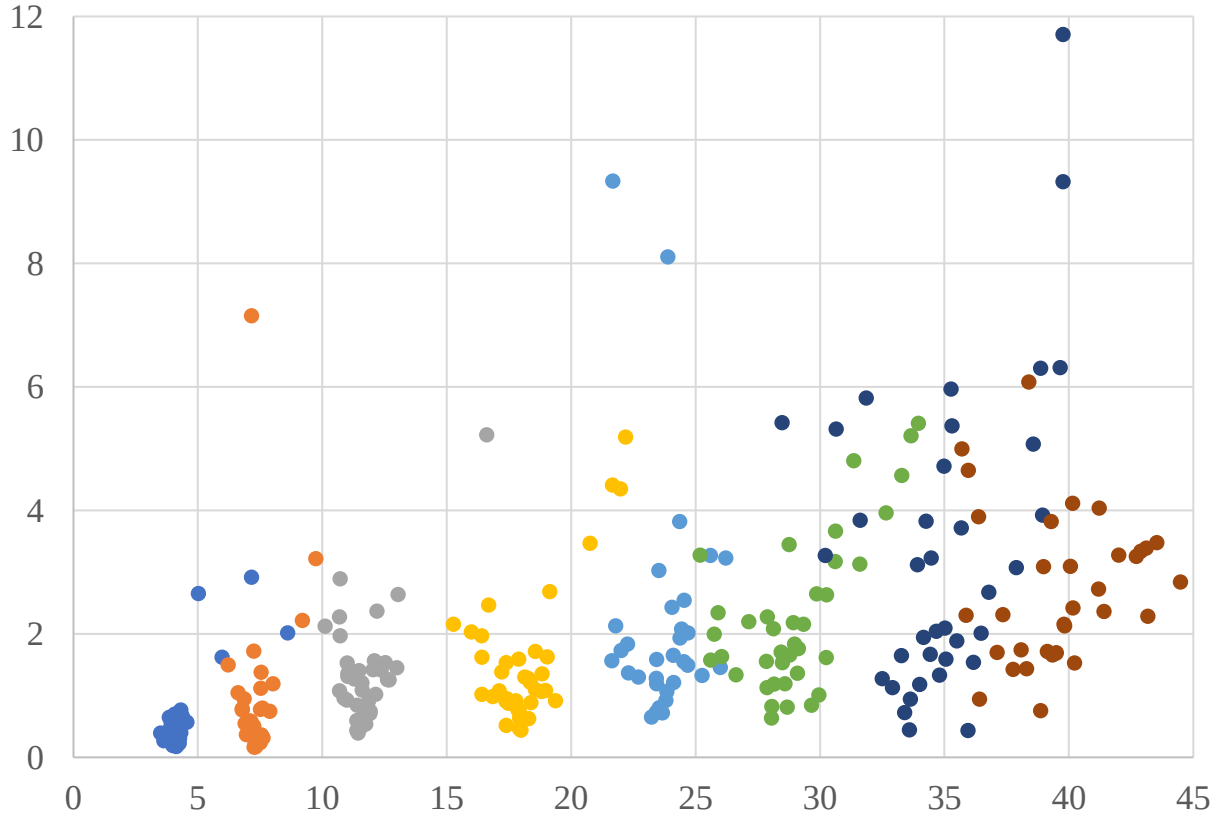

Figure 4.10: Error in pitch angle (degrees) as a function of pitch angle (degrees) for the raw 2DFFT no barred galaxies. Galaxies with higher pitch angles have higher associated errors.

4.4.2 Radial Size and Effective Measurement Annulus

Measurement success rate depends fairly strongly on the radial size of the galaxy in pixels, namely, there is a sharp dropoff in measurement success starting at 30 pixels in radius, with galaxies of all pitch angles and Fourier modes failing to be measured more often than not below 20 pixels in radius. Even GALFIT subtracting Sersic components to flatten the profile doesn't guarantee a good measurement. For galaxies which successfully produce a pitch angle measurement, the associated error is generally less than 5º for galaxies greater than 50 pixels in radius, increasing by a few degrees as the radius approaches zero. It would appear then, if 2DFFT or Spirality produce a measurement for the galaxy, that measurement usually has a relatively small associated error, and as our offset errors from the templates show, the measurement of the pitch angle is accurate. The distribution of sizes of the measurement offset from the templates is comparable to the recorded measurement error standard deviation for the galaxies to within a couple degrees, suggesting the error assignments for 2DFFT and Spirality are fairly correct.

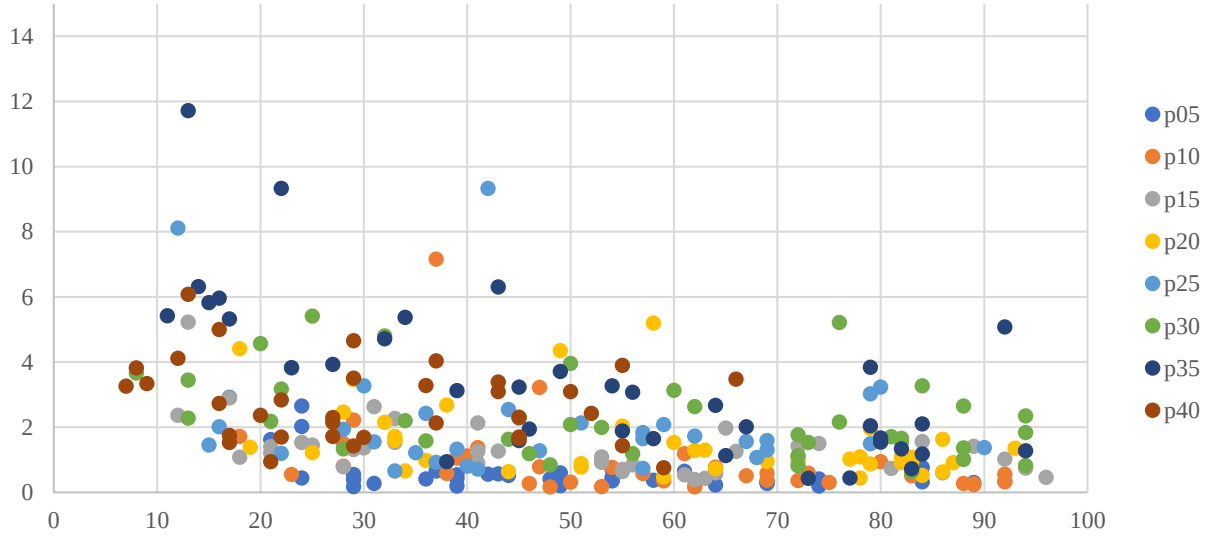

Figure 4.11: Error in pitch angle (degrees) as a function of galaxy radius (pixels) binned by pitch angle for successful measurements of pitch. Most galaxies smaller than 20 pixels in radius fail to produce a pitch angle measurement. Those that do have higher associated errors.

We produce surface plots of the recorded measurement error as a function of pitch angle and galaxy radius as well as a plot of measurement success rate as a function of pitch angle and Fourier mode strength. Galaxies with higher pitch angles and lower radii are shown to have higher associated measurement error, with r~40 being a fairly key level below which the magnitude of the errors increase, especially in high pitch galaxies. Most galaxies below 20 pixels in radius fail to be measured in the first place. The measurement success rate falls off somewhat at high pitch angles, but strongly depends on the Fourier mode strength of the galaxy, with even low pitch angle galaxies failing ~50% of the time when the Fourier mode strength is f=0.1. Since Fourier mode strength is a proxy for arm-interarm contrast, these results suggest a falling off in measurement success below arm-interarm contrasts of ~2 and definitely below ~1.5. The peak to trough height may not be the only factor in play. The broadness vs peakiness of the arms in GALFIT galaxies depend on the Fourier mode strength, with low Fourier mode strength galaxies having very broad, not very peaky arms. In real galaxies, sometimes the arm-interarm contrast is low but the arms themselves are fairly spatially constrained features. These galaxies are likely to have better success rates than the broad GALFIT counterparts of the same arm-interarm contrast.

False positive measurements of pitch angle in this study are very rare, where a pitch angle is measured but disagrees by more than a few degrees with the template pitch angle value. When such a failure occurs, there are a few different scenarios. One is a chirality flip, where the measured pitch angle is the wrong chirality. Another is a pitch angle measurement very close to zero which is usually clearly visibly wrong in looking at the image. Finally, sometimes galaxies with medium pitch angles read as 50-60 degrees in the measurement methods. If the resolution of the galaxy is poor enough not to be able to visually check the results for the pitch angle, some galaxies may be assigned much higher pitch angles than their actual value.

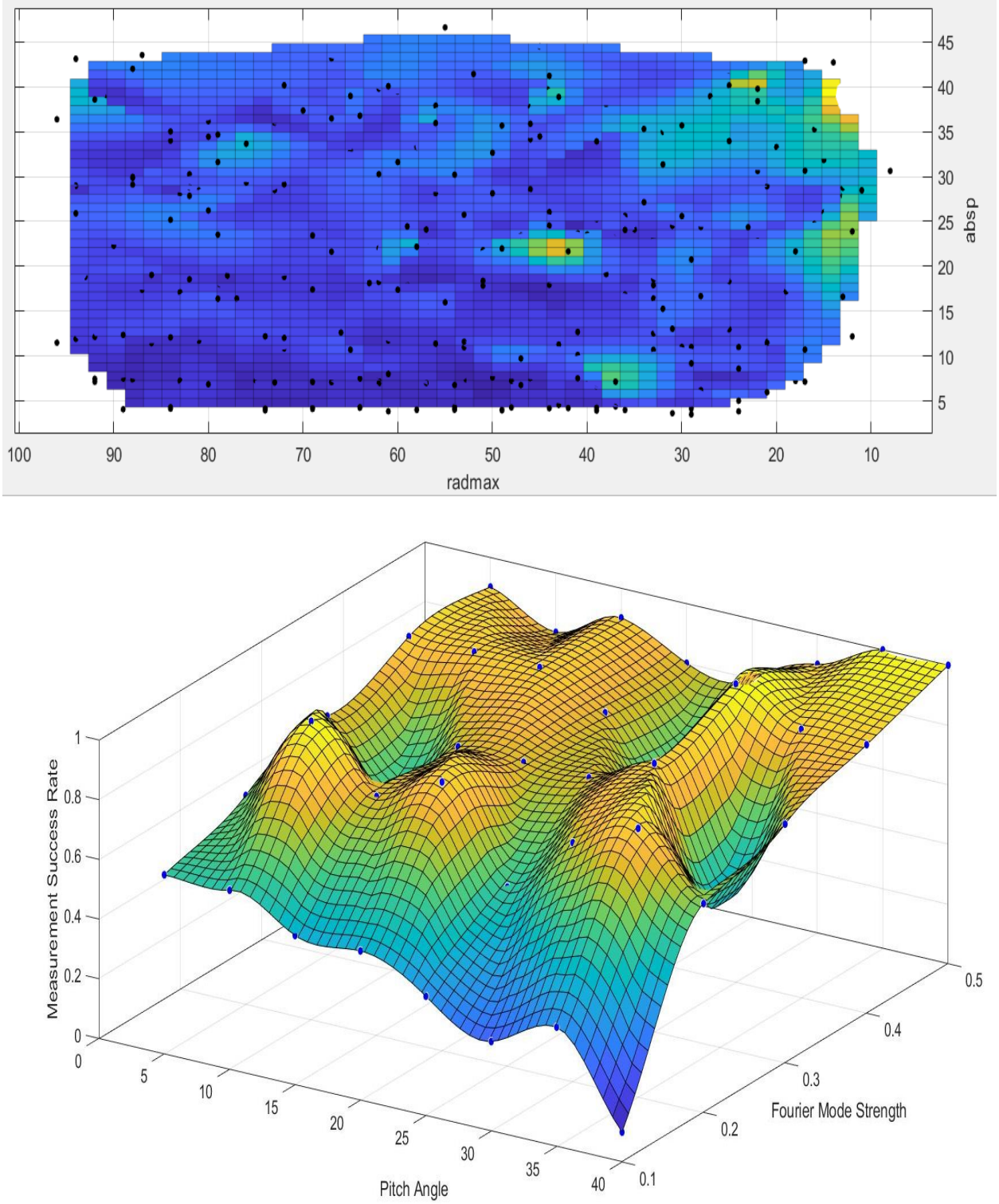

Figure 4.12: Top: Size of error in pitch angle measurement as a function of Pitch Angle and galaxy radius. Higher pitch angles and smaller galactic radii show higher error estimates. Bottom: Measurement success rate plotted against Fourier mode strength and pitch angle. Very low arm-interarm contrasts are much less likely to be successfully measured. This is especially true at high pitch angles.

4.5 Conclusions

The pitch angle measurement codes 2DFFT and Spirality are found to accurately reproduce the pitch angles of template galaxies and agree with one another very well on the value of the pitch angle. The measurement success rate and pitch angle measurement errors depend primarily on the arm-interarm contrast parameter of the galaxy being measured, with some limits set on other parameters. The effective measurement annulus size (outer radius of the galaxy minus bar radius) need be at least 20 pixels. The initial inclination angle of the galaxy need be less than ~70º. It is generally more difficult both in measurement success rate and error magnitude to measure galaxies with higher pitch angles. However, if a stable region of pitch angles is found for a given galaxy it is highly likely to return the correct pitch angle for that galaxy to within a few degrees.

Understanding the limitations of pitch angle measurement is important in constructing unbiased studies of pitch angle distribution functions in galaxy populations in the pursuit of better understanding spiral galaxy evolution and SMBH evolution in spiral galaxies. This study attempts to outline the 'best case' bounds for idealized simulated galaxies without the asymmetric spurs, clumps, flocculence, and other complexities of real galaxies. Even so, we convincingly show stable regions of pitch angle measurement to reproduce accurate pitch angles, so real galaxies with measurable pitch angles should be accurate under most circumstances, possibly with higher recorded error values as stable regions of pitch angle measurement are much smaller.

Extending the study of spiral structure to higher redshifts is important toward the subject of galaxy evolution. With the limitations of pitch angle measurement software better understood, it remains to study biases on the selection side when building sample populations of galaxies for

study. Some galaxies with spiral structure may not be properly identified as spirals at low spatial resolution or low arm-interarm contrast. Further study in this area is desired going forward.

4.6 Bibliography

Berrier, J., Davis, B., Kennefick, D., Kennefick, J., Seigar, M., Barrows, R., Hartley, M., Shields, D., Bentz, M., & Lacy, C. 2013, ApJ, 769, 132

Davis, B. L., Graham, A. W., & Cameron, E. 2018, ApJ, 869, 113, doi: 10.3847/1538-4357/aae820 —. 2019, ApJ, 873, 85, doi: 10.3847/1538-4357/aaf3b8

Davis, B. L., Graham, A. W., & Seigar, M. S. 2017, MNRAS, 471, 2187

Davis, B. L., Kennefick, D., Kennefick, J., et al. 2015, ApJL, 802, L13, doi: 10.1088/2041-8205/802/1/L13

Graham, A. W. 2016, Galactic Bulges, 418, 263, doi: 10.1007/978-3-319-19378-6 11

Haehnelt, M. G., Natarajan, P., & Rees, M. J. 1998, MNRAS, 300, 817, doi: 10.1046/j.1365-8711.1998.01951.x

Kormendy, J. 1981, in Cambridge Univ. Press, Vol. 153, , 111

Law, D. R., Shapley, A. E., Steidel, C. C., et al. 2012, Nature, 487, 338

Lin, C. C., & Shu, F. H. 1964, ApJ, 140, 646

Loeb, A., & Rasio, F. A. 1994, ApJ, 432, 52, doi: 10.1086/174548

Seigar, M. S., Kennefick, D., Kennefick, J., & Lacy, C. H. S. 2008, ApJ, 678, L93

Silk, J., & Rees, M. J. 1998, A&A, 331, L1. https://arxiv.org/abs/astro-ph/9801013

Peng C. Y., Ho L. C., Impey C. D., Rix H.-W., 2002, AJ, 124, 266

Peng, C. Y., Ho, L. C., Impey, C. D., & Rix, H. W. 2007, in Bulletin of the American Astronomical Society, Vol. 39, American Astronomical Society Meeting Abstracts, 804

Shields, D., Boe, B., Pfountz, C., Davis, B., Hartley, M., Imani, H.P., Slade, Z., Kennefick, D., & Kennefick, J. 2015, (arXiv:1511.06365)

Tully, R. B., & Fisher, J. R. 1977, A&A, 500, 105

5 Conclusion

This dissertation has explored the limitations of techniques for surface brightness and galactic spiral arm pitch angle measurement techniques near the limits of detection. The ability to observe and catalogue the low surface brightness outer structures of galaxies as well as faint companions has important implications in the study of cosmology and galaxy evolution. In a similar manner, extending the relation between SMBH mass and pitch angle to higher cosmological redshifts will allow SMBH mass measurement for late type galaxies earlier in the universe than under current techniques. Building a local Black Hole Mass Function for spiral galaxies provides a portion of the picture, a local snapshot of one subpopulation of black holes in the universe. Ensuring the capabilities and shortcomings of techniques for measuring pitch angles is vital toward building reliable datasets from galaxies at lower surface brightness and smaller pixel sizes. When biases and errors are well understood, the spiral galaxy subset of black holes may be studied as a function of time in addition to the current local picture.

In Chapter 2 of this dissertation, we move toward completing the local late type galaxy black hole mass function through inclusion of lower surface brightness galaxies in population sampling for black hole mass measurement. Missing galaxies (beyond the observing limit of the CGS survey) are reasonably corrected for and a revised BHMF for local late type galaxies is generated. A possible division between Hubble types a-c and the cd, d types is shown, with population clustering in pitch angle space corresponding very well to Hubble Type classification, and the latest Hubble types having the largest measured pitch angles. It should also be noted the pitch angles of m type spirals (Magellanic dwarfs) were not able to be measured. It would be interesting to acquire SMBH masses for these dwarf spiral galaxies in that they might belong to the intermediate mass black hole population. Deeper surveys of local galaxies could additionally be analyzed in future work to build larger samples of fainter local galaxies.

In Chapter 3 of this dissertation, UGC 4599 is classified as a GLSB analog to Hoag's object. The disk of UGC 4599 is shown to be extremely faint, with a central extrapolated surface brightness near 26^{th} r magnitude. Estimates for star formation rates from the core region, ring region, and disk/spiral region of

the galaxies are derived from the u filter surface brightness of the galaxy. The primary spiral arm of UGC 4599 is measured through several different methods to have a pitch angle near 6 degrees, which would correspond to an SMBH mass toward the heavier end for spiral galaxies, as expected given the more elliptical-like core of the galaxy. Galaxies which, like UGC 4599, were previously classified as relatively local high surface brightness galaxies might have fainter outer components not catalogued to date. Revisiting surveys of local galaxies at fainter observing limits is an informative endeavor toward identifying new candidates of these specific galaxy types. While relatively diffuse, the mass of stars in the faint outer regions of galaxies may be a significant contributor to the total star formation rate of the galaxy, as we illustrate for UGC 4599. Better characterization of the low surface brightness local universe has important implications for cosmology questions and galaxy evolution studies.

In Chapter 4 of this dissertation, we return to spiral arm pitch angle measurement and evaluate the strengths and weaknesses of some of the techniques for measuring this quantity. It appears some of the primary limiting factors in measuring pitch angle are signal to noise ratio above the sky, arm-interarm contrast ratio, inclination angle, pitch angle itself, and galactic radius in pixels, or more specifically effective annulus (annulus outside the bar region of the galaxy) in pixels. Realistically modelled GALFIT galaxies inserted into field images may shed light on selection effects in building populations of spiral galaxies for pitch angle measurement. Continued study of the limitations and biases of pitch angle measurement techniques will ensure robust measurements of these populations. The evolution of spiral galaxies and of the pitch angle distribution function over time are of interest, and extending populational studies to higher redshifts is necessary for fuller understanding.